# A NOVEL FINITE ELEMENT INVERSE ANALYSIS TO ASSESS BONE FRACTURE HEALING

By

Jared Anthony Weis

Dissertation

Submitted to the Faculty of the

Graduate School of Vanderbilt University

in partial fulfillment of the requirements

for the degree of

DOCTOR OF PHILOSOPHY

in

Biomedical Engineering

December, 2011

Nashville, Tennessee

Approved:

Michael I. Miga

Anna Spagnoli

Craig Duvall

John C. Gore

Hak-Joon Sung

TABLE OF CONTENTS

Page

Appendix

# ACKNOWLEDGEMENTS

Special thanks go to my co-advisors and mentors Dr. Michael Miga and Dr. Anna Spagnoli for their invaluable help and support throughout my work. Their guidance, support, and encouragement have been invaluable as I have progressed throughout my graduate school career. Specifically, Dr. Spagnoli has passed on to me the enthusiasm and motivation for both research and the study of bone fracture healing. Dr. Miga graciously allowed me to continue my work at Vanderbilt when Dr. Spagnoli's lab moved to UNC, and has passed on to me his excitement for computational analysis and has continually helped me with his time and most helpful guidance.

I would also like to thank committee members Dr. Craig Duval, Dr. John Gore, and Dr. Hak-Joon Sung for their helpful comments, guidance, and encouragement.

Past and present members of the BML and SNARL labs at Vanderbilt as well as past and present members of the Spagnoli Lab (at both Vanderbilt and UNC) also deserve special thanks. Without the help and support of lab members, post-docs and students alike, I would have never learned the many skills and techniques required to complete my research project. I would like to specifically thank Froi (Dr. Froilan Granero-Molto) for all of the time he spent teaching me the ins-and-outs of fracture healing biology as well as being a gracious host when I spent time at UNC generating and analyzing data.

Additionally, I would also like to acknowledge the Vanderbilt University Institute for Imaging Science (VUIIS) Center for Small Animal Imaging (CSAI) and the University of North Carolina – Chapel Hill (UNC-CH) Biomedical Research Imaging Center (BRIC) for assistance with microCT imaging.

Also, I would like to acknowledge my funding source; the majority of this work was supported by National Institutes of Health (NIH) Grant 5R01DK070929-02 from the National Institute of Diabetes and Digestive and Kidney Diseases (NIDDK).

Last and most certainly not least, I would like to recognize that all of this would have never been possible without the love and support of my wonderful wife Victoria. Tori has always been there for me and has graciously put up with me during my times of great frustration during my grad school career (when things were not quite working correctly). Tori, and our 'puppy' Maya, have been my rock throughout all of this and I am forever grateful to them.

LIST OF TABLES

LIST OF FIGURES

# CHAPTER I

# INTRODUCTION AND BACKGROUND

## Introduction

Bone fracture calluses are inhomogeneous, irregular materials and this complexity has led to considerable uncertainty in the assessment of biomechanical property improvement or impairment during various therapeutic interventions and genetic models of pathological fracture healing. Currently, the gold standard in biomechanical testing methodologies do not account for the confounding geometrical effects associated with the callus shape and constituency. Unfortunately, as a result, arguably one of the most important criteria, mechanical stability, is the least resolved with respect to fracture healing assessment. The current gold standard in functional assessment of fracture healing relies on biomechanical assessment of extrinsic material properties (force, displacement, stiffness); as such, there is a considerable lack of methods to assess fracture callus material properties without geometrical bias, rendering many studies inadequate to fully evaluate the fracture healing pathophysiology. Confounding geometrical factors can strongly bias extrinsic material property assessment of mechanical functional differences between fracture calluses (especially in situations where the callus geometry is drastically different), with some authors confusing the observation of an increase in strength of a healing callus with accelerated healing, rather than an increase in callus tissue volume/cross-sectional area. Traditional mechanical analysis techniques avoid these confounding geometrical effects by normalizing over

cross-sectional area and length, thereby working with intrinsic material properties (stress and strain) instead of the extrinsic material properties (force and displacement) that standard biomechanical analysis of fracture calluses relies on. However, due to the complexity and inhomogeneity of fracture calluses, simple normalization is inadequate and improper. Therefore, I will show that inverse finite element analysis can be extended and enhanced to assess: (1) longitudinal bone fracture callus mechanical property differences in a mouse model of fracture and (2) biomechanical improvement in fracture healing of mice receiving therapeutic intervention. Based on recent evidence that transplanted mesenchymal stem cells (MSC) migrate to the fracture site and participate in the initiation of the repair process while also contributing to enhancement of biomechanical properties [1], I hypothesize that MSC transplantation can ameliorate healing in fractures through enhancement of the biomechanical properties as measured by inverse FEA modulus reconstruction. Towards this end, the specific aims of this research are as follows:

(1) Development, construction, and validation of a novel inverse FEA modulus reconstruction methodology for biomechanical analysis of bone fracture healing.

(2) Utilize the inverse analysis method as compared to more traditional analysis metrics of fracture healing to assess the biomechanical properties of fracture calluses from longitudinal fracture healing in mice either receiving or not receiving therapeutic MSC transplantation.

(3) Extend the inverse analysis method with (a) ease-of-use enhancements through the development of a web-enabled submission system and (b) incorporation of an enhanced level of FE model sophistication.

# Background

## Biology of fracture healing

In long-bones, fracture healing proceeds through the formation of a cartilaginous template that is then replaced by bone that undergoes remodeling [2]. Fracture healing is a postnatal repair process that recapitulates aspects of the embryonic development of the skeleton. This process is briefly outlined in Figure 1. It proceeds via callus formation and an endochondral ossification sequence, where cartilage forms, matures, undergoes hypertrophy, and is eventually replaced by the new bone that bridges the fracture gap. In step 1 (Figure 1, A), immediately after the fracture, bleeding occurs which is followed by the development of a blood clot (fracture hematoma). In step 2 (Figure 1, B), an internal callus is formed by a network of spongy bone that unites the inner surfaces, and an external cartilaginous callus is formed which stabilizes the outer edges of the bone. In step 3 (Figure 1, C), the external cartilaginous callus is replaced by new bone, and spongy bone unites the broken bone ends. Dead and injured bone fragments are removed and replaced. In step 4 (Figure 1, D), local swelling marks the location of the initial fracture, which over time is remodeled. Throughout the fracture healing process, the newly formed cartilaginous callus stabilizes the fracture and provides a template for new bone formation. A critically important function of bone healing is that the healing tissue provides sufficient mechanical stabilization such that a return to functionality is possible.

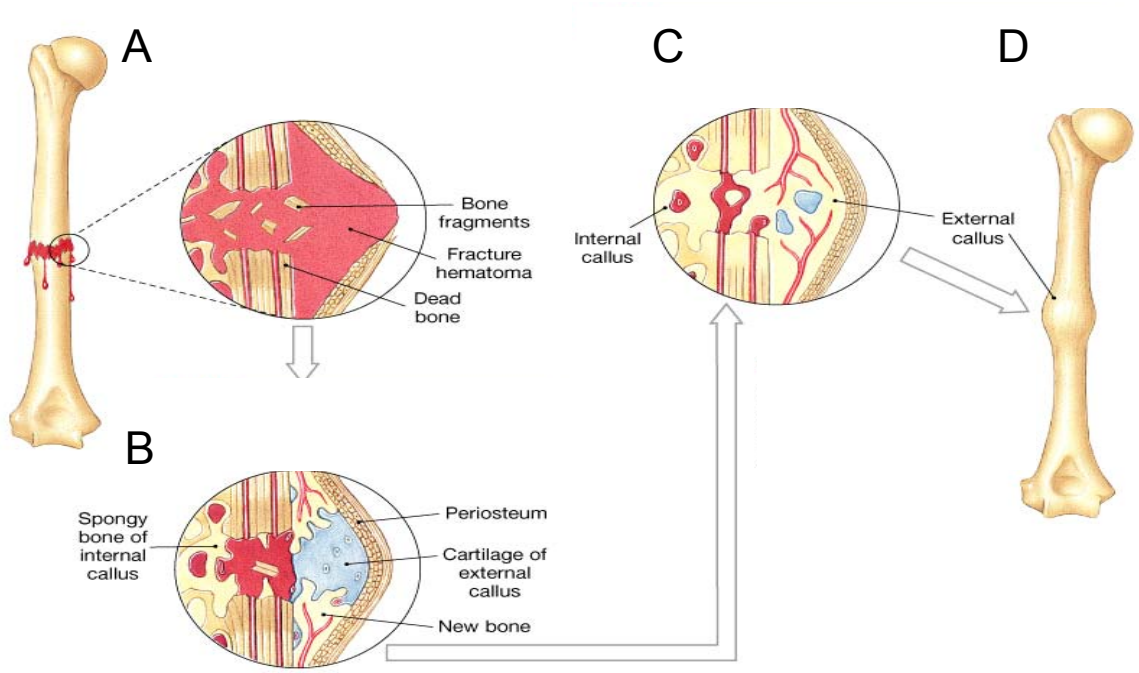


Figure 1. Bone fracture healing process. A: After the fracture bleeding and swelling occurs. B: Cartilage tissue (callus) bridges the fractured bone ends. C: Cartilage template is replaced by bone. D: Over the time the bone is remodeled. Adapted from [3].

Bone fracture nonunion

Approximately 10-20% of the 6.2 million annual bone fractures result in fracture healing failure (non-union), causing significant morbidity and mortality [4, 5]. Additionally, patients with osteogenesis imperfecta (osteodysplasia from a defect in collagen I assembly) suffer from recurrent fractures, many of which result in non-union. Fracture non-union is marked by the absence of bridging bone in radiographic images. An example of normal and non-union murine fracture healing is shown in Figure 2A and Figure 2B, respectively. The precise reasons why some fractures result in non-union are unclear, however it has been hypothesized that a limitation in the number and/or migratory capacity of native osteo-chondroprogenitors and/or growth factors, as well as

ineffective stabilization play pivotal roles in the failure of bones to undergo healing. As there is no validated/universally accepted definition of fracture non-union, clinical diagnosis of non-union is defined subjectively by physicians through time to radiographic bridging by serial radiography [6]. There is a considerable lack of consensus in what defines fracture non-union, with clinical definitions of non-union ranging from 2-12 months post-fracture with no radiographic bridging [6]. Currently there are no reliable methods that are capable of determining when a patient's fracture will fail to undergo healing without requiring clinical intervention, requiring many patients to undergo prolonged periods of morbidity and pain (up to 12 months) prior to more advanced clinical intervention.

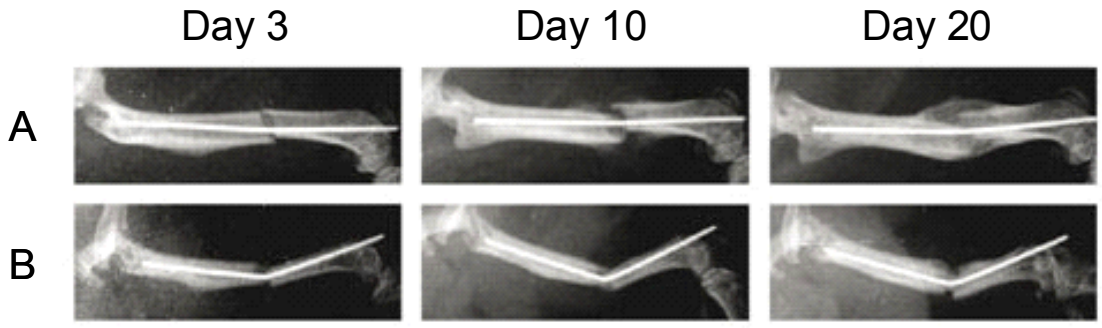


Figure 2. Murine fracture healing observed by serial x-ray images over a time course of 20 days resulting in (A) union and (B) non-union. Adapted from [7].

Following a diagnosis of fracture non-union, the current treatment options typically involve grafting (either autograft or allograft) along with significant invasive internal and/or external fixation followed by prolonged periods of immobilization, and do not guarantee future fracture healing success. In fact, recurrent fracture non-union

presents a major clinical problem. In these types of non-unions, a lack of fracture stabilization is clearly not the clinical problem; there is an underlying biological limitation.

Rationale for MSC in fracture healing

As the fracture repair process relies heavily on the osteo-chondroprogenitors that are recruited to the fracture site, new experimental therapeutic treatments for fracture healing pathologies have begun to explore the use of bone marrow (BM) mesenchymal stem cells (MSC) to enhance the available population of such progenitors. The evidence that BM contains MSC that can differentiate into chondrocytes and osteoblasts emerged from the studies of Friedenstein, who found that BM contained plastic-adherent cells that differentiated *in vitro* and *in vivo* into cartilage and bone [8, 9]. These initial observations clearly indicated the therapeutic potential for MSC, resulting in a phenomenal expansion of MSC studies over the last decade. The number of MSC in BM is low, but they are easy to isolate and expand; millions of cells can be generated from less than one milliliter of BM [10-20]. Moreover, the therapeutic use of MSC offers advantages over embryonic stem cells, in fact MSC: can be autologous, are easy to harvest, are more abundant, have no evidence of tumorgenicity and, raise no ethical controversies. MSC infused systemically or implanted locally have been shown to migrate and home into damaged tissues including fractured bones [21-25]. Initial clinical studies, including a study in children with severe osteogenesis imperfecta (O.I) have indicated that MSC or whole BM infusions can repair damaged tissues, including bone [23, 24]. Recently in an experimental animal study included within Appendix A and

summarized here, systemically transplanted MSC have been shown to beneficially affect bone fracture healing in normal murine tibia that otherwise would have undergone normal fracture healing [1], demonstrating a role for therapeutic MSC transplantation to advance healing in non-pathological (and potentially pathological) fractures. This study appears in: Granero-Molto F, Weis JA, Miga MI, Landis B, Myers TJ, O'Rear L, Longobardi L, Jansen ED, Mortlock DP, Spagnoli A. Regenerative effects of transplanted mesenchymal stem cells in fracture healing. Stem Cells 2009;27: 1887-98.

This study demonstrated evidence that transplanted MSC migrate to the fracture site and participate in the initiation and enhancement of the repair process *in vivo* in a dose-dependent manner. To assess this dose-dependent homing at the fracture site, MSC transduced with an adenoviral vector expressing *luciferase* (MSC-Adn-Luc) were systemically transplanted into mice with an experimental tibia fracture via tail vein injection. As expression is lost in dividing cells (no host genome integration), the observed luciferase signal only assesses direct MSC migration at the fracture site. As shown in Figure 3, MSC homing was observed to be dose-dependent in mice with fractured tibia transplanted with increasing doses of MSC-Adn-Luc (from $5X10^3$ to $1000X10^3$ MSC) at 3 days post-fracture as observed by bioluminescent imaging (BLI) (n = 3 mice per dose). The ED50 was determined as $300X10^3$ cells and a plateau was observed beginning at $700X10^3$ cells without any significant increase after a dose of $1000X10^3$ cells. This shows that MSC migration reaches a saturation point in which increasing dosage yields no further improvement in migration.

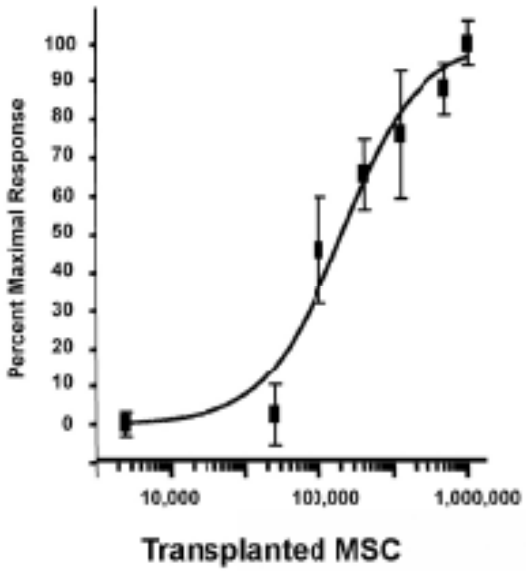


Figure 3. Dose-dependent homing of transplanted MSC in response to tibia fracture. Adapted from [1].

This study also evaluated the timing and amount/length of engraftment of MSC homing to the fracture site. To assess the dynamics of *in vivo* MSC migration in response to tibia fracture, $1X10^6$ MSC-β-Act-Luc, constitutively expressing *luciferase*, were transplanted into mice with stabilized tibia fracture and sequential BLI imaging was performed from day 1 to day 14 post-fracture/transplant. As depicted in Figure 4 (left panel), one day after the fracture/transplant MSC-β-Act-Luc were visualized at the lung site. On day 3 post-fracture, MSC began to preferentially localize at the fractured leg site (right tibia) as compared to other locations, where they persisted for up to 14 days post-fracture/transplant (Figure 4, left panel). Semi-quantitative analysis of the BLI signal of luciferase-tagged MSC over the fractured leg showed a time-dependent response, with BLI signal increasing progressively from day 1 to day 7 without any further increase at day 14.

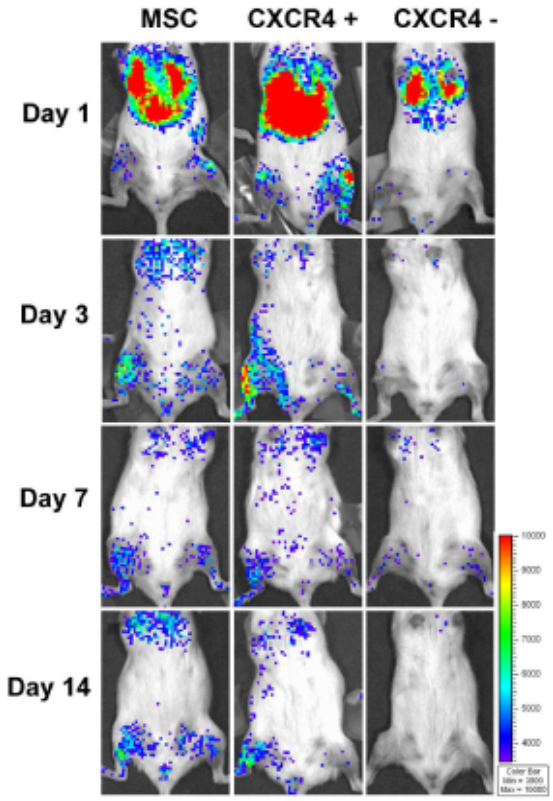


Figure 4. MSC migrate to the fracture site in a time- and CXCR4-dependent manner. Adapted from [1].

To investigate whether MSC improved the callus material properties, tensile BMT was performed. Dissected calluses from MSC recipient mice (MSC) as well as control calluses from mice that did not receive MSC (no cells) were subjected to tensile loading at 0.25 mm/min until failure. As shown in Table 1, calluses of mice that received MSC had increased toughness, ultimate displacement, and peak force compared to controls. The callus stiffness was not different in the two groups. Taken together, these data indicate that MSC improve the callus material properties.

Table 1. MSC improve the biomechanical properties of the fracture callus. 14 days after fracture, callus from mice that were transplanted either with or without MSC were dissected and subjected to tensile BMT. [a], $p<0.05$ vs No Cells; [b], $p<0.01$ vs No Cells by Student's t-test. Adapted from [1].

| | No Cells (n=5) | MSC (n=6) |
|---|---|---|
| Toughness (N-mm) | 0.138 ± 0.044 | 0.425 ± 0.143 [b] |
| Ultimate Force (N) | 1.803 ± 0.488 | 2.492 ± 0.829 |
| Stiffness (N/mm) | 17.790 ± 8.861 | 12.000 ± 7.591 |
| Ultimate Displacement (mm) | 0.124 ± 0.045 | 0.308 ± 0.148 [a] |

Volumetric changes as determined by microCT imaging were also determined for mice receiving and not receiving MSC transplantation. Mice that received MSC transplant displayed a significant increase of the total volume, as well as total bone, soft tissue, new bone, and callus volumes and callus mineralization content compared to controls (Figure 5A). The three dimensional reconstructions of the entire calluses as well as the sagittal sections showed remarkable differences in the size and morphology of the new mineralized callus in mice that received MSC versus controls. As shown in Figure 5B, the most notable differences were that: 1) a large callus surrounded the fractured bone edges as well as the intact cortical bone in the calluses from mice transplanted with MSC, but remained limited to the ends of the bone segments in the controls [compare Figure 5 panels B1 with B5 and B3 with B7]; 2) a continuous net of the creeping callus

bridging the fracture gap in MSC recipient mice versus the limited connectivity observed in the controls [compare Figure 5 panels B2 with B6 and B4 with B8]. These findings indicate that MSC transplant, by providing a more organized bridge between the bone ends, improves the reparative process.

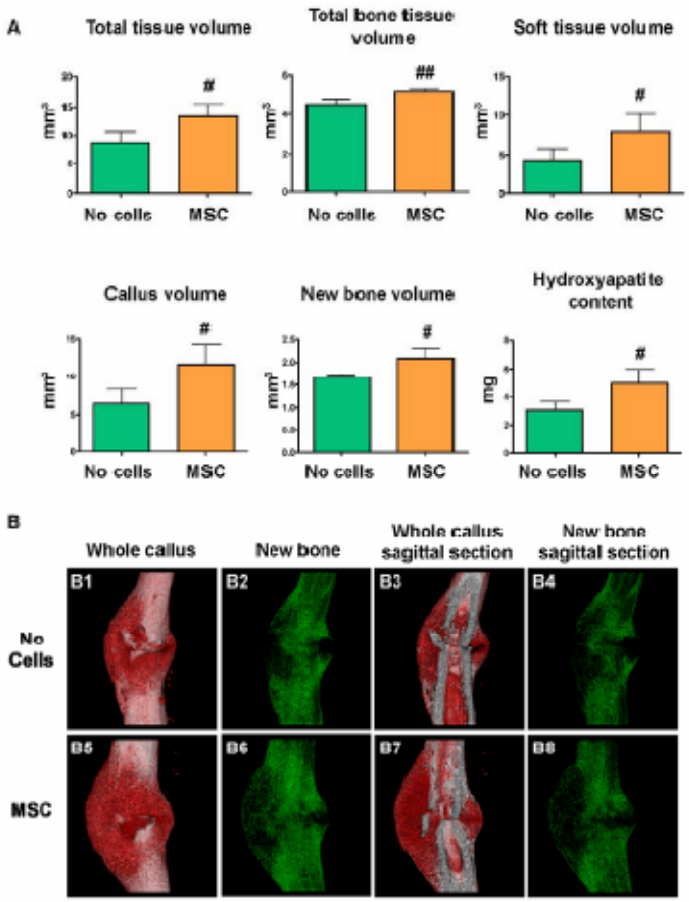


Figure 5. MSC transplant increases callus size and changes callus morphology. (A): µCT analyses were performed 14 days after fracture in calluses dissected from mice that received MSC transplant and no cells. Callus volume and new bone volume were calculated after subtracting the cortical bone volume respectively from the total volume and the total bone tissue volume. #, $p<0.05$ versus No Cells; ##, $p<0.01$ versus No Cells by Student's t-test. (B): three-dimensional reconstruction of whole calluses (B1, B2, B5, B6) and sagittal sections (B3, B4, B7, B8) were obtained 14 days after tibial fracture in calluses from mice that were transplanted with MSC or no cells. Adapted from [1].

Experimental assessment of fracture healing

Fracture healing is a complex biological process, and therefore numerous experimental studies (largely dependent on rodent models) have been performed to

elucidate the mechanisms responsible and develop therapeutic treatments for bone fracture healing. Likewise, there is also a considerable need to develop assays capable of detecting advancements or regressions in healing due to therapeutic treatment or experimental impairment (usually through genetic modifications). As such, many analysis techniques to assess the progression of the healing process have been proposed, such as histomorphometry, imaging, and biomechanical testing [26].

Histological methods of bone fracture healing analysis involve an extensive and time-consuming process of decalcifying, dehydrating, paraffin embedment, and sectioning. The bone fracture callus sections are then stained with histological markers that highlight tissues of interest, or regions where tissue-specific proteins are expressed. Usually, due to difficulty of quantitative assessment in bone fracture calluses, these histological preparations are qualitatively compared, but some have applied quasi-quantitative histomorphometric measurements that have been established for intact bone measurement to the assessment of fracture callus. Typically for these histomorphometric measurements, transverse sections are taken at fixed linear distances along the length of the fracture callus in relation to the callus midline and stained with either Safranin-O/Fast green or Masson's Trichrome. Volumetric measurements of diameter (callus) and area (cartilage, fibrous tissue, void, and osseous tissue) are then performed on the histological images. While histological methods are capable of accurately highlighting and describing tissue composition, comparisons between different samples are difficult due to the uncertainty of the section's original position in the callus. Furthermore, due to the lengthy sample preparation time and the difficulty of side-by-side comparisons from different samples, true quantitative assessment is unrealistic. Histological analysis

methods are also limited to post-mortem analysis and have an inability to provide direct functional information about the mechanical stability of the callus.

Researchers have also relied on various imaging modalities to assess the progression of fracture healing, such as x-ray, micro-computed tomography (microCT), magnetic resonance imaging (MRI), and positron emission tomography (PET) [27-34]. However, radiographic imaging (x-ray and microCT) remains the most heavily used due to advantages in visualization of bone. The major advantages in imaging based assessments of bone fracture healing are due the fast acquisition time and non-destructive nature, in comparison to histological assessment. In x-ray based fracture healing assessment, similar to the standard clinical method of fracture healing assessment, 2-D radiographic images in multiple planes (anterior-posterior and lateral) are acquired and qualitatively assigned a healing score based on the bridging callus bone. However, due to the subjective nature of the x-ray scoring system, microCT imaging remains the most heavily used in experimental fracture healing imaging assessment.

MicroCT has advantages over other imaging modalities in three dimensional qualitative representation and quantification of bone volume and density. MicroCT analysis of fracture callus relies on three dimensional reconstruction of the serial microCT axial images. The three-dimensional callus image is then subjected to densitometric and volumetric analysis, and when properly calibrated, it is possible to quantify both the density and amount of various tissues in the callus (non-mineralized callus, mineralized callus, and original cortical bone). For volumetric analysis, tissue volume can be quantified based on selecting density threshold ranges that correspond to physiologically distinct tissue types. If the tissue density falls between a certain threshold

range (based on threshold standards from scanned bone phantoms and/or serial microCT and histological comparisons), the tissue can be classified as non-mineralized callus, mineralized callus, or cortical bone. While capable of qualitative visual assessment and quantitative volumetric analysis, microCT imaging alone provides no functional information about the mechanical integrity and load-bearing properties of the healing bone, limiting its value in assessing bone fracture healing.

Recent studies have suggested the use of microCT as not only a quantitative volumetric analysis method, but as a surrogate measure of mechanical function through correlation/multi-regression of microCT analysis parameters (tissue mineral density – TMD, standard deviation of TMD – σTMD, bone volume – BV, total volume – TV, BV/TV ratio, and bone mineral content – BMC) [35, 36]. A recent study utilizing these methods was able to explain 62% of the variability in maximum torque (using TMD, BV, and σTMD) and 70% of the variability in torsional rigidity (using TMD, BMC, BV/TV, and σTMD) with only microCT parameters used in stepwise multiple regression analyses [35]. However, this explanation is purely correlative in nature and does not directly address functionality of the healing callus tissue. These microCT metrics, including those used in microCT-to-BMT regression studies, by design only provide quantification of volume and/or mineral density and therefore do not reflect the 3-dimensional mechanical connectivity of bone tissue within the callus. Similar to dual-energy X-ray absorptiometry (DXA) measured bone density (a bone quantity measure which has been disputed as an accurate measure of bone quality [37-43]), these commonly used microCT measures quantify bone quantity/density within the callus but ignore changes in the geometry and spatial organization of the callus tissue and thus do not accurately reflect

callus mechanical quality, which is the major determinant of mechanical function. As bone fracture healing progresses, there is both a gradual accumulation of bone mineral as well as a gradual spatial arrangement of that mineral towards enhanced mechanical function/stability. While the total volume and amount/density of mineral somewhat correlate with early stage healing progression, these are not the proper biomarkers to monitor as a determinant of fracture healing as they do not directly correspond to callus quality or mechanical function. While an imaging marker surrogate for mechanical function is highly desirable, our hypothesis is that only through the direct analysis of force and displacement data can mechanical integrity be assessed.

As the primary goal of fracture healing treatment is a return to load bearing function, mechanical integrity of the healing fracture remains an important metric. Due to limitations in other assessment modalities, biomechanical testing remains the gold standard for functional fracture healing assessment. However, biomechanical testing of fracture callus does not come without its own caveats. Classical biomechanical analysis techniques use extrinsic force versus displacement data obtained from mechanical testing of homogeneous machined samples and analytic calculations based on specimen geometry to generate intrinsic material property information, such as tissue elastic modulus. However, due to the atypical and inhomogeneous nature of the fracture callus, seen in Figure 2, such machining and homogenization is improper. Therefore, mechanical testing and theoretical calculations must be performed on the irregular and inhomogeneous specimen, for which a true closed-form solution does not exist. This process yields extrinsic material property metrics, such as apparent stiffness. For intrinsic material property information, analytic calculations rely on the assumption of a

homogeneous and regular cross section. But because of the irregular geometry of the bone and callus, these calculations have been shown to be strongly biased by geometrical factors [44] and are unable to generate intrinsic material properties. Thus, the current gold standard approach of determining extrinsic material properties as a biomechanical metric for fracture healing is clearly lacking.

In response to the current state of mechanical analysis of fracture calluses, researchers have recently begun to explore coupling microCT imaging with finite element analysis (FEA) to provide mechanical behavior information based on accurate geometrical information to study fracture healing. These subject-specific CT-based FEA studies rely on direct CT-attenuation to stiffness-value transformations to provide the important material mechanical properties [45, 46]. For example, Shelfbine et al. [46] reported an empirical power law relationship between modulus and density (Figure 6). The relationship under-predicted in cases with lower mineralization, i.e. when calluses are in their early healing stages. At later times, with more mineralization, the correlation improved. Shelfbine et al. [46] also did show a moderate correlation between predicted and experimental torsional rigidity for rat femur fractures at 3 and 4 weeks ($R=0.69$, Figure 7). However, it seems clear that the direct relationship between CT attenuation/density and mechanical parameters is unclear and insufficient; and when factoring in the potential for variability of this relationship across experimental systems, it is unlikely that the correlation will improve. One aspect regarding CT interrogation of callus healing that is clear, is its ability to discriminate calcification differences throughout the callus region. Combining these techniques with soft-tissue interrogation methods in the future may also provide more information regarding tissue structure and

consistency. However, with respect to function, the need to characterize load-bearing properties is of considerable importance if trying to assess treatment efficacy within small animal systems.

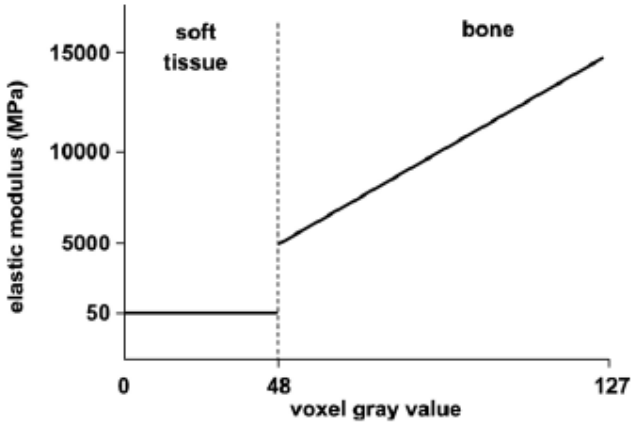


Figure 6. Relationship between voxel gray value and elastic modulus. Adapted from [46].

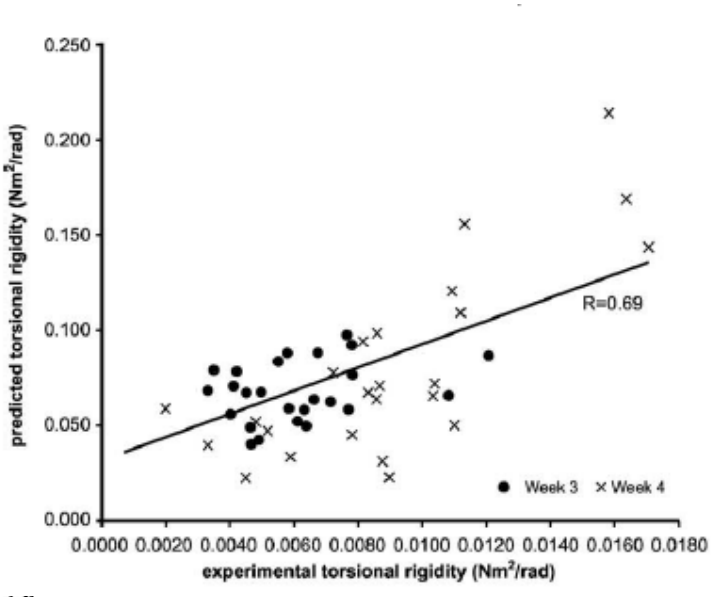


Figure 7. Predicted and experimental torsional rigidity of rat femur. Adapted from [46].

An extension to the extrinsic predictive 'forward' modeling (coupling microCT imaging and FEA through empirical relationships) as employed by Shefelbine et al. [46] to determine tissue-level material properties, is through the additional coupling of these methods with mechanical testing. With the additional coupling of mechanical testing information to the subject-specific FE models generated by microCT, an 'inverse' strategy can be employed such that tissue-level intrinsic material properties can be iteratively reconstructed.

## Significance

The concept of an inverse FE analysis method has been successfully used by many to determine the mechanical parameters of different soft tissues. The method is most commonly referred to within the imaging domain as elastography [47-53]. Many of these studies focus on using mechanical properties to characterize/monitor the progression of diseases that increase the stiffness of tissues (e.g. liver fibrosis [47], breast cancer [51, 54, 55]). Similarly here, the approach is to evaluate mechanical properties as a biomarker in the assessment of fracture healing progression. Quantifying the change in tissue-level mechanical properties during the fracture healing process may provide information that: (1) allows one to diagnostically determine when healing has stopped, (2) suggests the need for intervention in nonunion/slow healing fractures, and (3) evaluates the effectiveness of treatments (such as MSC therapy) that aim to enhance the healing process through the formation of more mechanically competent tissue. Without elastographic methods, such tissue-level mechanical property information is unattainable.

I therefore present a technique that allows for the reconstruction of subject-specific modulus properties from the acquired empirical data (i.e. force-displacement, and microCT image data). Rather than use a CT-to-stiffness empirical relationship and then use indirect measures such as torsional rigidity, or use imaging as a surrogate for functional mechanical analysis, this application takes a more elastographic or mechanical imaging view [48-53, 56-60] of the problem to directly generate values for mechanical parameters. Briefly stated, my approach combines a finite element (FE) model of the subject's callus/bone geometry, data acquired from mechanical testing, and numerical optimization techniques to characterize the mechanical properties of the callus region. This approach does not require calibration per system but rather is an active reconstruction parameter that can be measured experimentally. As detailed above, this approach represents a novel application of inverse analysis methodology to the problem of determining fracture callus tissue-level mechanical properties from microCT images and biomechanical testing.

# CHAPTER II

# METHODOLOGY

## Inverse FEA Modulus Reconstruction Overview

As summarized in Figure 8, the inverse FE modulus reconstruction procedure begins with the establishment of an assumed Hookean linear elastic tissue model framework for the bone/callus system. In brief, the process continues with the development of a bone/callus computer model of the subject generated from microCT image volumes. A volumetric tetrahedral grid is then generated to represent a FE mesh system. Boundary conditions for the model are chosen to reflect the BMT protocol, in which the top boundary is prescribed a fixed upward normal displacement and the bottom surface is fixed in both the normal and lateral direction. The remaining boundary conditions for the sides of the model are stress free. Solutions to the elastic system are then generated as reported previously [47]. As shown by Barnes and colleagues, the unused Galerkin equations associated with the implementation of the Dirichlet boundary conditions are utilized post model-execution to estimate the local boundary stress [47]. This stress is then averaged over the tensile boundary surface and multiplied by the surface area to generate a model-calculated average force ($F_{calc}$) applied to the bone surface for the given displacement. This force is then compared to the BMT acquired force in a least-squares sense and properties of the callus determined through an inverse iterative optimization process.

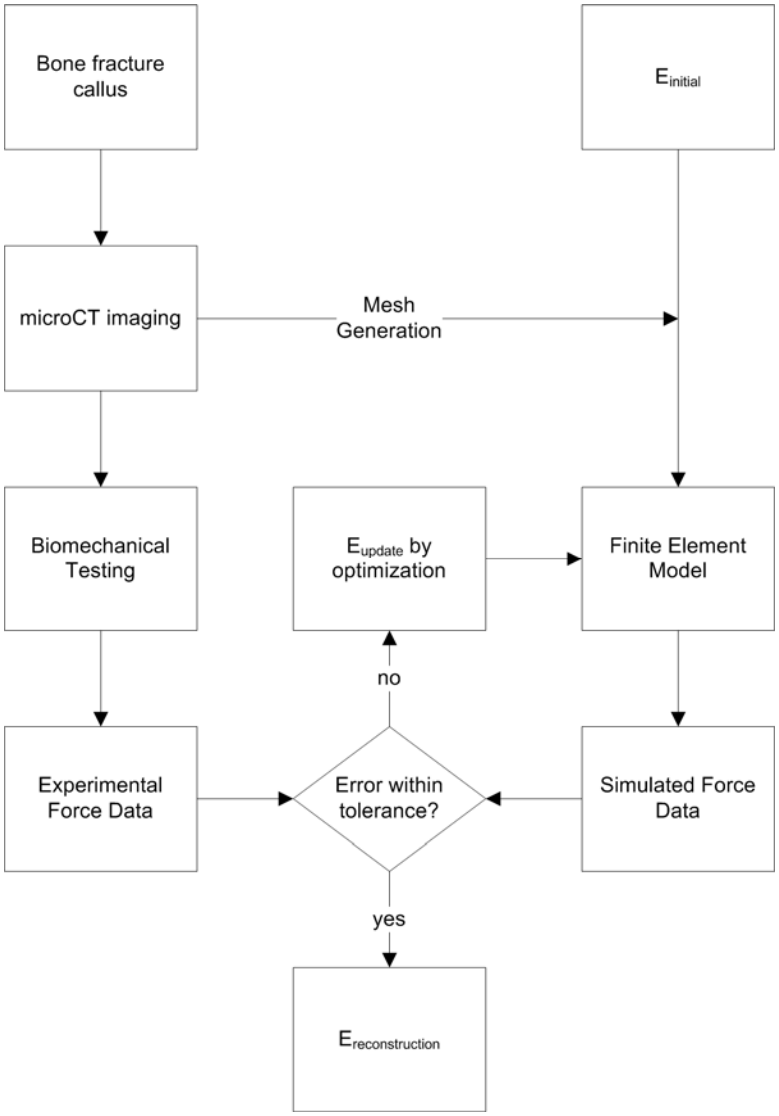


Figure 8. General framework of the inverse material property reconstruction method. The stiffness is iteratively reconstructed by comparing model calculated forces to BMT forces. Adapted from [61].

# Computational Methodology

## Computational System Methodology

The first and most important step in the generation of bone fracture callus tissue material property estimates through inverse FE analysis is building a finite element model from the microCT image volume that represents the discretization of the bone fracture callus. The procedure for generating computer models of bone fracture calluses will be detailed below in a systematic stepwise demonstration. Note that the details of this current methodology represent the latest techniques and advancements that are apart from initial realizations and thus may differ slightly from those techniques and methods used in older studies presented within this document.

### *Segmenting the microCT image volume*

The process begins with the generation of a subject specific tibia fracture callus FE model. MicroCT image volumes of a bone fracture callus sample are obtained utilizing the imaging protocol detailed within the Experimental System Methodology sub-section. Once this image volume is obtained, two image segmentations must be performed. First, the entire bone/callus volume is segmented from the surrounding air interface through the use of a global threshold-based semi-automatic extraction tool in a commercially available image analysis software (Analyze, AnalyzeDirect), generating an image volume in which only the bone/callus region is visible. The results of this segmentation are shown in Figure 9A. Next, the cortical bone is similarly segmented

from the extracted bone/callus image volume. The results from this segmentation are shown in Figure 9B.

*Generating the boundary surface description*

Boundary surface descriptions for both the bone/callus volume and the cortical bone volume must then be generated from the segmented microCT image volumes in order to proceed to the mesh generation step. These boundary surface descriptions are described by 3D point positions and 3D triangular patches and are generated through the use of a marching cubes algorithm in a commercially available image analysis software (Analyze, AnalyzeDirect). The results from boundary surface extraction are shown in Figure 9C and Figure 9D.

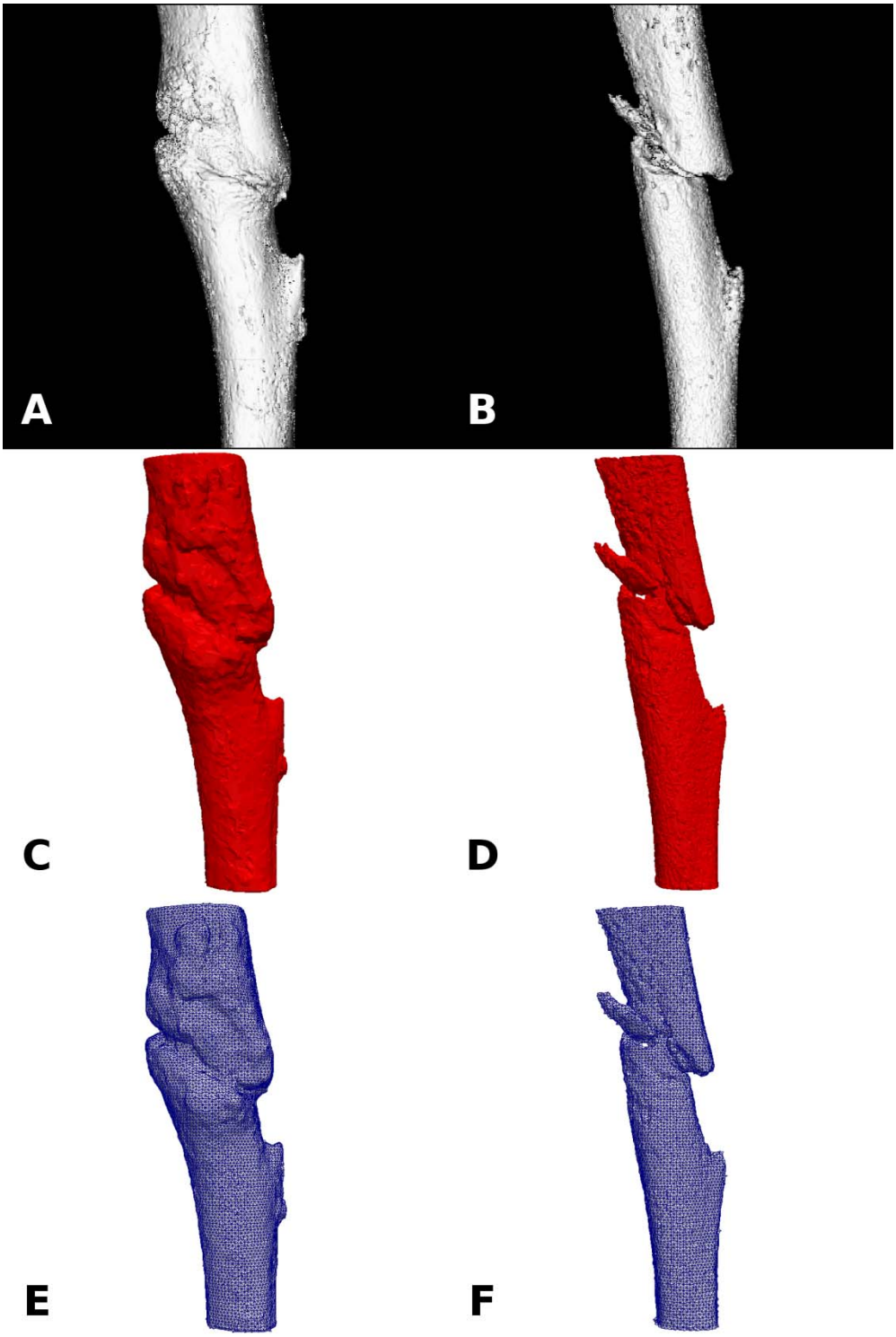


Figure 9. Representative images showing the construction of the model. (A) microCT image of the callus, (B) microCT image of the cortical bone, (C) boundary surface of the callus, (D) boundary surface of the cortical bone, (E) mesh of the callus, (F) thresholded mesh showing only the cortical bone.

*Generating the finite element mesh*

The boundary surface descriptions of each material are then used to create a heterogeneous FE tetrahedral mesh consisting of two properties (i.e. cortical bone and 'other' material) using custom-built mesh generation methods (SPMESH) [62]. The boundary surfaces and a mesh edge length parameter defining the coarseness of the mesh are defined and the mesh generator is executed, resulting in a tetrahedral FE mesh. For the purposes of this work, a mesh edge length was selected as ~ 0.05 mm, generating FE meshes on the order of 500,000 elements and 100,000 nodes. Following initial mesh creation, materials properties are assigned to the 'other' material that consists of either callus material or a void/air material (which accounts for empty spaces within the callus). An image-to-grid approach is utilized to define these materials which determines the voxel intensities within each tetrahedral element from the imaging domain and assigns properties based on a global threshold. An example tetrahedral FE mesh created using this methodology is shown in Figure 9E and Figure 9F.

*Laplacian model for 'cleaning' the mesh*

For many fracture callus FE models in which the cortical bone edges at the fracture gap are in close proximity to each other, the microCT scan reflects an incorrect connection between the cortical bone ends. This image artifact is caused by microCT imaging partial volume effects in which the external edge of the cortical bone occupies less than a full voxel dimension, generating an image intensity level for these voxels that is higher than air but lower than cortical bone. These partial volume effects serve to obfuscate the edges of the cortical bone, especially when the fractured cortical bone ends

are in close proximity to each other. This effect is magnified with lower image volume resolution. This artifact serves to render a minor incorrect connection between the cortical bone pieces. In cases which exhibit this artifact, the problem voxel connections must be removed (i.e. change the offending voxels' material property from cortical bone to callus) prior to modeling. If these connections were to remain during the modeling process, an incorrectly high force will be calculated during the forward FE model solution as the load transmission due to a given displacement would be transferred through the cortical bone connection. This phenomenon serves to greatly 'stiffen' the callus model.

In lieu of an arduous manual removal process in which offending voxels must be selected one-by-one by hand for further processing, a Laplacian-based modeling approach has been adapted to semi-automatically identify problem connecting voxel areas. In this approach, an incompressible fluid dynamics (Laplace's equation) problem is solved through FE analysis of the existing FE grid whereby fluid flow velocity potential boundary conditions of +1 and 0 are selected for all nodes at the top and bottom surfaces of the bone, respectively. The material properties are selected such that flow occurs only in the cortical bone material (cortical bone is selected to exhibit low flow resistance and callus is selected to exhibit high flow resistance).

Laplace's equation can be written as:

$$\nabla \cdot k\nabla u = 0$$

When this FE model is solved utilizing an in-house custom-built Laplacian FE solver, the steady-state velocity flow field is determined for each element contained within the grid. After calculating the rate of change of this flow field, the areas of voxel

connection between the top and bottom cortical bone segments can be determined. Logically, as fluid flow is only occurring within the cortical bone material, areas that represent geometrically small connections between the cortical bone ends (the offending voxels in question) will be observed to have a high rate of change of the flow field and can thus be automatically selected and reassigned through thresholding. As the flow field is in a steady-state condition, the boundary condition values will propagate along the cortical bone towards the fracture gap. In areas that connect the cortical bone ends, the velocity field will experience a large magnitude change, setting up a gradient of flow field between the bone ends ranging from +1 to 0. Taking the derivative of this flow field highlights the areas of connection. This procedure is visually presented in Figure 10.

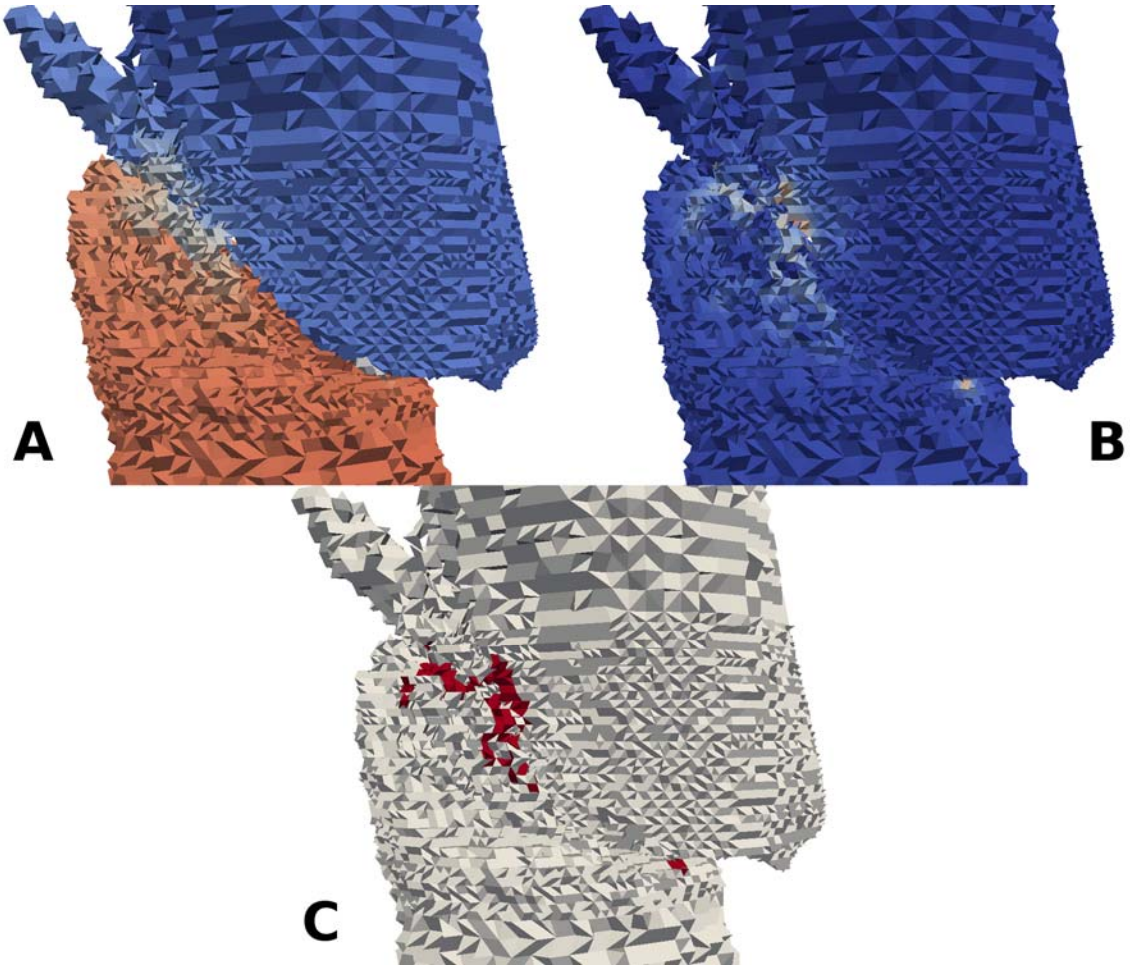


Figure 10. Results of the diffusion model zoomed to visualize the fracture gap: (A) flow field, (B) derivative of flow field, (C) removal of the connecting voxels. Elements highlighted in red in C represent elements that are removed to eliminate the cortical bone connection.

*Assigning boundary conditions and material properties*

Once the proper 3D mesh with correct material properties is created, boundary conditions are assigned. Boundary conditions are assigned as displacement and stress free as determined by comparisons to the BMT analysis. The top displacing surface is assigned Dirichlet (Type I) boundary conditions of rigid normal displacement, $u_n =$

$d$,$u_{t1} = 0, u_{t2} = 0$, and the bottom surface is fixed with Dirichlet boundary conditions, $u_n = 0, u_{t1} = 0, u_{t2} = 0$. The remainder of the surface nodes are assigned as stress-free (Neumann boundary conditions or Type II). The top and bottom surfaces are automatically selected by determining boundary surfaces nodes that fall within a preset distance tolerance of the maximum and minimum node height positions, respectively.

Values for the cortical bone and void space stiffnesses are assumed 5 GPa [63] and 0.1 Pa (many orders of magnitude below callus values), respectively. Values of Poisson's ratio are assumed for all tissue types (0.3 for bone and 0.45 for callus) based on the literature [46] and values associated with the near-incompressible nature of soft tissue. In addition, the cartilage and low-mineralized bone are lumped into a single isotropic property.

*Finite element model*

Upon generation of the bone fracture computer model, assigning material regions, and assigning boundary conditions, the inverse FE material property reconstruction procedure is ready for execution. Details of the forward FE model used to calculate the FE model force within the inverse procedure are given below.

For these analyses, isotropic linear elastic properties are assumed. The set of equations governing linear elastic deformation is given by:

$$\nabla \cdot G\nabla\vec{u} + \nabla\frac{G}{1-2\nu}(\nabla \cdot \vec{u}) = 0$$

where the shear modulus G is given by: $G = {}^{E}/_{2(1+\nu)}$, $\nu$ is Poisson's ratio, and $\vec{u}$ is the Cartesian displacement vector.

A numerical solution to the coupled set of partial differential equations is obtained using the weighted residual method. The method begins with standard weighting and integration:

$$\langle G\nabla\vec{u}\cdot\nabla\phi_i\rangle+\langle\frac{G}{1-2\nu}(\nabla\cdot\vec{u})\nabla\phi_i\rangle=\iint\sigma_s\cdot\vec{n}\,\phi_i dS$$

where $\langle\quad\rangle$ indicates integration of the problem domain and $\phi_i$ is the i[th] member of a set of scalar functions of position. The standard $C^0$ local Lagrange polynomial interpolants are used as the particular weighting functions. Using the Galerkin approach, the unknown displacement vector is expanded using a Lagrangian basis function for a standard linear tetrahedral element:

$$u(x,y,z)\approx\hat{u}(x,y,z)=\sum_{j=1}^{4}u_j\phi_j(x,y,z)$$

After substitution, the local weighted residual expression can be written for the i[th] equation and the j[th] displacement coefficients as:

$$[K_{ij}]\{\overrightarrow{u_j}\}=\{\overrightarrow{b_i}\}$$

where

$[K_{ij}]$

$$=\begin{bmatrix}G\langle\frac{2(1-\upsilon)}{1-2\upsilon}\delta_{xx}+\delta_{yy}+\delta_{zz}\rangle & G\langle\frac{2\upsilon}{1-2\upsilon}\delta_{yx}+\delta_{xy}\rangle & G\langle\frac{2\upsilon}{1-2\upsilon}\delta_{zx}+\delta_{xz}\rangle\\ G\langle\frac{2\upsilon}{1-2\upsilon}\delta_{xy}+\delta_{yx}\rangle & G\langle\delta_{xx}+\frac{2(1-\upsilon)}{1-2\upsilon}\delta_{yy}+\delta_{zz}\rangle & G\langle\frac{2\upsilon}{1-2\upsilon}\delta_{zy}+\delta_{yz}\rangle\\ G\langle\frac{2\upsilon}{1-2\upsilon}\delta_{xz}+\delta_{zx}\rangle & G\langle\frac{2\upsilon}{1-2\upsilon}\delta_{yz}+\delta_{zy}\rangle & G\langle\delta_{xx}+\delta_{yy}+\frac{2(1-\upsilon)}{1-2\upsilon}\delta_{zz}\rangle\end{bmatrix}$$

$$\{\overrightarrow{u_j}\}=\begin{Bmatrix}u_j\\v_j\\w_j\end{Bmatrix},\text{ and }\{b_i\}=\begin{Bmatrix}\vec{x}\cdot\oint\sigma\cdot\vec{n}\phi_i ds\\\vec{y}\cdot\oint\sigma\cdot\vec{n}\phi_i ds\\\vec{z}\cdot\oint\sigma\cdot\vec{n}\phi_i ds\end{Bmatrix},$$

and $\delta_{kl} = \frac{\partial \phi_j}{\partial k}\frac{\partial \phi_i}{\partial l}$

The local contribution from each tetrahedral element can then be determined and a global stiffness matrix constructed. Boundary conditions are applied and the matrix is then assembled and solved using an iterative matrix solver (Portable, Extensible Toolkit for Scientific Computation, PETSc), which uses a linear conjugate gradient solver with a Jacobi pre-conditioner. This results in a displacement solution for all nodes within the domain. After the displacement is calculated, the average surface stress can be estimated by utilizing the unused Galerkin equations on the Dirichlet boundary condition surfaces. Thus the following equation is available for each type I boundary condition node:

$$\iint \widetilde{\sigma_s} \cdot \vec{n}\, \phi_i dS = \Sigma_j \overrightarrow{u_j} \langle G \nabla \phi_j \cdot \nabla \phi_i \rangle + \Sigma_j \overrightarrow{u_j} \langle \nabla \phi_j \frac{G}{1-2\nu} \nabla \phi_i \rangle$$

The right hand side is constructed using the displacement solution and the left hand side surface integral for the local normal stress distribution can be solved. The surface stress is then averaged and multiplied by the model surface area to generate a FE calculated average force value for comparison to the respective experimental mechanical testing force.

*Inverse Problem Framework*

To determine the callus modulus, the model calculated average force ($F_{calc}$) is generated from an initial callus Young's modulus guess (E). A custom-built Levenberg-Marquardt non-linear optimization algorithm is used to iteratively optimize the modulus value such that $F_{calc}$ approaches the experimental material tester generated force ($F_{exptl}$). In this approach, each strain level is treated as an independent data point with respect to

determining the modulus. This allows the formation of an objective function from the elastic portion of the force-displacement data, i.e.

$$G(E) = \sum_{i=1}^{N} \left(F_{calc} - F_{exptl}\right)_i^2$$

where N is the number of data points along the elastic region of the force-displacement curve. In this case, we are solving for a single property which represents the elastic modulus (E) of the 'lumped' callus region. To optimize this for the callus modulus, we take the derivative of our objective function G(E) with respect to the modulus, and set equal to zero.

$$\frac{dG(E)}{dE} = \left[\frac{\partial F_{calc1}}{\partial E} \quad \cdots \quad \frac{\partial F_{calcN}}{\partial E}\right] \begin{Bmatrix} F_{calc1} - F_{exptl1} \\ \vdots \\ F_{calcN} - F_{exptlN} \end{Bmatrix}$$

or simplified as,

$$[J]^T\{\bar{F}_{calc} - \bar{F}_{exptl}\} = 0$$

where J is the Jacobian, which is a matrix of first-order partial derivatives of $F_{calc}$ with respect to the modulus.

From this, a standard Levenberg-Marquardt framework can be used to solve this root problem,

$$([J]^T[J] + \alpha I)\Delta E = [J]^T\{\bar{F}_{calc} - \bar{F}_{exptl}\}$$

where I is the identity matrix, $\Delta E$ is the change in material property for the iterative method, i.e.

$$E_{i+1} = E_i + \Delta E,$$

and $\alpha$ is a regularization term to improve the conditioning of the iterative procedure and is defined as,

$$\alpha = (\lambda * \text{trace}([J]^T[J]) * SSE^2)^{1/2} \qquad [64]$$

where λ is an empirical factor and SSE is the sum squared error between measured and calculated force. The Jacobian is determined by a finite difference calculation which was initiated by a 2.5% perturbation from the initial guess of the modulus. As schematically presented in Figure 8, the process is repeated until the relative error between iterations converges below a set tolerance or until no improvement in objective function is noted.

## Experimental System Methodology

### *Mouse stabilized tibia fracture model*

Female syngenic FVB mice (FVB-NJ, Jackson Laboratories) 8 to 12 weeks old are anesthetized using isofluorane to provide deep anesthesia. Pin stabilized mid-diaphaseal tibia fractures are generated by insertion of a 0.25 mm stainless steel pin (Fine Science Tools) through the tibial tuberosity followed by fracture creation using a three point impact bending device (Figure 11) with a standardized force. Immediately following tibia fracture, 0.5 mg/kg of bupremorphine is administered for pain control. On post fracture days 10, 14 and 21, mice are euthanized, fractured tibias are dissected and wrapped in PBS soaked gauze and stored at -80 °C until further analysis. This stabilized tibia fracture model exhibits complete fracture healing by 28 days (Figure 12). All animal studies are approved by the Institutional Animal Care and Use Committee at Vanderbilt University and University of North Carolina at Chapel Hill.

Figure 11. Fracture creation device.

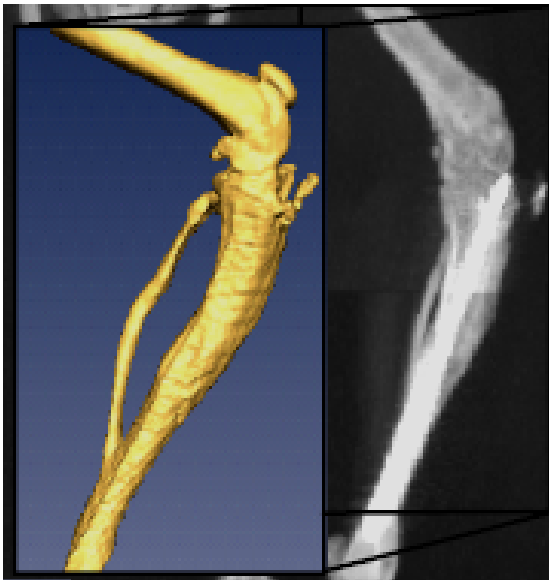

Figure 12. Standardized tibia fracture callus (28 days post-fracture).

*Isolation, expansion, and transplantation of MSC*

Primary cultures of BM-MSC are obtained by flushing the bone marrow from femurs and tibias of 4-6 weeks old FVB-NJ mice, as shown in Figure 13 and previously reported [65]. Briefly, BM nucleated plastic-adhering cells are expanded for 7-10 days

without passaging [65]. Immediately before transplant, contaminating hematopoietic cells are eliminated by immunodepletion of the CD45, CD11b and CD34 positive cells using a MACS magnetic separation system (Miltenyi-Biotech). As shown in [1], using this protocol a MSC population is obtained, in which >90% of cells express the specific MSC markers CD73, CD29, CD44, and 67.5% the CD105 marker. After fracture, mice selected to receive MSC are transplanted with $10^6$ MSC by tail vein injection.

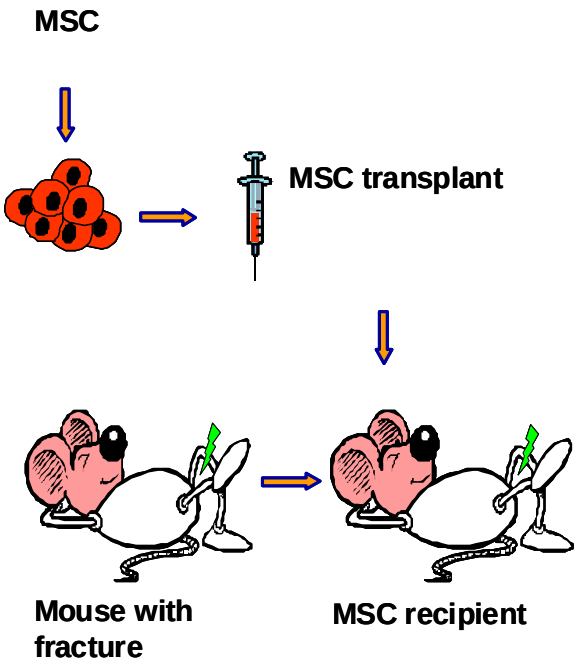


Figure 13. Schematic of MSC transplantation

*MicroCT callus imaging*

MicroCT scans are performed using a Scanco microCT 40 scanner (Scanco Medical) utilizing scan parameters of 55 kVp, 145 μA, 300 ms integration time using 12 μm voxel resolution along a standardized length centered at the fracture line with a total scanning time of approximately 1 hour per sample [66]. MicroCT reconstructions are

used for subsequent FEA analysis and volume measurements. To quantify callus volume, microCT images are thresholded according to a separate material type thresholding study, and volume measurements performed, such as total bone volume and total callus volume. Total bone volume is determined by summing the voxels corresponding to mineralized tissue (new bone and cortical bone), then multiplying by the voxel resolution. Total callus volume is determined by summing the voxels corresponding to callus tissue (soft tissue and new bone), then multiplying by the voxel resolution.

*Biomechanical testing*

To eliminate the dependence of bone/callus material properties with hydration, tibias are kept fully hydrated with PBS during the entire testing procedure. Tibias are prepared for mechanical analysis by embedding each of the bone ends in polymethylmethacrylate cast into custom designed testing fixtures, leaving the fracture callus exposed. The fixtures are loaded into either an Enduratec Electroforce 3100 or 3200 mechanical tester (Bose, Enduratec Systems Group) and tested in tension at a fixed displacement rate of 0.25 mm/min using a 22 N transducer (Honeywell Sensotec) for force data [67]. Displacement and force data are recorded until failure and used for subsequent FEA analysis and to determine biomechanical metrics of fracture healing such as ultimate load, toughness, apparent stiffness, and normalized apparent stiffness (Figure 14). Ultimate load is defined as the peak force recorded during the BMT procedure. Toughness is defined as the area under the Force vs. displacement curve from the origin to the point of ultimate load. Apparent stiffness is defined as the slope of a best fit line to the linear portion of the force versus displacement curve during the loading

phase. Normalized apparent stiffness is defined as apparent stiffness with the force and displacement values normalized by dividing by the largest cross-sectional area of the callus and its overall length, respectively.

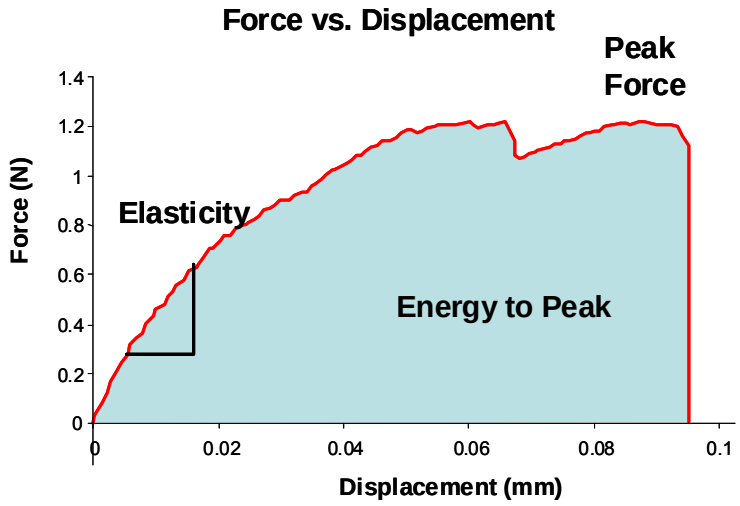


Figure 14. Determination of BMT metrics of fracture healing.

# CHAPTER III

# A FINITE ELEMENT INVERSE ANALYSIS TO ASSESS FUNCTIONAL IMPROVEMENT DURING THE FRACTURE HEALING PROCESS

## Introduction and Contribution of Study

This study is the first in regards to the fracture callus inverse FE analysis, and the experimental methods presented within this work represents the initial development of the analysis procedure. The initial evidence for the feasibility of inverse FE analysis of fracture callus is demonstrated within this work, as 10 day post-fracture calluses are compared to 14 day post-fracture calluses through microCT imaging, biomechanical testing, and inverse FE analysis. As this study represents a logical experimental system in which mechanical integrity should increase with time while the fracture is in an active healing phase, the evidence of a significant difference between groups as determined by inverse FE analysis serves as a proof-of-concept of inverse FE analysis as a fracture healing functional assessment method. Additionally, validation of the analysis methodology is presented within this study in simulation studies in order to confirm the inverse FE procedure. In particular, simulation studies were performed to: validate the inverse model reconstruction of material property values from geometries with known material properties, determine the sensitivity of the inverse procedure with respect to varied initial guess, determine the sensitivity of the inverse procedure with respect to mechanical testing transducer noise, and determine the sensitivity of the inverse procedure with respect to the assumed cortical bone property. The primary motivation

for this study was to enhance the level of sensitivity of functional fracture healing assessment in order to more reliably determine improvement (or impairment) in the fracture healing process. Traditional fracture healing assessment methods are limited by a lack of sensitivity and/or a lack of direct functional assessment applicability. Therefore the motivation was to develop a fracture callus assessment method that is both more sensitive and directly functionally related in nature in order to more reliably detect changes in the healing process. This study was also the first to report the application of inverse FE analysis methodology to the assessment of bone fracture healing. This study was published in the Journal of Biomechanics in 2010.

Appearing in:

Jared A. Weis, Michael I. Miga, Froilan Granero-Molto and Anna Spagnoli. A finite element inverse analysis to assess functional improvement during the fracture healing process. Journal of Biomechanics, Volume 43, Pages 557 - 562, January 2010.

## Abstract

Assessment of the restoration of load-bearing function is the central goal in the study of fracture healing process. During the fracture healing, two critical aspects affect its analysis: (1) material properties of the callus components, and (2) the spatio-temporal architecture of the callus with respect to cartilage and new bone formation. In this study, an inverse problem methodology is used which takes into account both features and yields material property estimates that can analyze the healing changes. Six stabilized fractured mouse tibias are obtained at two time points during the most active phase of the

healing process, respectively 10 days (n=3), and 14 days (n=3) after fracture. Under the same displacement conditions, the inverse procedure estimations of the callus material properties are generated and compared to other fracture healing metrics. The FEA estimated property is the only metric shown to be statistically significant (p=0.0194) in detecting the changes in the stiffness that occur during the healing time points. In addition, simulation studies regarding sensitivity to initial guess and noise are presented; as well as the influence of callus architecture on the FEA estimated material property metric. The finite element model inverse analysis developed can be used to determine the effects of genetics or therapeutic manipulations on fracture healing in rodents.

## Introduction

Approximately 10-20% of the 6.2 million annual bone fractures result in non-unions, causing significant morbidity and mortality [4, 5]. In long-bones, fracture healing proceeds through the formation of a cartilaginous template that is then replaced by bone that undergoes remodeling [2]. A critically important function of bone healing is that the healing tissue provides sufficient mechanical stabilization such that a return to functionality is possible. Experimental studies on fracture healing have largely been dependent on rodent models. However, the lack of sensitive methods to monitor and relate the fracture mechanical properties with tissue type renders those studies inadequate to fully evaluate the fracture healing patho-physiology.

Assessment of fracture healing has relied on histological, imaging, and biomechanical testing (BMT) [26]. Histological methods allow the visualization of tissue-specific molecules over histological sections by in-situ hybridization,

immunohistochemistry, or specific staining. However, comparisons between sections are difficult and true quantitative assessment is unrealistic. Furthermore, histological methods are limited to *post-mortem* analysis and cannot provide functional information. Various imaging modalities have been used to assess the fracture healing, such as micro-computed tomography (microCT), magnetic resonance, and positron emission tomography [27-34]. MicroCT imaging is mostly used due to advantages in 3D reconstructions. However, imaging provides no information about tissue types and mechanical properties. BMT remains the gold standard for the functional assessment of fracture healing. Standard BMT analyses use force versus displacement data and analytic calculations based on beam theory to generate mechanical property information. Beam theory calculations rely on the assumption of a homogeneous cross section, but because of the irregular geometry of the callus, these calculations are strongly biased by geometrical factors [44].

Some studies have explored coupling microCT imaging with finite element analysis (FEA) to predict the mechanical behavior based on geometrical information. In particular, studies have evaluated microCT attenuation to stiffness value transformations to provide material properties and found empirical power law relationships between modulus and bone mineral content assessed by microCT attenuation/density [45, 46]. Shefelbine and colleagues have also reported a weak correlation between predicted and experimental torsional rigidity with a very poor predictive value in calluses studied at early healing stages when mineralization is low [45, 46]. It is quite apparent that the direct relationship between microCT attenuation/density and mechanical parameters is unclear and is to some degree unsatisfactory; and when factoring in the potential for

variability of this relationship across experimental systems, it is unlikely that the correlation will improve.

In our studies, rather than using a μCT-to-stiffness empirical relationship, we have used an elastographic approach to directly generate values for mechanical parameters. Our approach combines an inverse finite element model of the subject's cartilage/bone geometry (microCT/histological imaging data), data acquired from BMT, and numerical optimization techniques to characterize the callus mechanical properties. This approach does not require calibration per system but rather is an active reconstruction parameter that can be measured experimentally. The concept of an 'inverse' FE analysis method to determine the mechanical parameters to monitor the progression of fibrogenic diseases has been demonstrated. These techniques are more widely referred to as elastography [47-53]. Within this work, the approach is used to evaluate mechanical properties as a biomarker in the assessment of fracture healing progression. Quantifying the change in mechanical properties during the fracture healing process may provide information that: (1) allows to determine when healing has failed to progress, (2) suggests the need for intervention in non-union/slow healing fractures, and (3) evaluates the effectiveness of treatments that aim to enhance the healing process through the formation of more mechanically competent tissue.

## Methods

### Generation of the computational model

An inverse FEA procedure was developed to determine the stiffness of the callus based on microCT imaging and BMT data. As summarized in Figure 15, the procedure

begins with the establishment of an assumed Hookean linear elastic tissue model framework for the bone/callus system. The process continues with the development of a bone/callus computer model of the subject generated from microCT image volumes. A volumetric tetrahedral grid is then generated to represent a FE mesh system.

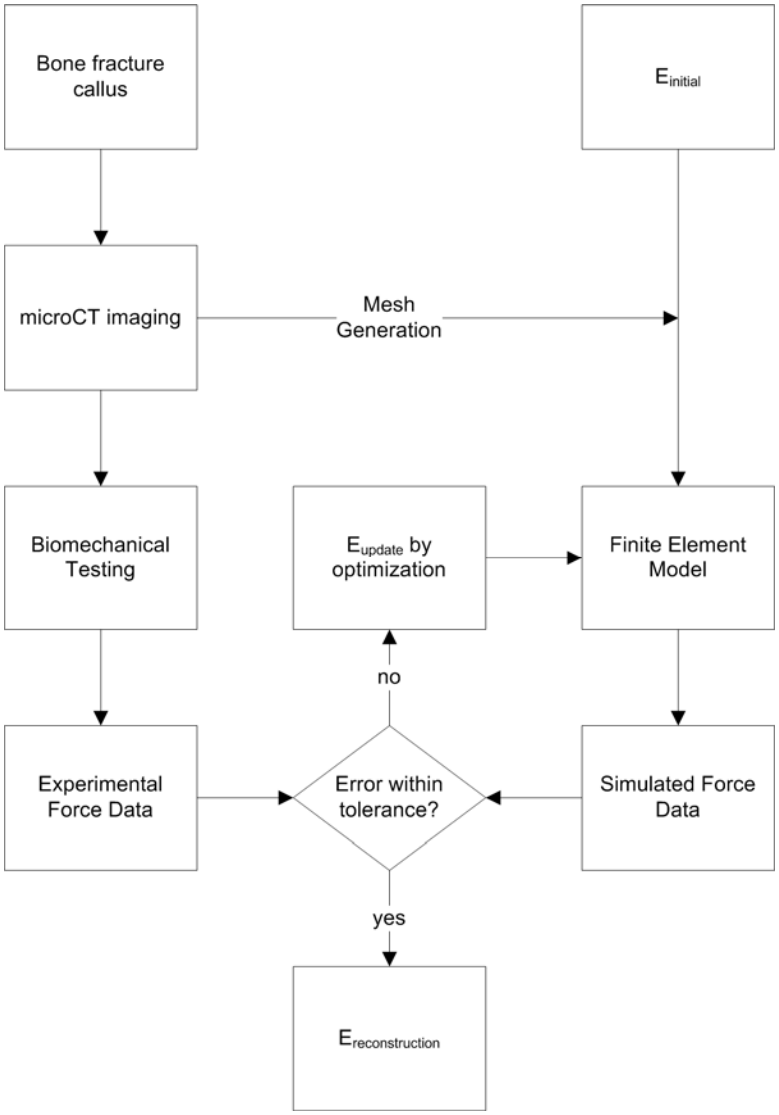


Figure 15. General framework of the inverse material property estimation method. The modulus of elasticity is iteratively determined by comparing model calculated forces to BMT forces.

The boundary conditions for the model were chosen to reflect the BMT protocol, in which the top boundary is prescribed a fixed upward normal displacement with no lateral displacement (Dirichlet boundary conditions). The bottom surface was also fixed in both the normal and lateral direction. The remaining boundary conditions for the sides of the model were stress free. The displacement criteria selected for each sample was based on the individual force/displacement curve obtained from BMT. A series of four displacements were taken along the curve at 25%, 50%, 75%, and 100% of the linear elastic limit to reproduce the linear portion of the curve. As pointed out in Figure 16, the linear elastic limit was defined as the point at which the curve exhibited plastic deformation (slope $\leq 0$ in our case). Solutions to the elastic system are then generated as reported previously [47]. As shown by Barnes and colleagues, the unused Galerkin equations associated with the implementation of the Dirichlet boundary conditions are utilized post model-execution to estimate the local boundary stress [47]. This stress is then averaged over the tensile boundary surface and multiplied by the surface area to generate a model-calculated average force ($F_{calc}$) applied to the bone surface for the given displacement. The model is solved at each displacement value to generate 4 model-calculated average forces which are compared to the corresponding forces measured from the force/displacement curve in a least squares sense and properties of the callus determined through an iterative optimization process. A further discussion of the inverse problem framework is discussed the Supplemental Material.

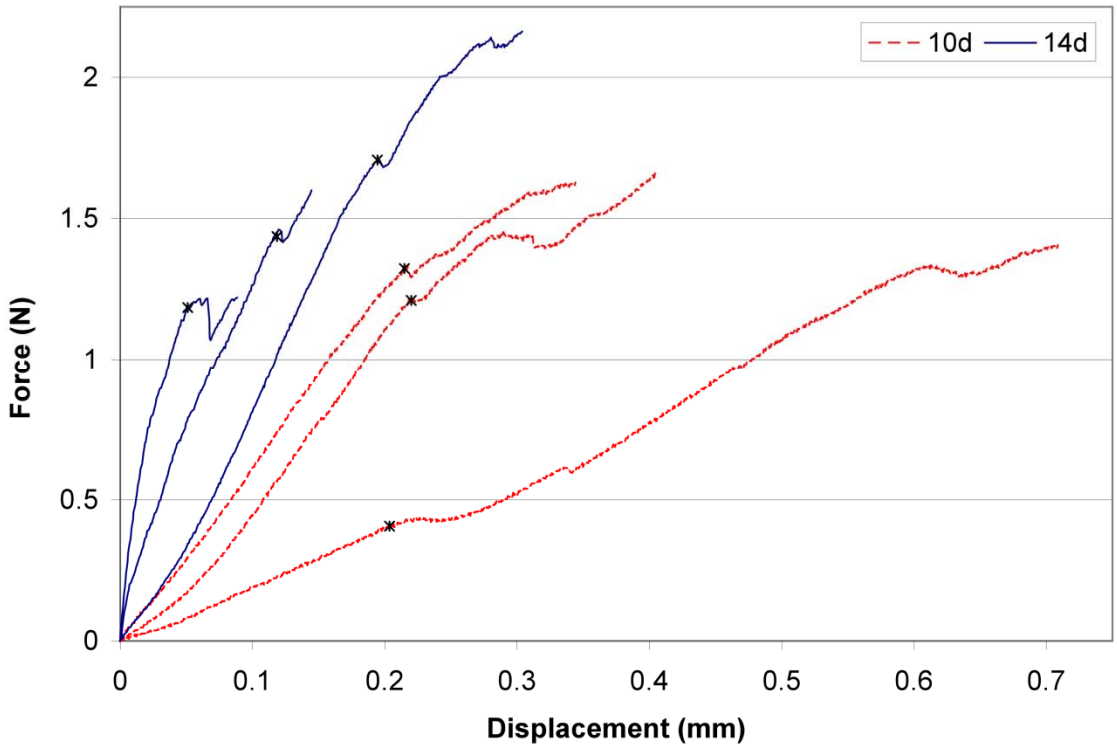


Figure 16. BMT force versus displacement data of each tibia fracture callus tested at day 10 and day 14 post fracture during tensile testing. Note the wide sample variation within each group, demonstrating confounding geometrical effects. Asterisk denotes linear elastic limit.

Experimental model

*Mouse stabilized tibia fracture model*

Female FVB-NJ mice (Jackson Laboratories) 8-12 weeks old were anesthetized using isofluorane to provide deep anesthesia. Pin stabilized mid-diaphyseal tibia fractures were generated by insertion of a 0.25 mm stainless steel pin (Fine-Science-Tools) through the tibial tuberosity followed by fracture creation using a three-point bending device with a standardized force. Immediately following tibia fracture, 0.5 mg/kg of bupremorphine was administered for pain control. On post-fracture days 10 and 14, mice were euthanized, fractured tibias were dissected and wrapped in PBS

soaked gauze and stored at -80 °C until further analysis. Animal studies were approved by the Institutional Animal Care and Use Committee at Vanderbilt University Medical Center and the University of North Carolina at Chapel Hill.

*microCT callus imaging and microCT/histological thresholding analyses*

μCT scans were performed using a Scanco microCT 40 scanner (Scanco Medical) and were obtained at 55 kVp, 145 μA, 300 ms integration time using 12 μm voxel resolution along 5.2 mm length centered at the fracture line [66]. microCT reconstructions were used for subsequent FEA and volume measurements. To determine material type (newly mineralized bone, highly mineralized bone and cartilage) and quantify callus volumes from microCT scans, a parametric thresholding study was performed by serial microCT scanning and histological analysis as more extensively reported within the Supplemental Material.

*BMT analyses*

Fractured tibia ends were embedded into a polymethylmethacrylate cast using custom designed testing fixtures, leaving the fracture callus exposed. Specimens were kept fully hydrated with PBS during the entire testing procedure. The fixtures were loaded into an Enduratec Electroforce 3100 mechanical tester (Bose, Enduratec Systems Group) and tested in tension at a fixed displacement rate of 0.25 mm/min using a 22 N transducer (Honeywell Sensotec) for force data [67]. Displacement and force were recorded until failure and used for subsequent FEA and to determine biomechanical

metrics of fracture healing. Additional descriptions can be found in the Supplementary Material.

*Generation of subject specific FE models*

Subject specific FE models were generated for 6 tibias (three each at 10 and 14 days post-fracture). After using the imaging protocol above, microCT image sets were semi-automatically segmented and boundary descriptions (as described by 3D points and 3D triangular patches) were generated through the use of a marching cubes algorithm in a commercially available image analysis software (Analyze, AnalyzeDirect) for both the entire bone/callus and solely the cortical bone. Boundary descriptions of each were then used to create a heterogeneous FE tetrahedral mesh consisting of two properties (i.e. cortical bone and other material) using custom-built mesh generation methods [62]. Once the 3D mesh is created, an image-to-grid approach is utilized which determines the voxel intensities within each tetrahedral element from the imaging domain and assigns properties based on thresholding.

Values of Poisson's ratio were assumed for all tissue types (0.3 for bone and 0.45 for callus) based on the literature [46] and values associated with the near-incompressible nature of soft tissue. In addition, the cartilage and low-mineralized bone were lumped into a single isotropic property. The value of the void space elastic modulus was assumed as 0.1 Pa (many orders of magnitude below callus value). Reported values of the cortical bone modulus range from ~4 GPa to ~21 GPa [63, 68, 69]. Because of this large variability, we tested the inverse FEA modulus estimations to explore the impact of different cortical bone modulus values using respectively 5, 10 and 15 GPa. As reported

in Table 4 within the Supplementary Material, we found that the estimated callus elastic modulus did not change with the assumed cortical bone modulus (maximum of ~4.5% difference, not statistically significant). Thereafter, the 5 GPa value has been used in all the studies performed.

Simulation studies

A cylinder mesh with three layers was created to simulate a simplified appearance of a bone fracture callus, as seen in Figure 17. The simplified geometry allows analytic comparisons to FEA results. Simulations were then performed on the cylinder mesh to test the accuracy and sensitivity of the inverse FEA procedure upon initial guess, with material properties approximating that of bone and callus (5 GPa and 1 MPa, respectively) and radius and total height of 1 mm and 6 mm, respectively. To gauge accuracy of the simulations, the forward elastic model was used to calculate boundary normal surface forces for a step displacement corresponding to 0.5% strain and compared to an analytic calculation of the surface normal force (derivation in Supplementary Material). The dependence of the elastographic framework on initial guess was also tested by executing simulations with five random initial callus modulus guesses.

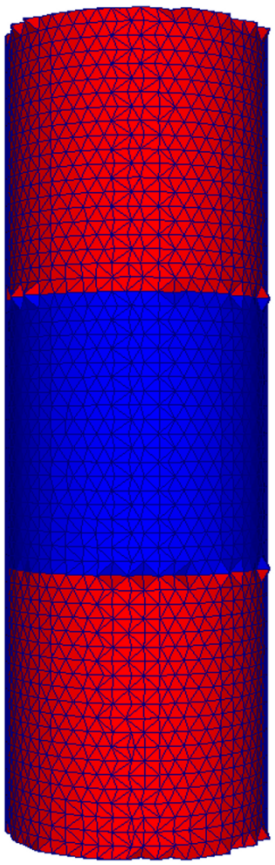

Figure 17. Cylinder mesh representing a simplified appearance of a bone fracture callus used for simulation studies. The proximal and distal layers represent the bone ends (red), while the intermediate layer represents callus (blue). Each geometrically identical layer is assumed to be a homogeneous material of dimension similar to that of a bone fracture callus.

In a separate simulation study, two meshes created from microCT imaging of a representative post-fracture day 10 and 14 tibia were used as realistic geometries for further simulation analyses. To examine the effect of mineralization compositional differences in the callus on the estimated lumped elastic modulus parameter, meshes at the two time points (representing two different phases of mineralization) were used to estimate the combined callus modulus. The callus material in the mesh was subdivided

into new bone and soft tissue portions and assigned separate Young's modulus values of 10 MPa and 0.1 MPa, respectively (values were arbitrarily selected to fit to actual experimental results, but are based on magnitude differences of 100 fold that have been previously suggested [46]). The effect of transducer noise on the inverse FEA method was also examined through the addition of Gaussian noise.

Ex vivo studies

Day 10 and 14 post-fracture tibias were subjected to the material property estimation analysis, whereby force versus displacement curves obtained from the mechanical tests were used in conjunction with the meshes generated from microCT scans to determine callus material properties. In addition, the following metrics were analyzed: (1) ultimate load, (2) toughness, (3) apparent stiffness, (3) normalized apparent stiffness, (4) total bone volume, and (5) total callus volume. More details are reported in the Supplementary Material.

Statistics

Data are expressed as mean ± SD. Statistical analyses were performed using unpaired Student's t-test, The Graph-pad Prism Software and the Power and Sample Size package software were used. Statistical significance was set at $p<0.05$; statistical power was set at 0.9.

# Results

## Simulation 1: Validation of the FEA model

To validate the FEA model, the simulation cylinder mesh was compared against an analytic calculation. The model was prescribed fixed displacement of 0.5% strain and the average normal surface force was calculated from the forward FEA model as described in the Methods. The average surface normal forces were calculated as 45.0347 mN and 47.1050 mN for the model and analytic calculations, respectively, representing a 4.40 percent error in the model versus the analytic calculation, which is reasonable given the level of discretization and the type of element used.

## Simulation 2: Sensitivity of material property estimation on initial guess

To determine the sensitivity of the material property estimation method, the forward FEA model was run as described in the Methods to generate model calculated average surface normal forces at 4 strain increments (0.5, 1.0, 1.5, and 2.0 percent strain). These results were then used as the "experimental force transducer" input along with multiple random initial guesses for the callus material property. The material property estimation was executed with varying initial guesses to determine the accuracy of the model to converge on the known material property given a random initial material property guess. As shown in Figure 18, the solution to the material property estimation converged to the correct value of 1 MPa (within 1.74 % maximum error) for all initial guesses tested.

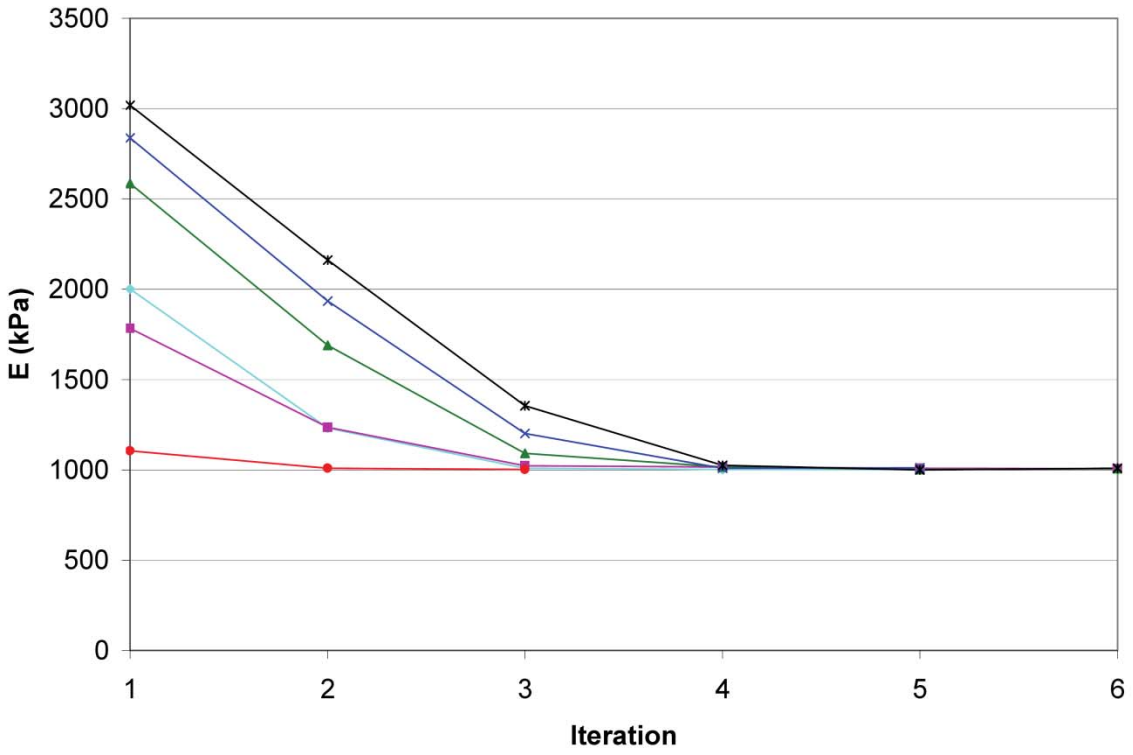


Figure 18. Convergence plot of cylinder mesh simulation with varying initial guess. The modulus of elasticity (E) converged to the optimal solution (1000 kPa) for all initial guesses tested.

Simulation 3: Lumped parameter estimation and sensitivity of force transducer error

Representative callus meshes from 10 and 14 days post-fracture were used in simulations in which the callus was subdivided into new bone and soft tissue with modulus values as described in the Methods. The forward model was used to determine boundary normal surface forces for displacements of 0.1, 0.2, 0.3, and 0.4 mm, which were then used as the transducer force inputs to the inverse FEA with one lumped parameter corresponding to the total bulk callus modulus of elasticity. As shown in Table 2, the estimated callus moduli were 1930 and 3538 kPa for the 10 and 14 day post-fracture callus meshes, respectively. These data demonstrate that changes to the new

bone volume fraction (new bone/callus volume) between days 10 and 14 post-fracture result in an estimated bulk modulus of ~ 2 fold. This simulation provides some understanding of how a lumped parametric model is affected by the new bone volume fraction. The effects of transducer noise was simulated by generating noisy data sets through the addition of random Gaussian noise of 0, 1, 2, 4 and 8 standard deviations of the force transducer's listed accuracy [± 0.15 % of full scale (22 N)] to each force data point on the loading curve of the previous simulation. The noisy data sets were used to define the effects of force transducer noise on the estimated material property accuracy. As shown in Table 2, the maximum error in the stiffness estimation procedure was observed as 3.89% for the addition of 8 standard deviations of transducer noise (an unreasonable case). For the realistic scenario of 1 standard deviation of noise, the error in estimation was 9.83 kPa and 12.97 kPa, corresponding to 0.51% and 0.37% error for the 10 and 14 day calluses, respectively. This suggests that transducer noise plays little part in the overall error of the method.

Table 2. Simulation results of estimated callus elastic modulus and effects of simulated transducer noise through the addition of 0, 1, 2, 4, and 8 standard deviations of noise.

| **Standard deviation of noise** | **$E_{model,10d}$ (kPa)** | **% error in $E_{10d}$** | **$E_{model,14d}$ (kPa)** | **% error in $E_{14d}$** |
|---|---|---|---|---|
| **0** | 1930 | 0 | 3538 | 0 |
| **1** | 1920 | 0.5094 | 3525 | 0.3667 |
| **2** | 1919 | 0.5870 | 3543 | 0.1355 |
| **4** | 1949 | 0.9651 | 3553 | 0.4193 |
| **8** | 1855 | 3.891 | 3471 | 1.903 |

Simulation 4: Material property estimation in mouse tibia fracture callus

Representative microCT reconstructions, corresponding meshes, and cross-sections of the meshes for both 10-day and 14-day groups are shown in Figure 19. microCT volume quantifications reported in Table 3, showed a trend over an increase of callus volume and mineralization in 14 versus 10 days post-fracture. Model generated material property estimations are also compared to other biomechanical fracture healing analysis metrics (apparent stiffness, normalized apparent stiffness, and callus volume). The inverse FEA was the only test to be statistically significant in estimating a modulus that was ~4 fold increased in the 14 days post-fracture calluses compared to day 10 post-fracture (Table II). With 3 mice in each group the inverse FEA had the statistical power to detect a difference (power=0.9, alpha=0.05) between groups. These data indicate that

the inverse FEA approach is sensitive to detect architectural changes that occur within the callus during the mineralization process. Although the unprocessed BMT data generated a trend of increasing stiffness for the 14 day over the 10 day post-fracture specimens, this parameter as well as all the others measured did not reach statistical significance. A large data variation was observed between samples, as clearly shown in Figure 16 that depicts the unprocessed BMT data for each sample. This large sample variation persisted following normalization of the apparent stiffness by maximal cross-sectional callus area and length, indicating the inadequacy of these types of normalizations.

Table 3. Comparison of BMT and CT fracture healing analysis metrics with estimated callus elastic modulus for 10 and 14 days post fracture samples. Numbers are expressed as mean +/- SD and P values are reported using unpaired Student's t-test. * denotes statistically significant difference.

| | **10 d (n=3)** | **14 d (n=3)** | **P Value** |
|---|---|---|---|
| **Ultimate Load (N)** | 1.560 ± 0.1370 | 1.643 ± 0.4888 | 0.7902 |
| **Toughness (N*mm)** | 0.4059 ± 0.08796 | 0.1957 ± 0.1567 | 0.1127 |
| **Apparent Stiffness (N/mm)** | 4.744 ± 2.345 | 13.95 ± 6.241 | 0.0751 |
| **Normalized Apparent Stiffness (kPa)** | 3885 ± 1800 | 8330 ± 4941 | 0.2170 |
| **Total Bone Volume (new bone + cortical bone) (mm^3)** | 4.051 ± 0.1183 | 5.894 ± 1.355 | 0.0788 |
| **Total Callus Volume (soft tissue + new bone) (mm^3)** | 4.391 ± 1.051 | 8.772 ± 3.772 | 0.1257 |
| **$E_{estimated}$ (kPa)** | 797.1 ± 414.3 | 2908 ± 872.8 | 0.0194* |

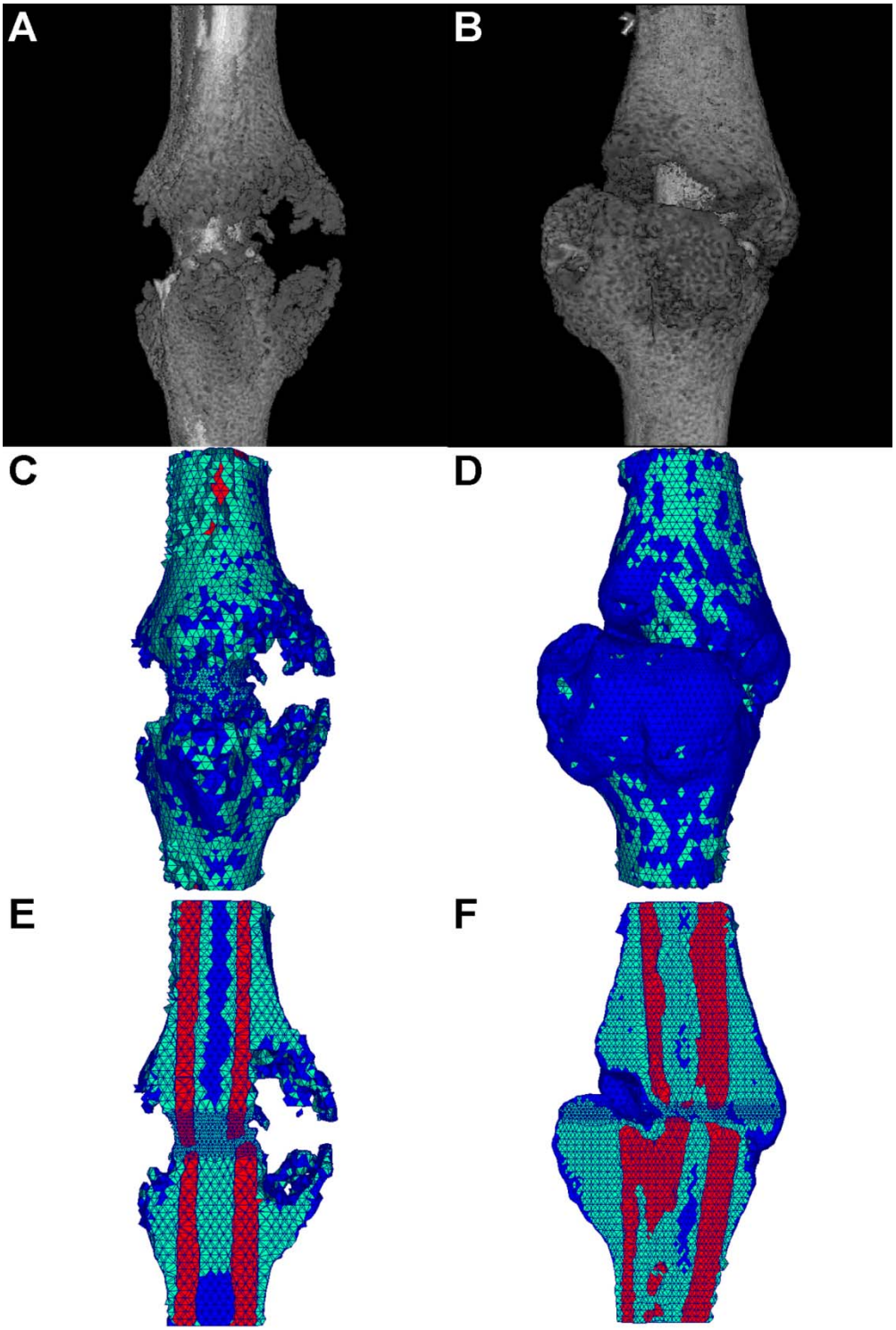


Figure 19. (a,b) Representative μCT 3-D reconstructions for mouse tibia fracture, (c,d) corresponding tetrahedral FE meshes, (e,f) cut-away images of the tetrahedral FE meshes showing internal elements and material types. Element colors represent material type of bone (red), callus (green), and void (blue). (a,c,e) 10 day post fracture, (b,d,f) 14 day post fracture.

## Discussion

In this study we have developed an inverse FEA procedure to determine the elastic modulus in mouse tibia fracture callus based on μCT/histological threshold data and data acquired from tensile BMT analyses. The FEA showed: 1) less than 5% error compared to the analytic calculations; 2) a sensitivity of material property estimation within 1.74% maximal error; 3) to be appropriately sensitive in estimating the modulus changes expected during two distinct time points of the fracture healing process.

The healing length of the stabilized mouse tibia fracture model is ~28 days [70]. We have performed our studies at post-fracture days 10 and 14. As assessed by histological analyses in this time window the callus is in its most active healing phase and has not yet reached the remodeling phase [70]. It is reasonable to assume that the mechanical properties of the callus should become progressively better and more functionally stable over time. As a result, metrics focused at assessing healing should improve between these time points. BMT has been considered the gold-standard technique to assess the mechanical properties of the callus and therefore the healing progression. However, in our studies we found that BMT was not sensitive to detect significant differences in any of these metrics between the time points studied. It is likely that the mechanical improvement has been masked by confounding geometrical factors that determined a wide data variation, even after maximal cross-sectional area and callus length normalizations. These BMT data, left alone, would have led to the paradoxical conclusion that a rapid healing progression would not be reflected by an improvement in mechanical stability. This lack of BMT sensitivity clearly highlights the need for alternative methods to detect material property changes during the healing process. Since

the large variance of the apparent stiffness measurements, it is possible that the inability of this method to detect a difference may be due to the small sample size. We estimated that 6 mice for each group would have been needed to get a statistical power of 0.9. On the other hand, using equal power analysis, only 3 mice for each group were needed to detect a difference between groups using the inverse FEA model. This indicates that because of the small variance, our model is powerful in detecting subtle differences in material properties therefore reducing the usage of mice, experimental time and expenses.

Through simulation studies, the inverse FEA approach developed in this work is shown to accurately calculate surface normal forces and to converge on a preset modulus value using random initial guess in the presence of transducer noise. Through ex vivo specimen analysis, the approach was able to detect a difference in the callus material modulus of ~4 fold from post-fracture day 10 to day 14. Taken together with the simulation analysis of callus meshes with both new bone and cartilaginous tissue material components, these data suggest that between 10 and 14 days post-fracture, there is a significant change in material composition (new bone volume fraction) that results in stiffness increase. In future studies, the inverse FEA approach will allow for establishing the temporal pattern of material property changes throughout the entire course of the healing process in normal and genetically/therapeutically manipulated fracture calluses.

In our model we have only incorporated the linear component of the force/displacement curves, but fracture healing can also be characterized by both geometrical and material nonlinearities. We recognize that our model in lacking the nonlinear component has some limitations, however, as depicted in Figure 16 the linear component accounts for 75 ± 24.2% of the curve(s) indicating that a significant amount of the callus follows a linear

modality in force/displacement testing. We acknowledge that this analysis only begins to address the question of constitutive modeling, but, it is important in that it demonstrates that first order approximations of subject specific models offer discriminatory power regarding fracture healing state analysis.

Supplementary Material

Table 4. Comparison of estimated callus elastic modulus for 10 and 14 days post fracture samples with differing values for cortical bone elastic modulus. Numbers are expressed as mean +/- SD and P values are reported using unpaired Student's t-test. * denotes statistically significant difference between 10 and 14 day groups.

| | **10 d (n=3)** | **14 d (n=3)** | **P Value** |
|---|---|---|---|
| **$E_{estimated}$ (kPa) w/ $E_{cortical}$ = 5 GPa** | 797.1094 ± 414.295 | 2908.294 ± 872.809 | 0.0194 * |
| **$E_{estimated}$ (kPa) w/ $E_{cortical}$ = 10 GPa** | 762.4152 ± 404.8187 | 2813.223 ± 825.9909 | 0.0181 * |
| **$E_{estimated}$ (kPa) w/ $E_{cortical}$ = 15 GPa** | 769.7466 ± 385.6674 | 2788.968 ± 786.6818 | 0.0162 * |

Appendix I: Additional descriptions of methods

*Inverse problem framework*

To determine the callus modulus, the model calculated average force ($F_{calc}$) is generated from an initial callus Young's modulus guess (E). A custom-built Levenberg-Marquardt non-linear optimization algorithm is used to iteratively optimize the modulus value such that $F_{calc}$ approaches the experimental material tester generated force ($F_{exptl}$).

In this approach, each strain level is treated as an independent data point with respect to determining the modulus. This allows the formation of an objective function from the elastic portion of the force-displacement data, i.e.

$$G(E) = \sum_{i=1}^{N} \left(F_{calc} - F_{exptl}\right)_i^2$$

where N is the number of data points along the elastic region of the force-displacement curve. In this case, we are solving for a single property which represents the elastic modulus (E) of the 'lumped' callus region. To optimize this for the callus modulus, we take the derivative of our objective function, G(E) and set equal to zero.

$$\frac{dG(E)}{dE} = \left[\frac{\partial F_{calc1}}{\partial E} \quad \frac{\partial F_{calc2}}{\partial E} \quad \cdots \quad \frac{\partial F_{calcN}}{\partial E}\right] \begin{Bmatrix} F_{calc1} - F_{exptl1} \\ F_{calc2} - F_{exptl2} \\ \vdots \\ F_{calcN} - F_{exptlN} \end{Bmatrix} = 0$$

or simplified as,

$$[J]^T \left\{\overline{F}_{calc} - \overline{F}_{exptl}\right\} = 0 .$$

From this, a standard Levenberg-Marquardt framework can be used to solve this root problem,

$$\left([J]^T [J] + \alpha I\right)\Delta E = [J]^T \left\{\overline{F}_{calc} - \overline{F}_{exptl}\right\}$$

where $\Delta E$ is the change in material property for the iterative method, i.e.

$$E_{i+1} = E_i + \Delta E ,$$

and $\alpha$ is a regularization term to improve the conditioning of the iterative procedure and is defined as,

$$\alpha = \left(\lambda * \text{trace}\left([J]^T [J]\right) * SSE^2\right)^{1/2} \quad [64]$$

where λ is an empirical factor, and SSE is the sum squared error between measured and calculated force. It should be noted that the Jacobian was determined by a finite difference calculation which was initiated by a 2.5% perturbation from the initial guess of the callus property. As schematically presented in Figure 1, the process is repeated until the relative error between iterations converges below a set tolerance or until no improvement in objective function is noted.

Material type description based on microCT/histological thresholding analysis

To determine material type from microCT scans, a parametric thresholding study was performed by serial microCT scanning and histological analysis. Fractured tibia calluses were dissected, fixation pins removed, and microCT scanned at 6 μm voxel resolution. Bones were then fixed for 48 h at 4 °C in 4% paraformaldehyde solution, and decalcified for 10 days in an EDTA decalcification solution (10 mM Tris-HCl, 10% EDTA, 7.5% polyvinylpirrolidone pH 7.5). Bones were dehydrated in a graded ethanol series, embedded in paraffin, and sectioned at 6 μm thickness along ~5.2 mm length centered at the fracture line. This resulted in 864 histological sections per bone, which were placed 3 sections per slide and divided into 4 serial groups for staining, resulting in ~72 slides per group (72 slides x 3 sections/slide x 4 groups). *In-situ* hybridizations for Collagen 1 and Collagen 10 and Trichrome Blue and Safranin O/Fast Green histological staining were performed to identify tissue type. Trichrome Blue and Safranin O/Fast Green staining were obtained using standard histological procedures as previously described [71]. Collagen 1 *in situ* hybridization was used to label new bone, Collagen 10 *in situ* hybridization to label hypertrophic chondrocytes; Safranin O/Fast

Green staining to label areas of cartilaginous tissue as bright red and areas of bone as green; Trichrome Blue staining to label newly mineralized bone as blue and highly mineralized bone as red. *In situ* hybridization analysis was performed as previously reported [72]. Plasmid with insertion of mouse Collagen (I)-alpha-1-chain (Col1a1) by G. Karsenty (Columbia University). Probe for mouse Collagen (X)alpha1chain (Col10a1) was generated as previously described [72]. Each histological marker was quantified by a custom built image analysis code written in MATLAB (Mathworks Inc., Natick, MA) that was used to select tissue type (cartilage tissue, new bone, and cortical bone) based on color intensity. Groups were quantified by summation of voxels and multiplied by voxel volume to yield volume of tissue. The microCT image stack was then thresholded based on radiodensity into the 3 groups that visually and quantitatively matched histological staining determination of tissue type. The soft tissue and new bone regions were lumped together and defined as callus material and the cortical bone regions were taken to be cortical bone material.

Description of analysis metrics

*BMT metrics:*

Ultimate load is defined as the peak force recorded during the BMT procedure. Toughness is defined as the area under the Force vs. displacement curve from the origin to the point of ultimate load. Apparent stiffness is defined as the slope of a best fit line to the linear portion of the force versus displacement curve during the loading phase. Normalized apparent stiffness is defined as apparent stiffness with

the force and displacement values normalized by dividing by the largest cross-sectional area of the callus and its overall length, respectively.

*Imaging metrics:*

Total bone volume was determined by summing the voxels corresponding to mineralized tissue (new bone and cortical bone), then multiplying by the voxel resolution. Total callus volume was determined by summing the voxels corresponding to callus tissue (soft tissue and new bone), then multiplying by the voxel resolution.

Appendix II: Derivation of simulation force

$$\sigma = E\varepsilon \tag{1}$$

$$\frac{P}{A} = E\frac{\delta}{L} \tag{2}$$

$$\delta = \frac{PL}{EA} \tag{3}$$

$$\delta = \delta_1 + \delta_2 + \delta_3 \tag{4}$$

$$P = P_1 = P_2 = P_3 \tag{5}$$

$$\delta = \frac{P_1 L_1}{E_1 A_1} + \frac{P_2 L_2}{E_2 A_2} + \frac{P_3 L_3}{E_3 A_3} \tag{6}$$

Because $L=L_1=L_2=L_3$, $A=A_1=A_2=A_3$ and from (5),

$$\delta = \frac{PL}{A}\left(\frac{1}{E_1} + \frac{1}{E_2} + \frac{1}{E_3}\right) \tag{7}$$

Since E1=E3,

$$P = \frac{\delta A}{L}\left(\frac{E_1 E_2}{2E_2 + E_1}\right) \tag{8}$$

# CHAPTER IV

# COMPARISON OF MICROCT AND A NOVEL INVERSE FINITE ELEMENT ANALYSIS: RESULTS IN A MSC THERAPEUTIC SYSTEM

## Introduction and Contribution of Study

The work presented within this chapter is an extension of the initial inverse FEA study and the mesenchymal stem cell study contained within Chapter 3 and Appendix A, respectively. In this chapter, bone fracture calluses at both 14 and 21 days post-fracture are compared from mice either receiving or not receiving a therapeutic transplantation of mesenchymal stem cells. As shown in Appendix A, mesenchymal stem cells are capable of migrating to the fracture site, engrafting, and becoming involved with the reparative process through differentiation into chondrocytes and osteocytes. This initial fracture healing with mesenchymal stem cell transplantation study provided the initial evidence that fractures in mice treated with MSC transplantation were better in both mechanical competence and bone tissue volume than fractures in mice that received no treatment. However as shown in Chapter 3, the inverse FE assessment procedure provides a greater degree of sensitivity and ability to assess the mechanical properties of the healing callus tissue. Therefore the inverse FE assessment methodology was applied to assess fractures from mice receiving MSC transplantation and compared to mice without MSC transplantation. This study thus serves as an additional challenge to the assessment methodology towards determining fracture callus mechanical property differences in a therapeutic system as well as a more functional and sensitive measurement applied

towards the effect of MSC transplantation upon mechanical properties. Additionally, this study challenges the assertion that microCT imaging-derived measurements can be used as a surrogate for functional mechanical analysis. Through the use of multiple data points at different stages of healing with and without a therapeutic interventional system, analysis metrics from imaging, biomechanical testing, and inverse FE analysis can be compared for their respective ability to differentiate experimental groups. This work is a manuscript that has been submitted and is currently under peer-review.

Appearing in:

Jared A. Weis, Froilan Granero-Molto, Timothy J. Myers, Lara Longobardi, Anna Spagnoli and Michael I. Miga. Comparison of microCT and a novel inverse finite element analysis: Results in a MSC therapeutic system. Submitted manuscript, under review.


## Abstract

An important concern in the study of fracture healing is the ability to assess mechanical integrity in response to candidate therapeutics in small-animal systems. In recent reports, it has been proposed that microCT image-derived densitometric parameters could be used as a surrogate for mechanical property assessment. Recently, we have proposed an inverse methodology that iteratively reconstructs the modulus of elasticity of the lumped soft callus/hard callus region by integrating both intrinsic mechanical property (from biomechanical testing) and geometrical information (from microCT) within an inverse finite element analysis (FEA) to define a callus quality

measure. In this paper, data from a therapeutic system involving mesenchymal stem cells is analyzed within the context of comparing traditional microCT densitometric and mechanical property metrics. In addition, a novel multi-parameter regression microCT parameter is analyzed as well as our inverse FEA metric. The results demonstrate that the inverse FEA approach was the only metric to successfully detect both longitudinal and therapeutic responses. While the most promising microCT-based metrics were adequate at early healing states, they failed to track late-stage mechanical integrity. In addition, our analysis added insight to the role of MSCs by demonstrating accelerated healing and was the only metric to demonstrate therapeutic benefits at late-stage healing. In conclusion, the work presented here indicates that microCT densitometric parameters are an incomplete surrogate for mechanical integrity. Additionally, our inverse FEA approach is shown to be very sensitive and may provide a first-step towards normalizing the often challenging process of assessing mechanical integrity of healing fractures.

## Introduction

Long bone fracture healing proceeds through the formation of a cartilaginous callus template that is progressively mineralized and replaced by bone which then undergoes remodeling [2]. There are approximately 7.9 million bone fractures that occur annually in the United States alone, with an approximate cost of $70 billion [73]. However, 10-20 % of these fractures exhibit impaired healing, delayed union, or non-union [5]. Current methods of treatment include autograft, allograft, and pharmacological therapies. These treatment methods experience varying degrees of

success but have significant drawbacks, including donor site morbidity, graft osteoinduction, limited efficacy, and significant morbidity and mortality [74-80].

Recently, significant interest has been directed at mesenchymal stem cell (MSC) transplantation as a potential therapeutic treatment in bone fracture for both their autocrine and paracrine effects. Previous research has shown that MSC, infused systemically or implanted locally, migrate and home into damaged tissues including fractured bones to improve healing [1, 21-25, 81, 82]. In particular, MSC have been shown to engraft at the fracture site and differentiate into mature mesenchymal cell types [1]. MSC transplantation has been also shown to increase some biomechanical properties (toughness and ultimate displacement increase with no change in apparent stiffness and ultimate force) and microCT derived volumetric and mineralization parameters (total volume, bone volume, bone mineral content) [1].

However, considerable uncertainty remains regarding true quantitative assessment of bone fracture healing. As the primary goal of fracture healing treatment is a return to load bearing function, mechanical integrity of the healing fracture callus is arguably the most important metric. Thus biomechanical testing (BMT) remains the gold standard for functional fracture healing assessment. However, biomechanical testing of fracture callus does not come without its own challenges. Classical biomechanical analysis techniques use extrinsic force versus displacement data obtained from mechanical testing of homogeneous machined samples and analytic calculations based on specimen geometry to generate intrinsic material property information, such as tissue elastic modulus. However, due to the atypical and inhomogeneous nature of the fracture callus, such machining and homogenization is improper. Therefore, mechanical testing and

theoretical calculations must be performed on the irregular and inhomogeneous specimen, for which a true closed-form solution does not exist. This process yields whole-bone extrinsic material property metrics, such as apparent stiffness. To determine tissue-level intrinsic material property information, analytic calculations rely on the assumption of a homogeneous and regular cross section. But because of the irregular geometry of the bone and callus, these calculations have been shown to be strongly biased by geometrical factors [44] and are unable to generate accurate tissue-level intrinsic material properties. Thus, the current gold standard approach of determining extrinsic material properties as a biomechanical metric for fracture healing is clearly lacking.

Recent studies have suggested the use of microCT as not only a quantitative volumetric analysis method, but as a surrogate measure of mechanical function through correlation/multi-regression of microCT analysis parameters (tissue mineral density – TMD, standard deviation of TMD – σTMD, bone volume – BV, total volume – TV, BV/TV ratio, and bone mineral content – BMC) [35, 36]. A recent study utilizing these methods was able to explain 62% of the variability in maximum torque (using TMD, BV, and σTMD) and 70% of the variability in torsional rigidity (using TMD, BMC, BV/TV, and σTMD) with only microCT parameters used in stepwise multiple regression analyses [35]. However, this explanation is purely correlative in nature and does not directly address functionality of the healing callus tissue. These microCT metrics, including those used in microCT-to-BMT regression studies, by design only provide quantification of volume and/or mineral density and therefore do not reflect the 3-dimensional mechanical connectivity of bone tissue within the callus. Similar to dual-energy X-ray

absorptiometry (DXA) measured bone density (a bone quantity measure which has been disputed as an accurate measure of bone quality [37-43]), these commonly used microCT measures quantify bone quantity/density within the callus but ignore changes in the geometry and spatial organization of the callus tissue and thus do not accurately reflect callus mechanical quality, which is the major determinant of mechanical function. As bone fracture healing progresses, there is both a gradual accumulation of bone mineral as well as a gradual spatial arrangement of that mineral towards enhanced mechanical function/stability. While the total volume and amount/density of mineral somewhat correlate with early stage healing progression, these are not the proper biomarkers to monitor as a determinant of fracture healing as they do not directly correspond to callus quality or mechanical function. While an imaging marker surrogate for mechanical function is highly desirable, our hypothesis is that only through the direct analysis of force and displacement data can mechanical integrity be assessed. Currently, the gold standard in biomechanical testing methodologies do not account for the confounding geometrical effects associated with the callus shape and constituency. Unfortunately, as a result, arguably one of the most important criteria, mechanical stability, is the least resolved with respect to fracture healing assessment.

Finite element analysis (FEA), a numerical simulation method in which an object is broken down into discreet sub-regions and mechanically simulated, has recently emerged as a method to analyze mechanical function and assess callus quality in fracture healing [46, 61]. We have previously shown the capability of inverse finite element analysis to detect changes in the elastic modulus of early stage normal bone fracture calluses in mice [61]. Utilizing this inverse problem methodology, accurate predictions

of intrinsic callus quality measures (e.g. elastic modulus) of the bone fracture callus tissue can be determined through the integration of biomechanical testing data and microCT derived data.

Within this study, we analyzed bone fracture callus tissue in mice either receiving or not receiving MSC transplantation through biomechanical analysis, microCT based analysis, and a novel inverse FEA modulus reconstruction procedure. The objectives of this study were to: 1) monitor the longitudinal functional changes in callus tissue among experimental therapeutic groups, 2) evaluate the sufficiency of microCT-derived measures and multi-regression as a surrogate for biomechanical analysis, and 3) evaluate the discriminatory capability of analysis methods (biomechanical testing, microCT, and inverse FEA modulus reconstruction) in clearly highlighting differences between experimental groupings.

## Methods

### Murine system

In previous work a murine tibia fracture system was developed to longitudinally assess the behavior of bone fracture calluses with respect to mesenchymal stem cell (MSC) transplantation [1]. Briefly, this animal model involves 8-12 week old female FVB-NJ mice (Jackson Laboratories) subjected to pin-stabilized tibial fracture utilizing a three-point bending impact device. At prescribed time points post-fracture (14 and 21 days), mice were euthanized and fractured tibias were prepared for analysis. Mice at each time point were divided into groups either receiving or not receiving therapeutic

transplantation of $1x10^6$ MSC via tail vein injection. Further details of the MSC transplantation system can be found in [1]. MicroCT imaging data was collected using the acquisition parameters of 55 kVP, 145 uA, 300 ms integration time, and 12 um voxel resolution [1, 61]. Biomechanical testing and mechanical analysis were performed as previously described [1, 61]. Briefly, fracture calluses were loaded in tension while force and displacement were recorded until failure; biomechanical metrics of healing (peak force, stiffness, and toughness) were calculated as previously described in [61].

Inverse finite element analysis

Subject-specific FE models were generated by semi-automatic image segmentation and boundary surface extraction from microCT image data as previously described [61]. The image segmentation and boundary surface extraction was performed for the callus tissue/air boundary as well as the cortical bone/callus tissue boundary, and the boundary description was used to create a tetrahedral FE mesh using custom-built mesh generation methods [62].

An inverse FEA procedure (as created in previous work [61]) was utilized to iteratively reconstruct the Young's modulus for callus material within the FE model. Briefly, the process begins with the creation of a subject specific Hookean linear elastic tissue computer FE model of the bone/callus specimen generated from segmented microCT images. An initial guess of the callus Young's modulus is assigned and boundary conditions corresponding to the individualized force/displacement curves generated from each specimen during the experimental biomechanical testing protocol are then applied. A series of 10 displacements are taken equally spaced along the curve

up to the linear elastic limit, serving as simulated displacements. From these simulations, the applied mechanical force can be estimated and compared to the empirical counterpart within a Levenberg-Marquardt non-linear optimization framework until a best fit is found [61]. Details of the approach can be found in [30].

MicroCT imaging analysis methods

A primary goal of this study is to directly evaluate the sufficiency of microCT as a surrogate for mechanical integrity as compared to our novel inverse FEA approach within the context of an intuitive therapeutic MSC transplantation system. As a part of the study, the following standard microCT derived metrics were determined using the callus image volume: total volume (TV) – defined as the volume of all voxels within the callus; bone volume (BV) – defined as the volume of voxels identified as bone by thresholding; callus mineralized volume fraction (BV/TV); tissue mineral density (TMD) – defined as the average voxel density (in g HA/$m^3$) of voxels within the BV component of the callus, standard deviation of mineral density ($\sigma_{TMD}$) – defined as the standard deviation of voxel density (in g HA/$m^3$) of voxels within the BV component of the callus; and bone mineral content (BMC) – defined as BV multiplied by TMD. A fixed global threshold of 25% of the maximum intensity value was selected to differentiate mineralized callus from non-mineralized callus. Soft tissue volume and callus volume were also calculated as described in [61].

Additionally, a regression similar to the one proposed by Morgan et al. [35] was calculated retrospectively whereby a microCT-based multiple regression was used to predict mechanical properties from microCT measures. Briefly, the Statistics Toolbox in

MATLAB was used to perform a multiple linear regression with TMD, BMC, BV/TV, and σTMD as predictors and stiffness as the response observation. Utilizing this methodology we obtain a metric representing mechanical stiffness that is derived purely from microCT data. This measure is equivalent in design to many other microCT-to-BMT statistical models/correlations proposed in the literature [35].

Comparisons across and among analysis metrics

Four unique data sets exist within the experimental mouse system data provided (two treatment cohorts - therapeutic and non-therapeutic, and at two different healing states - 14 days and 21 days) which leads to six unique comparisons among the groups. Comparisons by the proposed metrics should have some intuitive outcomes with respect to changes that are purely longitudinal in nature as well as supported outcomes from therapeutic findings based on the work in [1]. With respect to longitudinal assessments, we should observe increased mechanical integrity within appropriate treatment cohorts across time points. Based on [1], we would expect to observe increased mechanical integrity across treatment groups at similar time points. Comparing untreated early-stage to late-stage treated subjects should demonstrate both longitudinal and therapeutic benefits. Lastly, comparing untreated late-stage to early-stage treated subjects should indicate equivalence based on [1] inferring that the early-stage treated subjects experienced improved healing due to the administration of MSC therapy. Groups selected for statistical significance comparisons on each analysis metric are summarized along with their respective hypotheses in Table 5. Briefly, comparisons highlighted in green represent ones in which analysis metrics should show improvement in the fracture

healing process based on a greater amount of time or therapeutic application, whereas the comparison highlighted in yellow represents one in which analysis metrics should show equivalence due to acceleration of the fracture healing process as suggested by [1].

One-way analysis of variance (ANOVA) was used to determine statistically significant metrics and unpaired Student's *t*-test was used pair-wise across and among longitudinal and therapeutic groups as a post test. Data are expressed as mean ± SD and statistical significance was set at $p<0.05$. Analysis metrics shown to be statistically significant by ANOVA were subjected to pair-wise correlation analysis. Correlation coefficients were calculated by Pearson product-moment correlation coefficient analysis.

Table 5. Group comparisons used for each analysis metric and their respective hypotheses with respect to the MSC therapeutic system. Comparisons highlighted in green represent ones in which analysis metrics should show improvement in fracture healing. The comparison highlighted in yellow represents one in which analysis metrics should show equivalence. Comparisons listed in bold reflect greater importance.

| Comparison | Hypothesis |
|---|---|
| **14d NC v 21d NC** | **Longitudinal improvement** |
| **14d MSC v 21d MSC** | **Longitudinal improvement** |
| **14d NC v 14d MSC** | **Therapeutic improvement** |
| **21d NC v 21d MSC** | **Therapeutic improvement** |
| 14d NC v 21d MSC | Combined longitudinal and therapeutic improvement |
| 14d MSC v 21d NC | Equivalent due to therapeutic improvement |

## Results

### MSC effects on callus microCT metrics

Representative microCT image volumes from control non-recipient mice (NC) and MSC recipient mice (MSC) for both 14 and 21 days post-fracture are shown in

Figure 20 and volumetric quantifications are reported in Table 8 and visually presented in Figure 21. Statistical comparisons and associated p values are reported as compiled with all other metrics in Table 8. These data show that the degree of tissue mineralization is enhanced longitudinally in both NC and MSC groups and that MSC enhances this mineralization level at 14 days post-fracture but not at 21 days post-fracture. Qualitatively demonstrated in the volumetric reconstructions and X-ray images in Figure 20, more mineralization as well as a greater degree of bridging bone is seen in the fracture callus both longitudinally and with MSC transplantation.

Table 6. MicroCT metrics. [*], $p< 0.05$ by ANOVA. Post-test pair-wise statistical comparisons are shown only for comparisons listed in bold from Table 5. [a], $p< 0.05$ vs. 14d NC. [b], $p< 0.05$ vs. 14d MSC. [c], $p< 0.05$ vs. 21d NC.

| | **TV ($mm^3$)** | **BV ($mm^3$)** | **BV/TV** | **TMD (mg HA/cc)** | **$\sigma_{TMD}$ (mg HA/cc)** | **microCT Regress. (N/mm)** | **Soft Volume ($mm^3$)** | **Callus Volume ($mm^3$)** |
|---|---|---|---|---|---|---|---|---|
| **14d NC** | 11.37 ± 3.95 | 4.76 ± 1.75 | 0.42 ± 0.07 | 1.20E-6 ± 4.47 E-8 | 6.22E-8 ± 2.80 E-8 | 14.38 ± 8.45 | 6.09 ± 2.69 | 8.83 ± 3.03 |
| **14d MSC** | 11.19 ± 4.22 | 5.19 ± 1.71 | 0.47 ± 0.05 | 1.28E-6 ± 2.33 E-8[a] | 8.52E-8 ± 3.78 E-8 | 20.89 ± 6.68 | 5.19 ± 1.8 | 8.53 ± 2.81 |
| **21d NC** | 11.29 ± 7.10 | 6.35 ± 2.52 | 0.61 ± 0.12[a] | 1.42E-6 ± 1.12 E-7[a] | 1.04E-7 ± 4.69 E-8 | 37.72 ± 5.35[a] | 4.40 ± 3.34 | 9.00 ± 4.34 |
| **21d MSC** | 9.95 ± 3.27 | 6.14 ± 2.03 | 0.62 ± 0.01[b] | 1.42E-6 ± 5.45 E-8[b] | 6.32E-8 ± 2.80 E-8 | 40.63 ± 8.11[b] | 3.81 ± 1.58 | 9.02 ± 2.67 |
| **P Value (ANOVA)** | 0.9744 | 0.6136 | 0.0044[*] | 0.0004[*] | 0.3455 | 0.0007[*] | 0.5818 | 0.9964 |


Figure 20. Representative (left) volumetric microCT reconstructions and (right) simulated X-ray images of (A,B) 14d NC, (C,D) 14d MSC, (E,F) 21d NC, (G,H) 21d MSC.

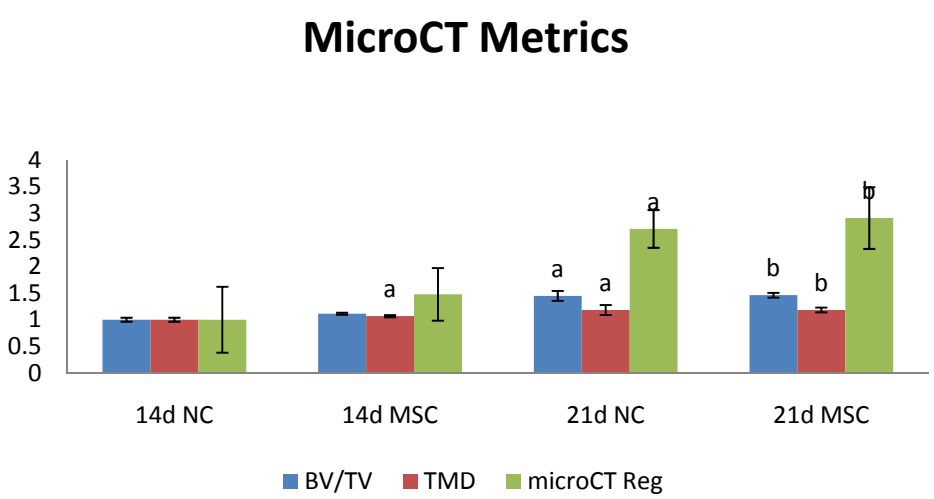


Figure 21. MicroCT based metrics. Data are normalized with respect to 14d NC. Post-test pair-wise statistical comparisons are shown only for comparisons listed in bold from Table 5. [a], $p< 0.05$ vs. 14d NC. [b], $p< 0.05$ vs. 14d MSC. [c], $p< 0.05$ vs. 21d NC.

MSC effects on callus BMT metrics

Biomechanical testing (force vs. displacement) data from NC and MSC at 14 and 21 days post-fracture is shown in Figure 22. A wide variation in the curves is observed both among and across all testing groups representing a broad distribution of extrinsic biomechanical properties. Quantitative analysis of biomechanical testing metrics of ultimate load, toughness, and apparent stiffness were generated for these samples and the results are shown in Table 7 and Figure 23. Statistical comparisons and associated p values are reported as compiled with all other metrics in Table 8. Reflecting the wide variation among biomechanical testing data, a statistically significant increase was observed for apparent stiffness only for wild-type mice from early to late-stage healing. These data show that extrinsic whole-bone BMT measures are enhanced longitudinally from 14 to 21 days post-fracture and that MSC transplantation enhances only some of

these extrinsic properties at 14 days post-fracture but not at 21 days post-fracture. However, without accounting for the geometrical changes caused by time and MSC treatment on calluses, it is impossible to separate the enhancement in whole bone BMT behavior from either geometrical morphological changes or tissue-level mechanical improvement.

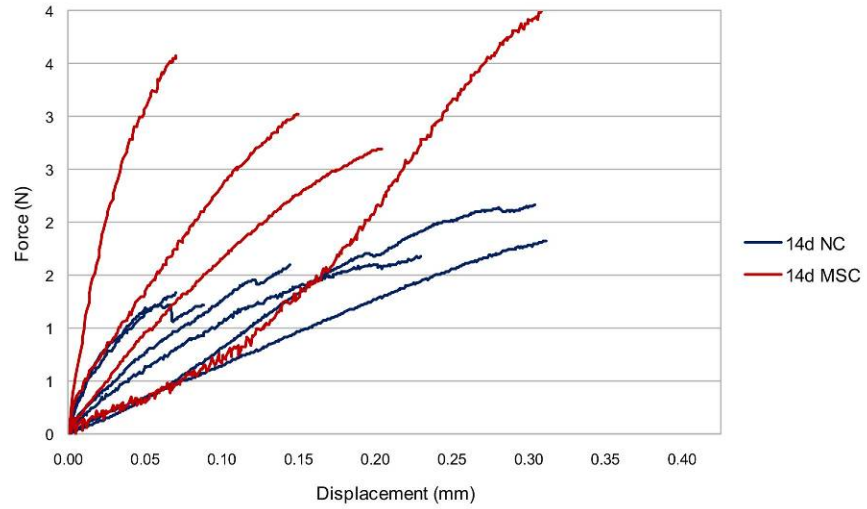


A

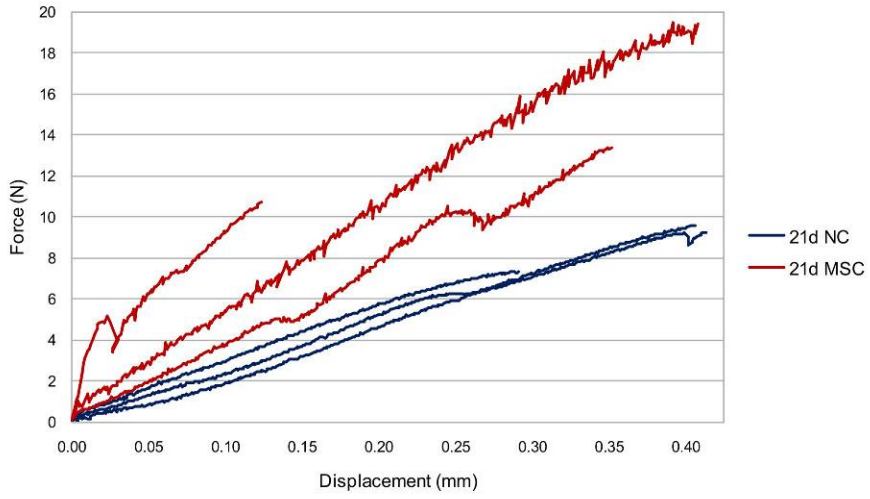


B

Figure 22. BMT force vs. displacement plot for (A) 14d NC and 14d MSC, (B) 21d NC and 21d MSC.

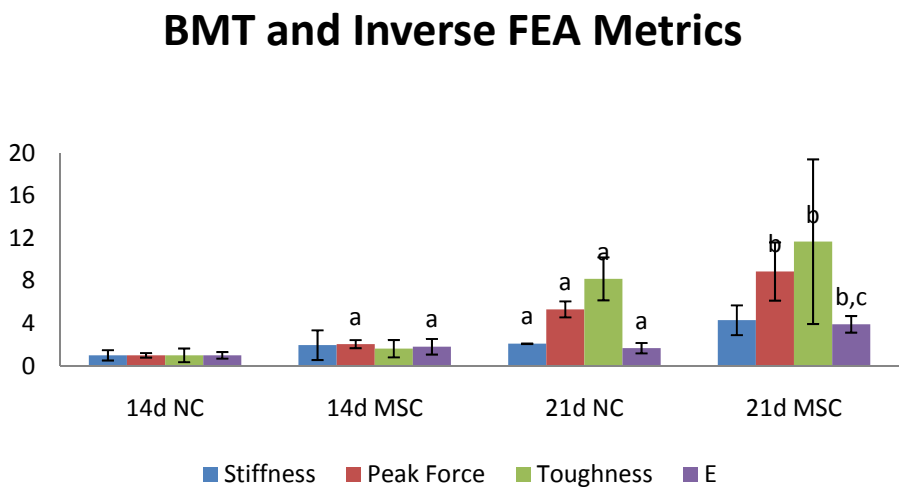


Figure 23. BMT and inverse FEA metrics. Data are normalized with respect to 14d NC. Post-test pair-wise statistical comparisons are shown only for comparisons listed in bold from Table 5. [a], $p < 0.05$ vs. 14d NC. [b], $p < 0.05$ vs. 14d MSC. [c], $p < 0.05$ vs. 21d NC.

Table 7. Biomechanical testing and inverse FEA reconstructed modulus metrics. [*], $p < 0.05$ by ANOVA. Post-test pair-wise statistical comparisons are shown only for comparisons listed in bold from Table 5. [a], $p < 0.05$ vs. 14d NC. [b], $p < 0.05$ vs. 14d MSC. [c], $p < 0.05$ vs. 21d NC.

| | **Stiffness (N/mm)** | **Toughness (N*mm)** | **Peak Force (N)** | **Inverse FEA Modulus (kPa)** |
|---|---|---|---|---|
| **14d NC** | 12.23 ± 5.90 | 0.2 ± 0.13 | 1.63 ± 0.35 | 2296.45 ± 715.56 |
| **14d MSC** | 23.89 ± 17.05 | 0.33 ± 0.17 | 3.35 ± 0.61[a] | 4144.09 ± 1686.89[a] |
| **21d NC** | 25.55 ± 0.35[a] | 1.66 ± 0.41[a] | 8.68 ± 1.23[a] | 3842.02 ± 1123.96[a] |
| **21d MSC** | 52.51 ± 17.06 | 2.37 ± 1.57[b] | 14.49 ± 4.46[b] | 8981.57 ± 1798.59[b,c] |
| **P Value (ANOVA)** | 0.0034[*] | 0.0020[*] | 3.8E-6[*] | 9.66E-5[*] |

MSC effects on callus inverse FEA reconstructed modulus

Finite element models were created as described and representative FE meshes from MSC and NC at 14 and 21 days post-fracture are shown in Figure 24. Inverse FEA generated material property reconstructions were performed as described to generate estimations for the Young's modulus of the callus material. As shown in Table 7 and Figure 23, significant increases were observed for the inverse FEA modulus reconstructions for all important comparison groups longitudinally for both NC and MSC. Additionally, significant increases were observed for the inverse FEA modulus reconstructions in the case of MSC transplantation at both 14 days and 21 days post-fracture, representing an enhancement in the modulus of elasticity in calluses treated with MSC at both early and late-stage healing. Notably, a greater than 2 fold increase in inverse FEA reconstructed elastic modulus was observed at 21 days post-fracture for MSC transplantation as compared to control, which was the only metric analyzed that provided statistical significance at this time point. Statistical comparisons and associated p values are reported as compiled with all other metrics in Table 8.

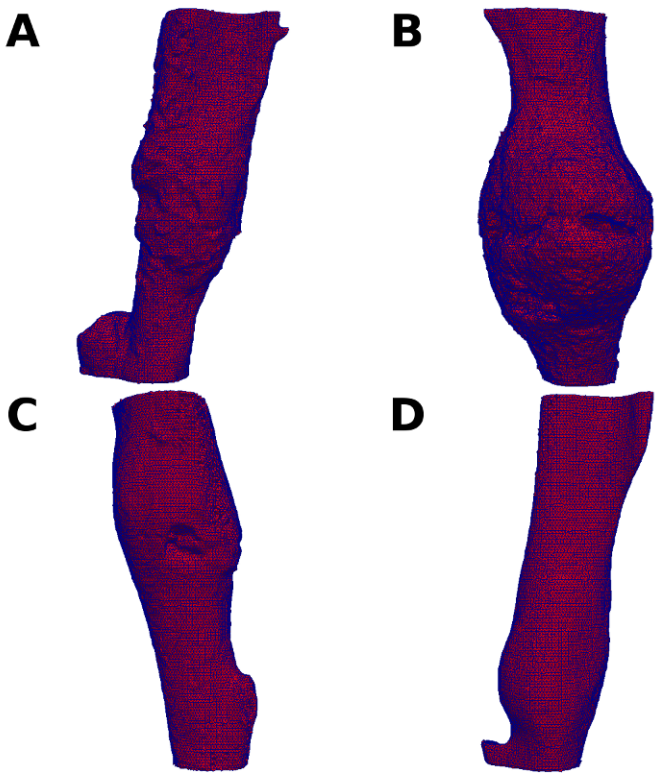

Figure 24. FEA Meshes for (A) 14d NC, (B) 14d MSC, (C) 21d NC, and (D) 21d MSC.

Comparisons and correlations among analysis metrics

Table 8 illustrates the compilation of the analysis metrics from this work. Comparison metric names are displayed in the upper triangular region of the matrix with respective quantitative p values associated with the pair-wise *t*-tests shown in the symmetric position in the matrix. The table is also color-coded with green designating a statically significant difference and yellow designating no statistically significant difference. While the table yields considerable information, we draw attention to 3 interesting aspects. Outlined in magenta we see a clear comparison where a traditional biomechanical and microCT metric as well as the microCT-based stiffness regression fail to discriminate (stiffness and BV/TV), whereas the inverse FEA reconstructed modulus and other traditional BMT and microCT metrics (peak force and TMD) show a statistically significant difference. Outlined in black, we see an interesting finding whereby the MSC treated 14 day post-fracture data is similar in tissue mineral density and mechanical properties to that of the untreated 21 day post-fracture. Lastly, circled in red, the comparison between 21 day post-fracture with and without MSC transplantation shows that our novel metric is the only one to identify a statistical difference.

Correlation analysis was performed pair-wise for each statistically significant metric and the correlation matrix is shown in Table 9. Moderate positive correlations between BMT and microCT were observed ranging from $r = 0.62$ to $r = 0.74$; however microCT metrics correlated weakest with the apparent stiffness parameter. Additionally, the inverse FEA estimated elastic modulus parameter was seen to correlate very strongly ($r = 0.91$) with apparent stiffness and moderately with microCT derived measures and ultimate load.

Table 8. Significance matrix comparing BMT, microCT, and inverse FEA material property reconstruction analysis metrics. "E" represents the inverse FEA reconstructed modulus, "Stiffness" represents the slope of the force vs. displacement curve, "Peak Force", represents the peak biomechanical force experienced during testing, "BV/TV" represents bone volume to total volume fraction, "µCT-Reg" represents the microCT-based stiffness multiple regression, and "TMD" represents tissue mineral density. Green denotes significant differences ($p<0.05$), while yellow represents no significant differences. The upper triangular region designates metrics while the associated p-values are found in the lower triangular region. Comparisons of interest are outlined in magenta, black, and red.

| Cohort | 14 Day No Cells n=6 | | | 14 Day MSC n=4 | | | 21 Day No Cells n=3 | | | 21 Day MSC n=3 | | |
|---|---|---|---|---|---|---|---|---|---|---|---|---|
| 14 Day No Cells n=6 | | | | E<br>BV/TV | Stiffness<br>µCT-Reg | Peak Force<br>TMD | E<br>BV/TV | Stiffness<br>µCT-Reg | Peak Force<br>TMD | E<br>BV/TV | Stiffness<br>µCT-Reg | Peak Force<br>TMD |
| 14 Day MSC n=4 | 0.041<br>0.287 | 0.1526<br>0.2336 | 5.00E-04<br>0.012 | | | | E<br>BV/TV | Stiffness<br>µCT-Reg | Peak Force<br>TMD | E<br>BV/TV | Stiffness<br>µCT-Reg | Peak Force<br>TMD |
| 21 Day No Cells n=3 | 0.037<br>0.019 | 0.0069<br>0.0036 | 2.40E-06<br>0.003 | 0.8<br>0.083 | 0.8761<br>0.0161 | 6.00E-04<br>0.052 | | | | E<br>BV/TV | Stiffness<br>µCT-Reg | Peak Force<br>TMD |
| 21 Day MSC n=3 | 1.00E-04<br>0.003 | 9.00E-04<br>0.003 | 1.00E-04<br>4.00E-04 | 0.015<br>0.005 | 0.0794<br>0.0164 | 0.004<br>0.006 | 0.0137<br>0.944 | 0.0521<br>0.6317 | 0.096<br>0.924 | | | |

Table 9. Pearson product-moment correlation coefficient matrix for all metrics classified as significant by ANOVA ($p< 0.05$).

| | E | Stiffness | Toughness | Peak F | BV/TV | TMD | µCT-Reg |
|---|---|---|---|---|---|---|---|
| E | | 0.91 | 0.48 | 0.70 | 0.56 | 0.53 | 0.70 |
| Stiffness | 0.91 | | 0.48 | 0.69 | 0.62 | 0.57 | 0.75 |
| Toughness | 0.48 | 0.48 | | 0.95 | 0.68 | 0.67 | 0.59 |
| Peak F | 0.70 | 0.69 | 0.95 | | 0.74 | 0.74 | 0.73 |
| BV/TV | 0.56 | 0.62 | 0.68 | 0.74 | | 0.86 | 0.83 |
| TMD | 0.53 | 0.57 | 0.67 | 0.74 | 0.86 | | 0.76 |
| µCT-Reg | 0.70 | 0.75 | 0.59 | 0.73 | 0.83 | 0.76 | |

## Discussion

This study compared an inverse FEA elastic modulus reconstruction algorithm with both BMT and microCT derived metrics within the context of longitudinal changes in bone fracture healing and with therapeutic transplantation of MSC. Based on ANOVA, four of the six common microCT metrics demonstrated significance – bone

volume-to-total volume ratio, tissue mineral density, standard deviation of tissue mineral density, and the microCT multi-parameter regression metric. With respect to mechanical property metrics, all showed significance in monitoring changes within this experimental system – stiffness, toughness, peak force, and our novel inverse FEA modulus metric. One interesting finding is circled in black on Table 4 whereby early-stage treated mice demonstrated an equivalent mechanical property to their late-stage untreated counterparts. This suggests an accelerated rate of healing in response to MSC transplantation. It is also interesting to note in this comparison that the multi-parameter regression metric assigned a statistically significant difference to this comparison, which in this case represents a failure as it is unsupported by the microCT, BMT, and inverse FEA modulus data. Interestingly, the more simplistic microCT metrics of TMD and BV/TV produced a similar result to that of inverse elasticity analysis. This conflict among microCT metrics speaks to its fidelity. Another interesting finding is the red circled region of Table 4. This comparison between 21 day post-fracture with and without MSC transplantation indicates that our novel metric was the only one to register a statistical difference. More specifically, all microCT metrics failed this test including TMD, which was the most successful microCT metric in this study. This result is troublesome with respect to considering microCT as a surrogate for mechanical function. Observing Figure 22b, a clear difference between these groups is supported. This indicates that while TMD could be a successful surrogate at early stage healing, its role throughout the continuum of healing is inadequate in these experiments. In light of this, if we revisit the black circled finding, the weak rejection of the hypothesis by TMD versus the stronger rejection by our parameter may be a confirmation that bone mineral

density is challenged in capturing biomechanical effects at progressively late stages. If comparing the force vs. displacement curves associated with the 14 day MSC treatment (Figure 22a) and the 21 day no cells system (Figure 22b), the distribution of the curves of the former would completely envelope the more closely distributed curves of the latter and as such supports these two groups as being mechanical similar. Of equal weight to the red circled finding, this observation was missed by the multi-parameter regression metric and only weakly rejected with TMD while soundly rejected by our inverse metric. As we step back from this study, the inverse metric consistently passed all tests while the microCT metrics were of inconsistent veracity and at times failed. These data highlight the power of this analysis and the tenuous nature of microCT as a surrogate.

As reported, our results demonstrate that the inverse FEA reconstructed elastic modulus is a more sensitive measure of callus quality than BMT or microCT derived measures (including microCT-to-BMT regression based metrics) alone. Throughout the range of comparisons, both traditional BMT and microCT derived measures were inconsistent across the intuitive comparisons conducted. As a result of this work, the suggestion that microCT measures be accepted as a surrogate for true mechanical functional analysis must be called into question. Furthermore, the mechanistic basis of the relationship between elastic modulus derived via inverse FEA reconstructions and callus quality is quite clear from classical mechanics, whereas the relationship between microCT derived parameters is not. With the failure of densitometric parameters, it would seem to suggest that the spatial arrangement/architecture is changing outside of additive material property benefits. Furthermore, monitoring these proposed surrogate metrics seems inappropriate whereas the metric we have proposed is a measure that

accounts for both the amount and arrangement of material and is directly relatable to classical mechanics. In addition, it is important to note that the microCT metrics analyzed reflect those of previous work [35] and the murine system analyzed produced comparable correlations in basic densitometric measures (Table 8, $r = 0.57$, stiffness vs. TMD) as well as the more novel multi-parameter regression measures (Table 8, $r = 0.75$, stiffness vs. μCT-reg).

From our inverse FEA reconstruction data, we reach the supported conclusion that the elastic modulus of bone fracture callus tissue is gradually enhanced over time during early to late-stage fracture healing. Systemic transplantation of MSC accelerates the increase in callus elastic modulus. Over time, we expect this enhancement provided by MSC as compared to normal to gradually reduce as healing transitions into later stages, but further studies on late stage healing are needed to determine the exact timeline of MSC enhancement in callus tissue mechanical properties. Previous research has shown that MSC engraft at the fracture site and express bone morphogenic protein 2 (BMP-2) [1] and as such is a potent and essential initiator of the fracture healing cascade [7]. Our results regarding the effects of MSC transplantation corroborate previous work [1], in that transplantation of MSC is seen to enhance fracture healing even in a normal fracture healing animal model, however it is important to note that this work advances the understanding of the biomechanical effects of MSC transplantation on healing callus tissue by demonstrating the increase in modulus in response to therapy.

Lastly, it should be noted that there are several drawbacks to our current approach. Our methodology is currently unable to be directly translated to *in vivo* fracture healing assessment due to the direct biomechanical testing needed to provide

mechanical information to the inverse FEA procedure. However, our procedure provides valuable callus quality information necessary for assessment of experimental fracture healing due to therapeutic or genetic manipulations. Also, the material simplification through the use of an assumed linear elastic constitutive law yields an inherently limited material model. But it should be noted that the goal of this study was to generate material property information based on an assumed material model that was capable of accurately discriminating longitudinal and therapeutic groupings, not to generate the most accurate multi-physics model of a bone fracture callus system.

## Conclusions

This study has provided a framework for the generation of key intrinsic tissue level material properties measures, such as elastic modulus, that describe callus quality within the framework of experimental bone fracture healing studies. Our results have demonstrated that functional mechanical assessment of bone fracture healing and therapeutic manipulation of healing through MSC transplantation is possible through the inverse FEA procedure that we have developed. Utilizing this methodology, results were obtained that create a clear picture of the change in elasticity of the callus tissue throughout early and late-stage healing, as well as changes in the elasticity of callus tissue due to MSC transplantation. Also, we have challenged the assumption of microCT as a sufficient surrogate for direct mechanical property measurement in the determination of callus quality.

# CHAPTER V

# QUANTIFYING MECHANICAL PROPERTIES IN A MURINE FRACTURE HEALING SYSTEM USING AN INVERSE GEOMETRIC NONLINEAR ELASTICITY MODELING FRAMEWORK

## Introduction and Contribution of Study: Part A

The inverse methodology presented in the previous chapters utilizes a purely linear elastic model, which as a theoretical basis utilizes a theory of application of only small strains. However in practice this assumption is not entirely valid. During the mechanical testing procedure, the area of the callus that is contained within the fracture gap is subjected to considerable strain as the deformation is confined to this rather soft area (in comparison to the very stiff cortical bone regions). This considerable amount of strain thus fails to satisfy the 'small strain' assumption, and therefore for an enhanced level of modeling accuracy/sophistication this high strain region may be accounted for. One such approach, as used within this chapter, is to utilize a geometrically nonlinear approach in which a series of small strains are modeled sequentially whereby the deformation from each strain level is added back to the model position prior to the next strain level. This approach is often referred to as a 'moving mesh'. As an added benefit, the geometrically nonlinear approach generates model calculated force/displacement curves that are uniquely nonlinear in nature and with the incorporation of this additional unique nonlinear model data, this the inverse technique using this model is capable of reconstructing multiple material properties, as opposed to the limit of a single material property in the case of purely linear elastic models. The studies contained within this

chapter utilize this approach and challenge the concept of single material property reconstruction by reconstruction of the Lame' constants through the use of a geometrically nonlinear approach. This study was presented as a conference paper at the 5th International Symposium of Biomedical Simulation by Dr. Michael I. Miga in 2010.

Appearing in:

Michael I. Miga, Jared A. Weis, Froilan Granero-Molto, and Anna Spagnoli. Quantifying mechanical properties in a murine fracture healing system using an inverse geometric nonlinear elasticity modeling framework. 5th International Symposium on Biomedical Simulation, Lecture Notes in Computer Science, Springer, Vol. 5958, pp. 29-37, 2010.


## Abstract

Understanding bone remodeling and mechanical property characteristics is important for assessing treatments to accelerate healing or in developing diagnostics to evaluate successful return to function. The murine system whereby mid-diaphaseal tibia fractures are imparted on the subject and fracture healing is assessed at different time points and under different therapeutic conditions is a particularly useful model to study. In this work, a novel inverse geometric nonlinear elasticity modeling framework is proposed that can reconstruct multiple mechanical properties from uniaxial testing data. This is investigated within the context of a murine cohort (n=3) that are 14 days post fracture. This work is the first to report mechanical properties of a callus using an inverse problem methodology whereby 2758.4 ± 682.5 kPa, 0.467 ± 0.009 were found to

be the Young's modulus and Poisson's ratio, respectively. In addition better consistency of the reconstructed metrics over more traditional metrics is demonstrated.

## Introduction

There is significant morbidity and mortality due to the improper or inhibited healing of bone fractures and is especially relevant to the aging population [78-80]. Restoration of mechanical function to bone is an important healthcare concern and processes to accelerate that process or mediate more successful outcomes is of high significance. In addition, the development of diagnostics that can assess the mechanical function of bone are equally important. Murine systems have become natural platforms for the investigation of therapeutics towards improved healing [81] and ex vivo mechanical testing has served as the primary means to assess efficacy [83, 84]. However, due to confounding geometric effects associated with callus growth and remodeling, robust metrics of evaluation are challenging.

To address this, investigators have begun to explore using the detailed structure provided by microCT imaging to facilitate general imaging metrics as well as computational approaches to assess mechanical function using more subject specific models/metrics [35, 46, 66, 85, 86]. In this paper, an approach is investigated which looks at the problem more within the context of an inverse problem approach. Similar to work by Shefelbine et al. [46] and Weis et al. [85, 86], a finite element framework is used to generate subject-specific callus models. In this work, an inverse methodology is investigated which represents a significant advance to addressing the problem with computational techniques.

# Methods

## Inverse geometric nonlinear elasticity modeling framework

Hooke's Law is a widely used constitutive law to represent the stress-strain behavior of a material. In the case of uniaxial loading (Figure 25), the full strain state can be expressed with respect to the applied force as shown here,

$$\varepsilon_x = \frac{\sigma_x}{E}, \varepsilon_y = -\nu\frac{\sigma_x}{E}, \varepsilon_z = -\nu\frac{\sigma_x}{E}, \gamma_{xy} = \gamma_{xz} = \gamma_{yz} = 0 \qquad (1)$$

where E is Young's modulus and often referred to as the stiffness, and $\nu$ is Poisson's ratio which represents the negative ratio of transverse to axial strain. When conducting mechanical testing, the traditional technique is to prepare a sample with known shape such that the cross-sectional area, A, and reference length, L, are known, and the displacements and forces applied are measured by the testing device. This allows one to take that data and calculate the stiffness of the specimen with, $E = \frac{FL}{A\delta}$ where F is the measured force for the given displacement $\delta$. Typically with this approach a series of displacements are used that span the small strain region of the material characteristic curves and a modulus is fit.

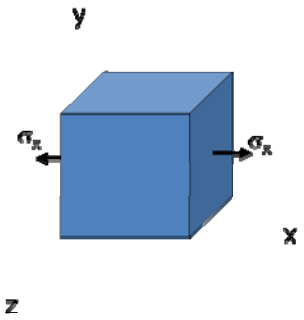


Figure 25. Uniaxial loading.

Of course, the reality is that with the application of an increment of displacement, a change to the cross-sectional area (via Poisson's ratio) is imparted and ultimately affects the measured force. This nonlinear effect is due to the specimen changing shape. To demonstrate, in a simple analytical experiment, a 1 cm cube under tensile loading experienced strains from 0-10% with E=1 MPa (a reasonable approximation to callus stiffness) and a Poisson's ratio of $\nu$=0.3. Figure 27A illustrates the two respective stress-strain curve where 'L' and 'GNL' represent the linear and geometrically nonlinear approaches, respectively. Figure 27b demonstrates the difference in force when taking geometric nonlinearity into account over a range of Poisson's ratio. This is produced by incrementally deforming the specimen cube and accumulating the force at each increment, which is a common strategy to linearize geometric nonlinear problems. As can be seen in Figure 27b, a distinctive force versus strain curve is generated for each Poisson's ratio. This is directly related to the geometric changes to cross-sectional area as reflected by varying Poisson's ratios.

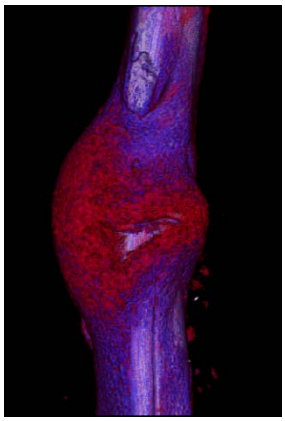

Figure 26. Image showing callus consistency. Rendering utilizes transparency to reflect bone composition with (red) cartilage, (blue) new bone, and (white) highly mineralized bone.

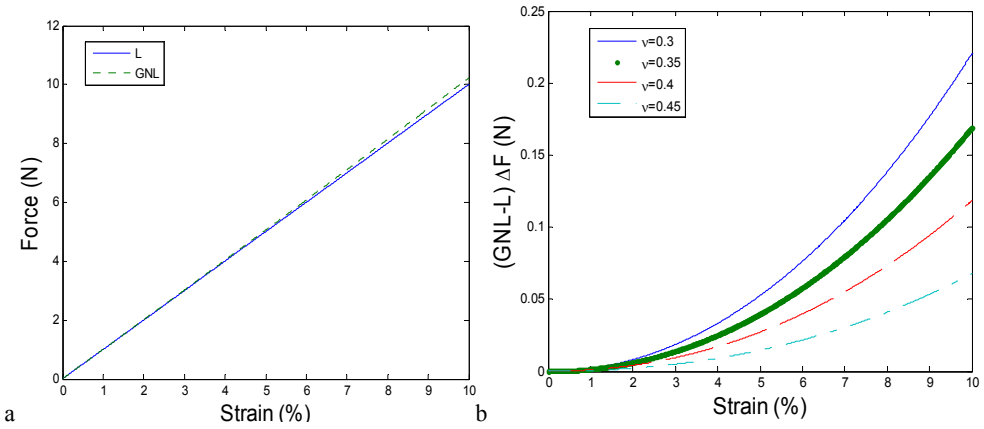


Figure 27. (a) Force versus strain for linear and geometrically nonlinear problems, (b) the difference in force values over several Poisson's ratios.

We hypothesize that by taking into account geometrically nonlinear effects within an inverse reconstruction framework that multiple properties can be differentiated from uniaxial testing data. More specifically, we propose to model the geometric nonlinearity in a similar manner as the above analytic example whereby with each increment we deform the mesh and then impart the next increment. The measured forces are then determined by summing the increments. For the application herein concerned with the

mechanical integrity of a healing callus, more dramatic changes are expected than the homogeneous example discussed above. In addition, for this paper the callus is being 'lumped', i.e. characterized, as one region with unique mechanical properties. Figure 26 illustrates the typical callus region extracted from μCT data and its geometrical complexity consisting of cartilage (red), new bone (blue), and highly mineralized bone (white). As a dynamic grid finite element model is implemented under tensile load, one can easily note that the geometric relationships between these callus constituents will rapidly change which will manifest in changes to the incremental force.

For the purpose of reconstructing multiple material parameters for the callus region, the model for mechanical equilibrium will be expressed in terms of Lame' constants and is stated here,

$$G\nabla^2\bar{u} + (G+\lambda)\nabla(\nabla \bullet \bar{u}) = 0, \qquad (2)$$

where G is the shear modulus, $\lambda$ is the second Lame' constant, and $\bar{u}$ is the displacement vector. With an initial guess at these material parameters, a finite element model of the domain shown in Figure 26 can be constructed, analogous displacements are imposed that match the experimental conditions, and an average force ($F_{calc}$) is reconstructed from the simulation. A custom-built Levenberg-Marquardt non-linear optimization algorithm is then used to iteratively optimize the material properties such that $F_{calc}$ approaches the experimental material tester generated force ($F_{exptl}$). In this approach, each strain level is treated as an independent data point with respect to determining the mechanical properties. The important aspect to the approach is that each strain state represents an accumulation effect associated with approximating the geometric nonlinearity. Ultimately this translates to the objective function,

$$\Psi(G,\lambda) = \sum_{i=1}^{N} \left(F_{calc} - F_{exptl}\right)_i^2 \qquad (3)$$

where N is the number of displacement data points along the elastic region of the force-displacement curve. The goal is to minimize this objective function with respect to two mechanical properties, G and λ, of the 'lumped' callus region. To optimize this for the callus properties, the derivative of our objective function, $\Psi(G,\lambda)$, is taken with respect to the properties G and λ, and set equal to zero, i.e.

$$\begin{bmatrix} \frac{d\Psi(G,\lambda)}{dG} \\ \frac{d\Psi(G,\lambda)}{d\lambda} \end{bmatrix} = \begin{bmatrix} \frac{\partial F_{calc1}}{\partial G} & \frac{\partial F_{calc2}}{\partial G} & \cdots & \frac{\partial F_{calcN}}{\partial G} \\ \frac{\partial F_{calc1}}{\partial \lambda} & \frac{\partial F_{calc2}}{\partial \lambda} & \cdots & \frac{\partial F_{calcN}}{\partial \lambda} \end{bmatrix} \begin{Bmatrix} F_{calc1} - F_{exptl1} \\ F_{calc2} - F_{exptl2} \\ \vdots \\ F_{calcN} - F_{exptlN} \end{Bmatrix} = \begin{bmatrix} 0 \\ 0 \end{bmatrix}, \qquad (4)$$

or simplified as,

$$[J]^T \left\{\bar{F}_{calc} - \bar{F}_{exptl}\right\} = 0 \qquad (5)$$

where [J] is the Jacobian matrix. It is important to note that in the above equation each component of the Jacobian is independent and is built over a series of incremental developments. In the case of a fixed mesh/grid counterpart to this approach, each subsequent strain state is just a scalar multiple based on the applied deformations (i.e. double the applied deformation, and double the Jacobian term). The relationship between force and property is just a linear function of applied displacement. However in the GNL approach, each increment provides new information regarding the geometric relationship of the callus constituents. The result is that the standard Levenberg-Marquardt framework contains considerably more information and can be implemented such that multiple mechanical property reconstruction is possible, i.e.

$$\left([J]^T[J] + \alpha I\right)\left[\Delta\bar{P}\right] = [J]^T\left\{\bar{F}_{calc} - \bar{F}_{exptl}\right\}, \qquad (6)$$

and

$$\left[\Delta\bar{P}\right] = \begin{bmatrix} G \\ \lambda \end{bmatrix}_{i+1} - \begin{bmatrix} G \\ \lambda \end{bmatrix}_{i}, \tag{7}$$

with the regularization term $\alpha$ defined as,

$$\alpha = \left(\phi * \text{trace}\left([J]^T [J]\right) * SSE^2\right)^{1/2} \tag{8}$$

[64], where $\phi$ is an empirical factor and SSE is the sum squared error between measured and calculated force. It should be noted that the Jacobian was determined by a finite difference calculation which was initiated by a 2.5% perturbation from the initial guess of the callus property. The process is iterative until the relative error between iterations converges below a set tolerance or until no improvement in objective function is noted. With respect to reporting the values in this paper, the Lame' constants were converted to Young's modulus and Poisson's ratio for the purpose of comparing with the more traditional metrics. In addition, two other reconstructions were executed whereby Poisson's ratio was fixed ($\nu$=0.45) and Young's modulus was determined using the linear and geometric nonlinear approaches for a single property.

Murine system

Three female syngenic FVB mice (FVB-NJ, Jackson Laboratories) 8 to 12 weeks old with a pin-stabilized mid-diaphaseal tibia fracture were generated. Procedural implementation utilized a standard three point bending system for fracture delivery [87], anesthesia, and pain control and was approved by the Institutional Animal Care and Use Committee at Vanderbilt University Medical Center and the University of North Carolina at Chapel Hill. At day 14, the mice were euthanized and tibia fractures were dissected, and wrapped in phosphate buffered saline (PBS) soaked gauzed. The specimens were

then placed within a Scanco μCT 40 scanner (Scanco Medical) and an approximate 5 mm section was scanned for each specimen which consisted of callus and bone ends. Once completed, each specimen was prepared for mechanical testing by embedding each end within a customized polymethylmethacrylate cast such that it could be placed within the testing unit while also allowing the callus to remain exposed and free of constraints. The assembly was placed with an Enduratec Electroforce 3100 mechanical tester (Bose, Enduratec Systems Group) and tested in tension at a fixed displacement rate of 0.25 mm/min using a 22 N force transducer (Honeywell Sensotec). Data consisted of displacement and force values and was recorded continuously until failure. Figure 28 shows a murine tibia being tested.

Figure 28. A murine mouse tibia loaded within the testing apparatus.

Once the collection of the imaging and displacement data is complete, the bone/callus regions are segmented from the μCT data, a tetrahedral grid is generated, and properties are assigned to mineralized bone and void regions. In this work, highly

mineralized bone (white regions in Figure 26) were assigned E=5 MPa, and ν=0.3 MPa [63], while voids within the domain were assigned negligible material properties. With the computational model and data in place, these are then provided to the inverse approach. In this paper, three inverse approaches are generated: (1) a single callus shear modulus reconstruction using the static mesh, (2) a single callus shear modulus value using the dynamic grid, and (3) a dual callus reconstruction of the Lame' constants using the dynamic grid. In addition, the apparent stiffness, and normalized apparent stiffness are reported which are common metrics within the literature. Apparent stiffness is the slope of the best fit line to force versus displacement data within the linear loading phase. Normalized apparent stiffness is the same fitting procedure but with the force and displacement values normalized by the largest cross-sectional area of the callus and overall length, respectively.

## Results

Figure 29 illustrates a typical result from the model generation process. Figure 30 illustrates the force versus displacement curves for all (n=3) mice. Table 10 reports the mechanical property metric types in the first column with their corresponding value in the second column. While statistical significance from such a small data set cannot be achieved at this time it is interesting to look at the magnitude of the standard deviations relative to the mean property across the different metrics (reported in column 3 of Table 1).

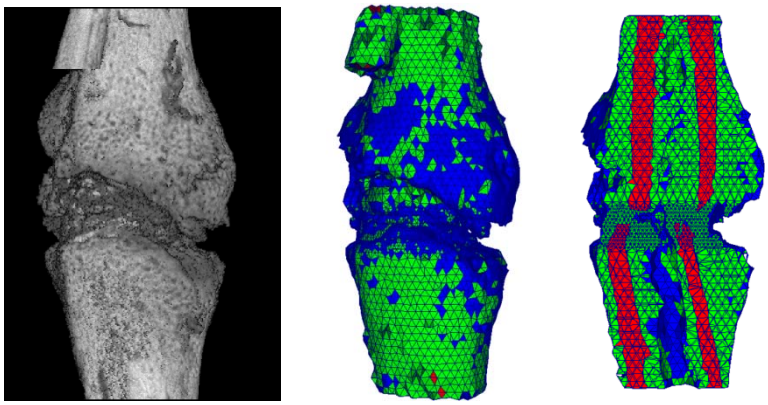

Figure 29. (left) Volume rendered μCT of callus, (middle) tetrahedral grid of volume, (right) cross-section through mesh. (red is bone ends, green is callus, and blue is voids).

Table 10. Metrics for mechanical properties assessed over (n=3) mice.

| PROPERTY | 14 d (n=3) | **SD as % of mean** |
|---|---|---|
| Apparent Stiffness (N/mm) | 13.95 ± 6.24 | 44.7% |
| Normalized Apparent Stiffness (kPa) | 8330.1 ± 4941.0 | 59.3% |
| $E_{reconstructed}$ (kPa)<br>Linear (ν=0.45 fixed) | 2908.3 ± 872.8 | 30.0% |
| $E_{reconstructed}$ (kPa)<br>Geometric NonLinear (ν=0.45 fixed) | 3230.2 ± 986.7 | 30.5% |
| $E_{reconstructed}$ (kPa), $\nu_{reconstructed}$<br>Geometric NonLinear (dual property) | 2758.4 ± 682.5, 0.467 ± 0.009 | 24.7%,<br>1.9% |

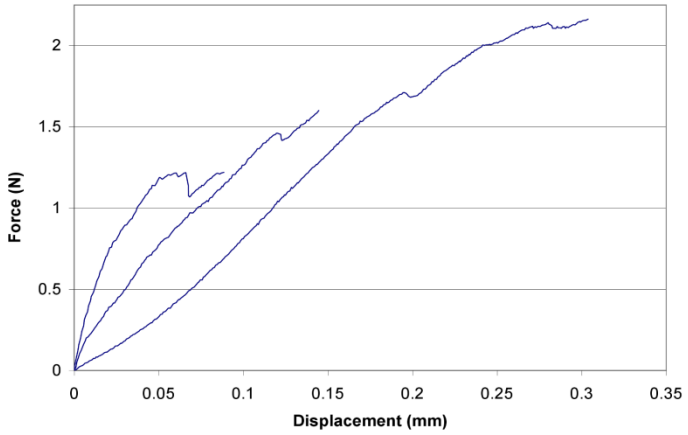


Figure 30. Force versus displacement for (n=3) mice. Only regions prior to an approximate elastic limit were analyzed as part of the reconstructive analysis.

## Discussion

The methods reported have shortcomings at this early stage but nevertheless the results are promising. Some of those short comings are: (1) lack of finer discretization of the callus models as shown in Figure 29, (2) the choice of tetrahedral elements as opposed to ones more accurate in mechanics modeling, e.g. hexahedral elements [88], (3) although the grid is dynamic in the geometric nonlinear approach, the lack of re-meshing for the intermediate steps to ensure optimal element aspect ratios, (4) the high strain conditions within the fracture fissure likely need the full-nonlinear strain tensor description, (5) lack of more data necessary to achieve statistical significance, and (6) the inherent experimental error associated with 'potting' tibia fractures and mechanical testing. Despite this however, it is encouraging that the reconstructed values are quite consistent among the widely distributed force/displacement curves. The heterogeneity among these curves can be seen in the considerably large standard deviation of the apparent stiffness and the normalized apparent stiffness as compared to their mean values. Comparing quantitatively, the standard deviations of the apparent stiffness values are approximately 45-60% relative to the mean value while reconstructed values using the inverse approaches are only 25-30% of the mean. This suggests that model-based inverse analysis produces a more consistent metric. The considerable 15% increase in variation when normalizing the apparent stiffness suggests that the process of normalization introduces variability and would seem to confirm the confounding effects of geometry often referred to in the literature. The contribution of the work is that this represents to our knowledge the only inverse elasticity approach to this problem. Because the approach is based on measured force, each result from the three variants to

the algorithm represents a quantitative value. As the shortcomings are overcome, better absolute quantification will be achieved, but even as realized here, the approach may serve as an effective means to differentiate and score different treatment groups at different time points. In fact, in recent work not reported here, the ability to differentiate different time (10 day, 14 day post-fracture) points of healing under similar fracture conditions has been found in an expanded cohort (n=6) of mice. Interestingly, the reconstructive analysis was the only method to find statistical significance among the two groups [86].

## Conclusion

This paper presents a novel inverse approach that takes advantage of geometric nonlinearities to increase the extent of information such that the reconstruction of multiple material properties is achieved. It also goes on to compare different realizations of the approach and compares these to more common metrics to qualify mechanical properties in a murine fracture system. The results indicate a more consistent result across mice using the model-based analysis. Future work will involve investigating if the method can be used to differentiate mice at different healing points and among different treatments.

## Introduction and Contribution of Study: Part B

This study is a follow-up to the study in part A, in which a larger cohort of mice encompassing 2 different stages of healing (at 10 days post-fracture and 14 days post-fracture) are assessed using a similar geometrically nonlinear approach. In this study,

Lame' constants are reconstructed and compared across the groups along with other metrics of fracture healing. This study was presented as a conference paper at the SPIE Medical Imaging 2010 conference by Dr. Michael I. Miga.

Appearing in:

Michael I. Miga, Jared A. Weis, Froilan Granero-Molto, and Anna Spagnoli. Quantifying mechanical properties in a murine fracture healing system using inverse modeling: preliminary work. SPIE Medical Imaging 2010: Visualization, Image-Guided Procedures, and Modeling Conference, 2010.


Abstract

Understanding bone remodeling and mechanical property characteristics is important for assessing treatments to accelerate healing or in developing diagnostics to evaluate successful return to function. The murine system whereby mid-diaphaseal tibia fractures are imparted on the subject and fracture healing is assessed at different time points and under different therapeutic conditions is a particularly useful model to study. In this work, a novel inverse geometric nonlinear elasticity modeling framework is proposed that can reconstruct multiple mechanical properties from uniaxial testing data. To test this framework, the Lame' constants were reconstructed within the context of a murine cohort (n=6) where there were no differences in treatment post tibia fracture except that half of the mice were allowed to heal 4 days longer (10 day, and 14 day healing time point, respectively). The properties reconstructed were a shear modulus of G=511.2 ± 295.6 kPa, and 833.3± 352.3 kPa for the 10 day, and 14 day time points

respectively. The second Lame' constant reconstructed at $\lambda$=1002.9 ±42.9 kPa, and 14893.7 ± 863.3 kPa for the 10 day, and 14 day time points respectively. An unpaired Student *t*-test was used to test for statistically significant differences among the groups. While the shear modulus did not meet our criteria for significance, the second Lame' constant did at a value $p<0.0001$. Traditional metrics that are commonly used within the bone fracture healing research community were not found to be statistically significant.

## Introduction

A critically important function of bone healing is that the healing tissue provides sufficient mechanical stabilization such that a return to functionality is possible. Because fracture healing is a phenomenon that modulates the mechanical stability of a broken bone, within the clinical context there is an important need to monitor the mechanical properties of a healing callus so that a clinician may detect and intervene in the event of a non-union. In addition, there is an equally important need to understand how to therapeutically promote better and more mechanically stable fracture healing. As a result, many researchers are studying fracture healing animal models within the context of treatment therapeutics [81, 89-95]. While a great deal of work has been targeted at assessment of healing via imaging methods [27-34], there is real need to monitor and characterize the load-bearing mechanical properties of an experimental fracture callus system in response therapeutic intervention. To date, the level of sophistication associated with these mechanical characterizations has been somewhat simplistic. Early analysis techniques used idealized assumptions regarding geometry (e.g. beam theory) and attempted to correlate force-displacement data acquired through biomechanical

testing (usually three-point bending). More recently, investigators have begun to explore novel medical imaging technologies as well as more sophisticated modeling methods [35, 46, 66, 85]. Some studies have attempted to generate statistical models whereby microCT metrics are correlated with the results of torsional strength experiments [35, 66]. In these approaches, the challenge is that callus' often have a great deal of geometric complexity under similar initial conditions. This creates difficulty in generating proper normalized metrics such that large sample sizes are not necessary. Others have begun to explore the use of subject-specific finite element (FE) models. However these studies tend to compare empirical torsional strength data of the specimen to simulated data whereby the objective is to determine a mathematical relationship between mechanical properties and microCT intensity [46]. The difficulty with this approach is that each system (e.g. different therapeutics, healing time point, initialization, etc.) could potentially generate a different relationship. Establishing these relationships would require many mice per system which could prove to be cumbersome.

In this paper, an approach is investigated which looks at the problem more within the context of an inverse finite element (FE) methodology. In previous work, the approach was reported using a linear Hookean elastic model of the callus [86]. It analyzed the 10-day and 14-day healing time point data reported here and found that the inverse-based metric was the only metric to show statistical significance. The unusual aspect to the work reported in this paper is that it tries to take advantage of the inherent geometric nonlinear nature of deforming soft tissue to discern more information regarding callus mechanical properties. More specifically, by incorporating an incremental moving mesh strategy, each data point along the force/displacement testing

curve becomes a solution to a unique elastic problem and increases the degrees of freedom for fitting material properties. The results reported below show a considerable improvement to the statistical significance.

## Methods

### Geometric nonlinear approach to an inverse elasticity analysis

A linear elastic continuum is one of the fundamental models used in many biomechanics applications. To reflect this, Hooke's Law is the widely used constitutive law for representing the stress-strain behavior of the material. The model speaks to the basic principle of mechanical equilibrium and can be represented by the partial differential equation,

$$\mathbf{G}\nabla^2\bar{\mathbf{u}} + (\mathbf{G}+\lambda)\nabla(\nabla \bullet \bar{\mathbf{u}}) = 0 \qquad (1)$$

where G is the shear modulus, $\lambda$ is the second Lame' constant, and $\bar{\mathbf{u}}$ is the displacement vector. With respect to usual computational practice, equation (1) would be solved using some sort of numerical technique such as the finite element method. In so doing, a geometric mesh would be generated, the partial differential equations (PDEs) would be integrated over each of the mesh subunit domains, collected into a matrix of equations, and the displacements would be solved throughout the domain simultaneously. Conventionally, this represents a linear solution, i.e. a solution to a particular boundary valued problem in this manner is unique and scalable (e.g. scaling the boundary contributing boundary conditions scales the solution by the same factor). One interpretation of a geometric nonlinear framework would be to represent the boundary

conditions incrementally, and with the application of each increment, the geometric domain is altered. This results in a path dependence based on shape change for the elastic domain as well as the final solutions being presented as an accumulation of increments. Figure 31 illustrates the concept of a geometric nonlinear problem. In Figure 31a, the computation model is based on the first state of the callus. From that statement, a boundary condition set is applied that deforms the system $\delta$. Upon the completion, the model from first state is executed again with a boundary condition displacement reflecting twice that of $\delta$. In this case, the solution to the second problem need not be constituted because it only represents a scaling of the first (just multiplying the first solution by the scale factor 2 in this is sufficient). Similarly, if one were to reconstruct the force profile that generated the displacement $\delta$, the finding would be that twice the force is necessary for the second state. This represents the nature of a linear solution to a PDE on a fixed domain. In Figure 31b, a change can be seen. In this solution, the mesh is allowed to deform to a new shape based on the initial boundary condition application of $\delta$. From this new domain shown in state 2, another $\delta$ boundary condition displacement is applied. In this case, if I were to constitute the forces applied between state 1 and state 2, and between state 2 and state 3, they would not be equal. This is because the shape of the domain has changed and in so doing the manner in which stress is conveyed has changed.

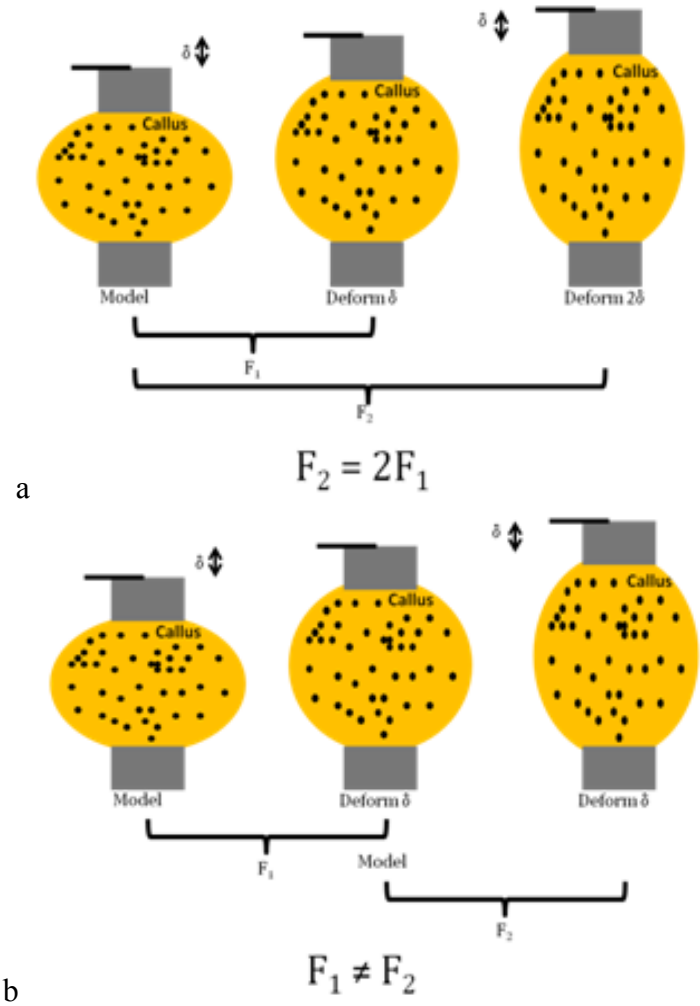


Figure 31. (a) 3 callus states whereby the model is based on state 1 and displacement δ is applied twice from the base state, (b) 3 callus states whereby the model is based on state 1, a displacement δ is applied, the model is reconstituted in its deformed state, and second displacement δ is applied.

We hypothesize that by taking into account geometrically nonlinear effects within an inverse reconstruction framework that multiple properties can be differentiated from uniaxial testing data. More specifically, we propose to model the geometric nonlinearity in a similar manner as the above descriptive example whereby with each increment we deform the mesh and then impart the next increment. The measured forces are then

determined by accumulating the differential increments. It should also be noted that for this paper the callus is being 'lumped', i.e. characterized, as one region with unique mechanical properties. Figure 32 illustrates the typical callus region extracted from μCT data and its geometrical complexity consisting of cartilage (red), new bone (blue), and highly mineralized bone (white). Observing Figure 32, one can easily note that in a dynamic mesh FE calculation, the callus constituents will change in relation to each other spatially which will ultimately translate to changes in the incremental force. While this approach is interesting, there are some inherent problems too that will also be discussed. However, in this preliminary investigation, it was intriguing to note the improvement in significance between the two mouse groups as the results will indicate.

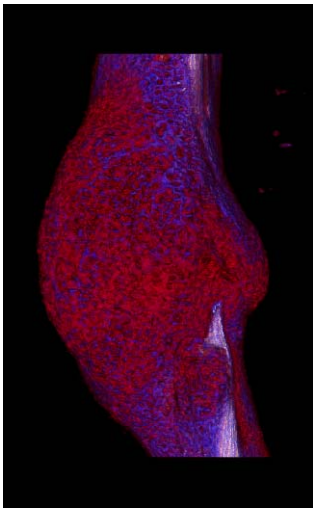

Figure 32. Image showing callus consistency. Rendering utilizes transparency to reflect bone composition with (red) cartilage, (blue) new bone, and (white) highly mineralized bone.

The model equations for our system are shown in equation (1) with the caveat that a dynamic grid will be utilized in the construction process. With an initial guess at these material parameters, a finite element model of the domain shown in Figure (2) can be constructed, analogous displacements are imposed that match the experimental counterpart, and an average force ($F_{calc}$) is reconstructed from the simulation. A custom-built Levenberg-Marquardt non-linear optimization algorithm is then used to iteratively optimize the material properties such that the least squared error between $F_{calc}$ and the experimental material tester generated force, $F_{exptl}$, is minimized. Ultimately this translates to the objective function,

$$\Psi(G,\lambda) = \sum_{i=1}^{N} \left(F_{calc} - F_{exptl}\right)_i^2 \tag{2}$$

where N is the number of displacement data points along the elastic region of the force-displacement curve. The goal is to minimize this objective function with respect to two mechanical properties, G and λ, of the 'lumped' callus region. To optimize this for the callus properties, the derivative of our objective function, $\Psi(G,\lambda)$, is taken with respect to the properties G and λ, and set equal to zero, i.e.

$$\begin{bmatrix} \frac{d\Psi(G,\lambda)}{dG} \\ \frac{d\Psi(G,\lambda)}{d\lambda} \end{bmatrix} = \begin{bmatrix} \frac{\partial F_{calc1}}{\partial G} & \frac{\partial F_{calc2}}{\partial G} & \cdots & \frac{\partial F_{calcN}}{\partial G} \\ \frac{\partial F_{calc1}}{\partial \lambda} & \frac{\partial F_{calc2}}{\partial \lambda} & \cdots & \frac{\partial F_{calcN}}{\partial \lambda} \end{bmatrix} \begin{Bmatrix} F_{calc1} - F_{exptl1} \\ F_{calc2} - F_{exptl2} \\ \vdots \\ F_{calcN} - F_{exptlN} \end{Bmatrix} = \begin{bmatrix} 0 \\ 0 \end{bmatrix}, \tag{3}$$

or simplified as,

$$[J]^T \left\{\overline{F}_{calc} - \overline{F}_{exptl}\right\} = 0 \tag{4}$$

where [J] is the Jacobian matrix. It is important to note that in the above equation each component of the Jacobian is independent and is built over a series of incremental developments. In the case of a fixed mesh/grid counterpart to this approach, each

subsequent strain state is just a scalar multiple based on the applied deformations. The standard Levenberg-Marquardt framework contains considerably more information and can be implemented such that multiple mechanical property reconstruction is possible, i.e.

$$\left(\left[J\right]^T\left[J\right]+\alpha I\right)\left[\Delta\overline{P}\right]=\left[J\right]^T\left\{\overline{F}_{calc}-\overline{F}_{exptl}\right\}, \tag{5}$$

and

$$\left[\Delta\overline{P}\right]=\begin{bmatrix}G\\ \lambda\end{bmatrix}_{i+1}-\begin{bmatrix}G\\ \lambda\end{bmatrix}_{i}, \tag{6}$$

with the regularization term $\alpha$ defined as,

$$\alpha=\left(\phi * \text{trace}\left(\left[J\right]^T\left[J\right]\right)* SSE^2\right)^{1/2} \tag{7}$$

[64], where $\phi$ is an empirical factor, and SSE is the sum squared error between measured and calculated force. It should be noted that the Jacobian was determined by a finite difference calculation which was initiated by a 2.5% perturbation from the initial guess of the callus property. The process is iterative until the relative error between iterations converges below a set tolerance or until no improvement in objective function is noted. With respect to reporting the values in this paper, the Lame' constants were reported but they were also converted to Young's modulus and Poisson's ratio for the purpose of comparing with the more traditional metrics and the results from [86].

Experimental murine system

Female syngenic FVB mice (FVB-NJ, Jackson Laboratories) 8 to 12 weeks old were anesthetized using isofluorane to provide deep anesthesia. Pin stabilized mid-diaphyseal tibia fractures were generated by insertion of a 0.25 mm stainless steel pin

(Fine Science Tools) through the tibial tuberosity followed by fracture creation using a three point bending device with a standardized force. Immediately following tibia fracture, 0.5 mg/kg of bupremorphine was administered for pain control. On the specified post-fracture day, mice were euthanized, fractured tibias were dissected and wrapped in phosphate buffered saline (PBS) soaked gauze and stored at -80 °C until further analysis. Using this methodology, a preliminary study (n=6) was conducted where there were no differences in treatment post tibia fracture except that half of the mice were allowed to heal 4 days longer (10 day, and 14 day healing respectively))[86]. Intuitively, mice allowed to heal longer should have a more stabilized callus (i.e. stiffer) in the fracture region. The results of that study are reported below. All animal studies were approved by the Institutional Animal Care and Use Committee at Vanderbilt University Medical Center.

CT scans of the extracted specimens were performed using a Scanco microCT 40 scanner (Scanco Medical) and were obtained at 55 kVp, 145 μA, 300 ms integration time using 12 μm voxel resolution along 5.2 mm length centered at the fracture line with a total scanning time of approximately 1 hour [66]. Figure 32 is an example of a microCT volume of data from this preliminary fracture/callus healing study [86]. These microCT reconstructions were then used for subsequent FE analysis and volume measurements.

As inverse techniques require true data comparison to effectively reconstruct callus elastic properties, fractured tibia ends were embedded into a polymethylmethacrylate cast using custom designed testing fixtures, leaving the fracture callus exposed. Specimens are kept fully hydrated with PBS during the entire testing procedure. The fixtures were loaded into the mechanical tester (Enduratec ELF 3100)

and tested in tension at a fixed displacement rate of 0.25 mm/min using a 22 N transducer (Honeywell Sensotec) [67]. Displacement and force data were recorded until failure. Reproduced from [86], Figure 33 shows the data from all 6 subjects. While distinction among the two groups can be seen visually, there is a significant amount of spread within each group.

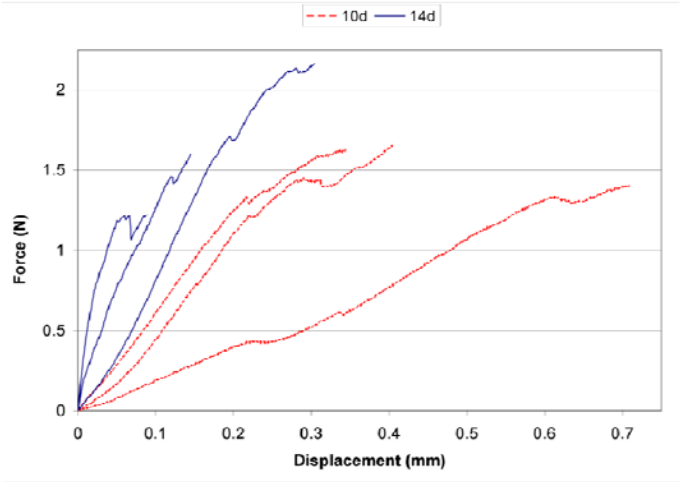


Figure 33. BMT force versus displacement data reproduced from [86] of each tibia fracture callus tested at day 10 and day 14 post fracture during distraction-to-failure testing. Note the wide sample variation within each group, demonstrating confounding geometrical effects.

## Results

Table 11 illustrates the results of the reconstruction as well as the comparison of the linear reconstruction from [86]. Figure 34a illustrates the mean and standard deviation of routine biomechanical testing metrics while Figure 34b illustrates the reconstructed material parameters with the linear reconstructed Young's modulus, followed by the nonlinear reconstructed Lame' constants, and the reformatted nonlinear values into

Young's modulus and Poisson's ratio (note each has been normalized by its 14-day value).

Table 11. Results for biomechanical testing (BMT) metrics for 10day and 14day mice.

| | 10 d (n=3) | 14 d (n=3) | P Value |
|---|---|---|---|
| **Ultimate Load (N)** | 1.56 ± 0.14 | 1.64 ± 0.49 | 0.79 |
| **Toughness (N*mm)** | 0.41 ± 0.088 | 0.20 ± 0.16 | 0.11 |
| **Apparent Stiffness (N/mm)** | 4.74 ± 2.35 | 14.0 ± 6.2 | 0.08 |
| **Normalized Apparent Stiffness (kPa)** | 3885.3 ± 1799.7 | 8330.1 ± 4941.0 | 0.22 |
| **$G_{linear\ recon}$ (kPa)** | 274.9 ± 142.9 | 1002.9 ± 301.0 | 0.019* |
| **$G_{non\text{-}linear\ recon}$ (kPa)** | 511.2 ± 295.6 | 833.3 ± 352.3 | 0.29 |
| **$\lambda_{non\text{-}linear\ recon}$ (kPa)** | 1002.9 ± 42.9 | 14893.7 ± 863.3 | <0.0001* |

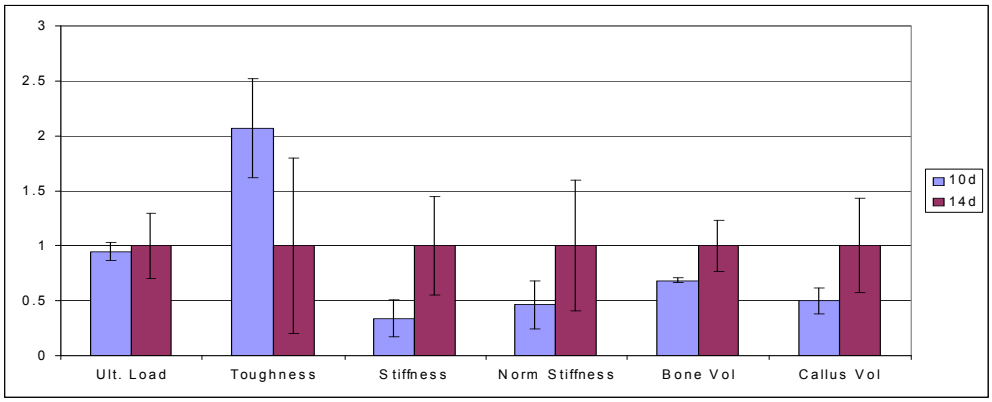


b

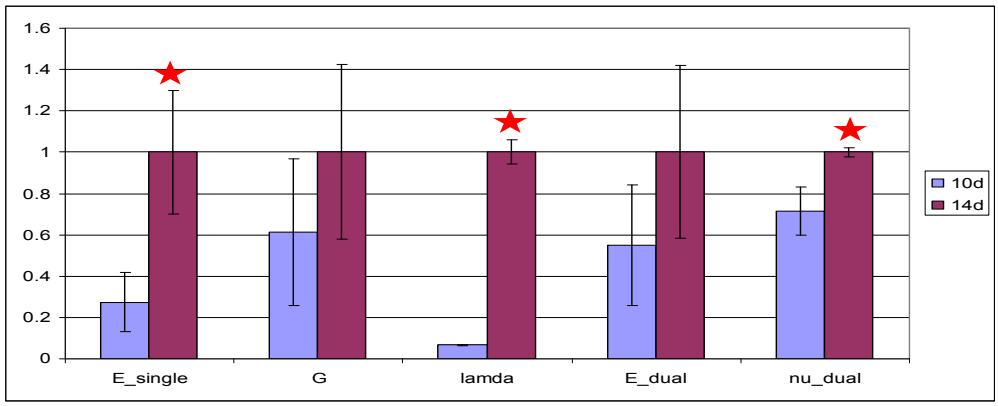


Figure 34. (a) Routine BMT metrics for each mice group, (b) reconstruction properties with the single property reconstruction, reconstructed Lame' constants, followed transformed Lame' constants into Young's modulus and Poisson's ratio (red star indicates statistical significance with $p < 0.05$). Each has been normalized by the 14 day value.

## Discussion

Table 11 and Figure 34 are encouraging in that the nonlinear reconstruction differentiated the two groups more significantly than its linear counterpart (it should be noted that the linear reconstruction used a constant Poisson's ratio, $\nu=0.45$). The other intriguing aspect is that the Lame' constant $\lambda$ was found to be statistically different between groups while the shear modules did not reflect this level of difference. It is likely that given the heterogeneous nature of a healing callus, volumetric changes

probably dominate its load/displacement behavior as opposed to constant-volume distortional shape change.

While the results are suggestive, the methods reported have shortcomings at this early stage. Some of those short comings are: (1) lack of finer discretization of the callus models, (2) the choice of tetrahedral elements as opposed to ones more accurate in mechanics modeling, e.g. hexahedral elements [88], (3) although the grid is dynamic in the geometric nonlinear approach, the lack of re-meshing for the intermediate steps to ensure optimal element aspect ratios, (4) the high strain conditions within the fracture fissure likely need the full-nonlinear strain tensor description, (5) lack of more data necessary to achieve statistical significance, (6) the inherent experimental error associated with 'potting' tibia fractures and mechanical testing, and (7) determining how much measurement change occurs as a result of nonlinear shape change during mechanical excitation and whether the sensitivity of the force transducer can detect that change.

## Conclusions

A method to reconstruct multiple material properties from uniaxial BMT data using geometrically nonlinear information is presented. An initial study using 6 mice separated into 2 groups differing by an extra 4 days of healing was used as a system to test the inverse elastic property reconstruction. Using the enhanced method, better statistical difference between the groups was achieved. In future work, shortcomings will be addressed as well as future testing of the frameworks within the context of therapeutic challenges.

# CHAPTER VI

# A DUAL-NODE SUBMISSION RESOURCE FOR ANALYSIS OF FRACTURE HEALING MECHANICAL PROPERTIES

## Introduction and Contribution of Study

The previous chapters have detailed the construction, utilization, and effectiveness of an inverse FE analysis methodology for the analysis of fracture healing, however these methods are sophisticated and technically cumbersome and thus prohibitive for general adaptation and usage as a standard fracture healing analysis technique. The challenging nature of the analysis thus necessitates ease-of-use enhancements to facilitate a wider usage among bone biology groups whom are not experts in computational analysis. Therefore this chapter details the conception, construction, and utilization of an online web-enabled model submission system in which bone fracture callus microCT imaging and biomechanical testing are collected with a minimal amount of pre-processing on a remote user node and submitted to a compute node which builds and executes the inverse material property construction. This submission is performed through the use of a simple graphical user interface which facilitates the collection of relevant files, variables, and commands to generate a FE model from microCT data, generate boundary conditions which match the biomechanical testing parameters, and submit the data for inverse analysis. In this scenario, the specifics associated with running the computational model (including software library construction and maintenance and hardware compute cluster setup and upkeep) are transparent to the analysis user and performed at the site of the compute cluster node (where the computational experts reside and the inverse

methodology was developed). This chapter does not involve modifications to the inverse model itself; rather it details the packaging of the inverse methodology within a submission system for general adaptation by non-computational modeling experts. This work is a manuscript in preparation to be submitted.

Appearing in:

Jared A. Weis, Anna Spagnoli, and Michael I. Miga. A dual-node submission resource for analysis of fracture healing mechanical properties. Manuscript in preparation.


## Abstract

The inverse bone fracture callus elastographic characterization methods developed in previous work can be streamlined for more efficient data analysis and facilitation of collaborative utilization by other bone biology groups without the need for extensive expertise in numerical analysis and image processing nor access to extensive computational resources. In this work, we describe a two-node implementation which optimally addresses the differing computational needs of the off-site analysis client and on-site analysis server. We demonstrate the framework's use with an application to bone fracture healing, using microCT and biomechanical testing data to perform inverse material property reconstruction for the purpose of examining differences in healing across treatments. We have developed a software framework for distributed computing which makes significant computational resources available to provide inverse model-assisted material property reconstruction. The only submitted input is the segmented microCT image set and biomechanical testing data from the imaged sample, with the

remainder of the analysis automated. The returned output is the mechanical properties of the bone fracture callus, which serves as a biomarker for fracture healing.

## Introduction

Combining and incorporating microCT and biomechanical testing data into inverse finite element (inverse FE) models to determine mechanical property information for healing bone fracture calluses has been previously shown to provide enhanced discriminatory analysis for determination of functional material property differences in fracture callus tissue [61]. However, the ability to integrate highly resolved computer model information into the analysis of fracture calluses remains challenging. The knowledge and execution of advanced numerical and image processing techniques along with the significant computational resources required to process the bone fracture callus inverse FE models are too cumbersome and thus prohibitive for general adaptation and acceptance within the general fracture healing community.

With this realization, the concept of a dedicated computing resource suitable for solving these problems would seem a promising strategy. Thus we propose that a dedicated computing resource connected by a web-enabled network to a remote analysis user client, and that the capabilities of this computing resource are exposed to the client through a software framework which incorporates model generation from microCT images, boundary condition assignment, and inverse FE material property reconstruction. In particular, we suggest a dual-node approach in which a high-capability compute resource (server) for inverse FE analysis and a low-capability compute resource (client)

for collection and submission of microCT and biomechanical testing data are used jointly.

The concept of a dual-node web-enabled client/server application for the analysis of biological data is not a novel one. For example, the widely used Basic Local Alignment Search Tool (BLAST) [96, 97] represents a similar framework in which the general user submits a text-based nucleotide sequence (or sequence file) via a web-browser to an analysis server which processes it and returns information and data about the gene and homologous gene(s) which that sequence encodes. Similar to our proposed design, the details and execution of the sequence analysis job are performed automatically and transparently to the user. The user needs no expertise in technical computing nor access to significant computational resources in order to execute the gene sequence analysis. The general biology community has thus widely accepted this bioinformatics tool as a sequence/gene analysis method. However this example represents a rather simple realization, in that both the size of the data files being transmitted and the level of sophistication of the analysis are small (analysis consists of database queries). While similar resources have been used for database management and simple analysis, to the best of our knowledge this is the first time such a system has been developed and reported for use in inverse FE model analysis and involves a parallel multi-performance compute resource structure.

## System and Methods

The design of the compute platform is a dual compute node framework for facilitating model-assisted analysis. The framework involves: (i) a high-capability on-

site compute resource which acts as a server to facilitate the inverse analysis and accompanying pre-processing stages (on-site server), and (ii) a low-capability off-site compute resource which acts as a client and generates a minimum data set that can be transmitted to the onsite server (off-site client). In this framework, the off-site client represents a user compute node that would prepare and submit the biomechanical testing and microCT image data, whereas the on-site server represents a compute node for the creation, execution, and processing of inverse FE models. This dual-capability resource compute node concept is managed via software called a compute resource manager (CRM) and the dual node concept represents a promising approach to integrating models with inverse procedures.

The underlying architecture of the CRM is a client-server relationship, in which the client communicates with the server to provide computational services to the user. The CRM manages the clients and the servers independently and transparently. On the client side, the CRM is an application programming interface (API) that integrates with data-management software to collect the necessary data from the user. Therefore, the client collects the data required to execute the inverse FE analysis, namely microCT image and biomechanical testing data. In addition to managing data, the API on the client side allows the user to (a) submit data to the server, (b) ask the server to perform computational routines (in this case the inverse FE analysis), (c) query the status of the computational routines, and (d) retrieve the results once the server compute node completes the computational jobs. On the server side, the CRM has been designed to (a) manage requests from the clients, (b) invoke the computational routines, (c) allocate computational resources and, (d) monitor the status of the computational routines. On the

server the CRM is run as a perpetual process that is always waiting for new input. Additionally, the CRM can handle multiple simultaneous computational jobs from different clients. Figure 35 shows a schematic of the complete dual resource concept applied to inverse FE analysis procedures.

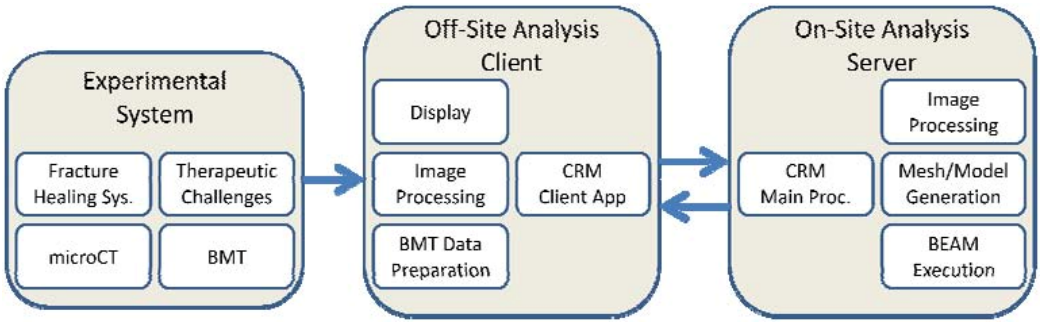


Figure 35. Schematic of the submission system.

The API on the client side has been implemented in the Python language to take advantage of the many flexible data structures native to Python and the client application has been designed in QT. All interactions with the compute node are performed through this interface. On the server side, the CRM has been implemented with a modular design that allows for additional computational routines to be incorporated into the workflow using a plug-in architecture. Data is transferred between the client and the server nodes as serialized, encrypted objects and reconstituted into memory-resident objects on the receiving end. This ensures that data resident on one node can be reproduced on the other and also minimizes the chances of data corruption during the transfer. We have implemented the XML-RPC protocol for transporting input and output data, as well as command/control directives, between the client and server nodes.

The on-site server performs the computations and resultant data is then transferred back to the off-site client for feedback. It is therefore important to carefully manage the flow of data, order of execution, and allocation of services and resources so that the computational routines run smoothly without any system errors. It is also important to relay feedback to the user while the computational routines are being performed on the on-site server and attribute appropriate failure messages to the tasks if the computational routines fail. It should be noted that the CRM acts simply as a software manager for (a) transferring data from the off-site client to the on-site server and vice-versa, (b) for running the computational routines on the on-site server, and (c) relaying feedback messages to clients. The CRM itself does not perform any of the routine tasks associated with initial data preparation, such as segmentation, or the inverse FE model analysis. It should be also noted that any type of computer hardware can be used for the compute node. It can be a desktop GPU computing resource, a multi-processor workstation, or multi-node compute cluster capable of handling the computationally-intensive inverse FE material property reconstruction technique reported in [61]. In this case, we have utilized a 10 node multi-core compute cluster to act as the on-site server.

## Implementation

The process of user submission of a bone fracture healing dataset for inverse FE analysis utilizing the CRM is divided into 4 distinct steps within this work: surface generation, mesh generation, boundary condition assignment, and model submission. Each step is organized as a separate tab within the submission application on the off-site client and has unique data inputs and outputs specific to the particular task being

performed on the on-site server, as discussed below. Common to each tab are options for on-site server selection, job description tags, local output directory, and job submission/retrieval commands. Each individual step in the application represents a logical discretization of the workflow performed in [61] and data is submitted and received to/from the on-site server during each individual step. For each task, the user selects the local location of relevant files needed for upload, assigns job specific parameters, selects a destination off-site compute server, assigns a local output directory for retrieval of output files, tags the job with a job description, and submits the job for processing. Upon submission, the job is assigned a unique job identification number such that the client and server remain synchronized upon which job the client is running. During processing, the user can check the status of the job through a command button, and upon completion the user can retrieve the resultant output files through a command button. While the analysis could be fully automated, the stepwise discretization is important for the user to observe and verify the results of each step prior to proceeding with the next step to ensure the integrity of the final result.

Surface generation

The process of model submission begins with generating a boundary surface description from a segmented microCT image volume using the surface generation tab. The user utilizes commercially available image segmentation tools (such as ANALYZE) to segment the callus-air boundary and the cortical bone-callus boundary and submits, along with parameters for surface creation (element reduction and smoothing parameters), this data to the on-site server for surface generation using the client

application. A screenshot of this tab is seen in Figure 36. Via the CRM, the on-site server receives this data and processes it using a marching cubes surface extraction followed by surface smoothing (performed by the FastRBF Toolbox (Farfield Technologies)). This task is performed automatically and transparently to the user and a smoothed boundary surface is returned to the user once the task is completed by the on-site server.

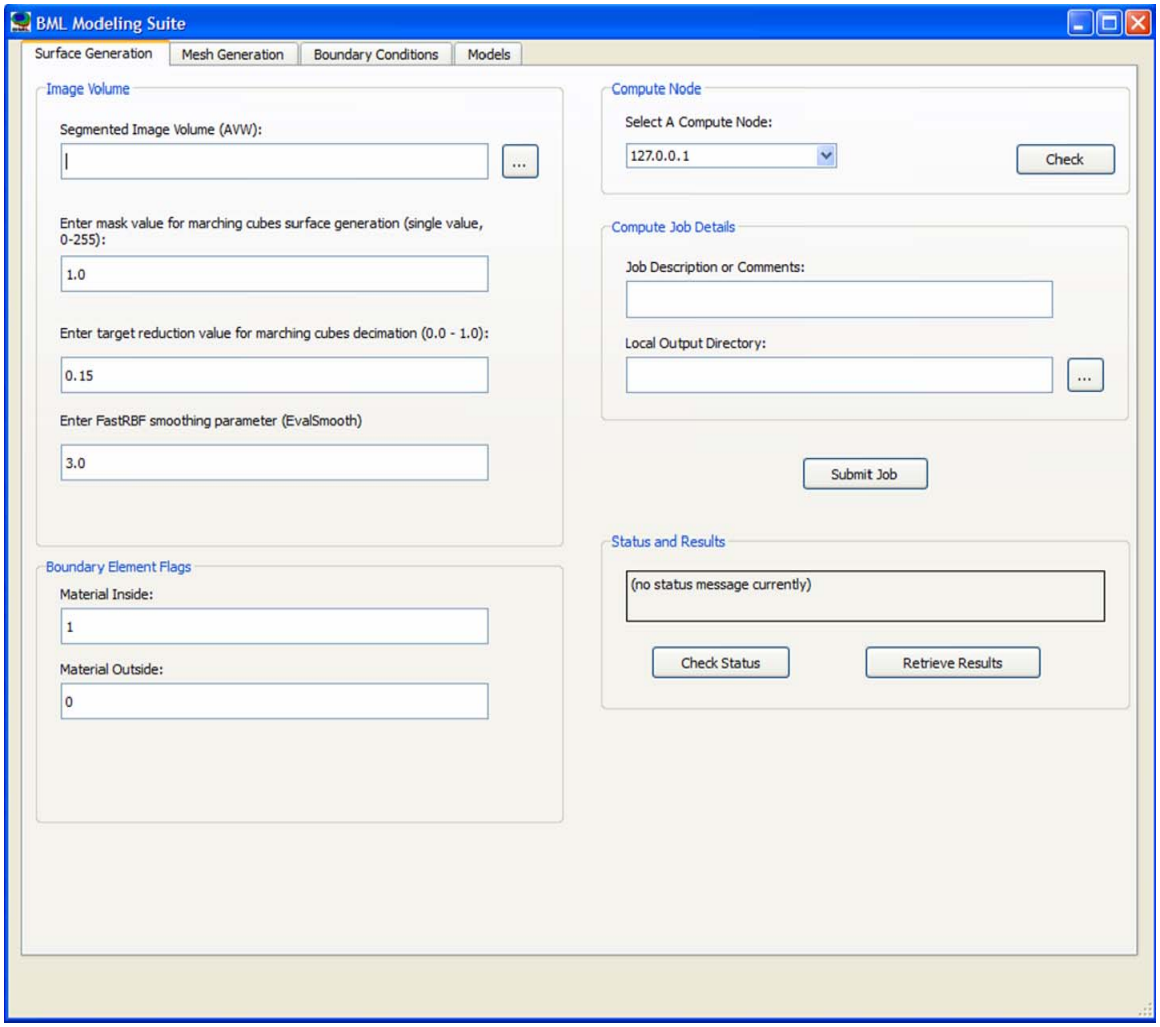


Figure 36. Surface generation interface

Model creation/mesh generation

In the mesh generation tab, FE model mesh generation is performed similarly to that of boundary surface creation, whereby the smoothed marching cubes boundary surface created during the previous step is submitted along with mesh refinement parameters (edge length, optional refinement plane, and image to grid parameters) and a finite element mesh (and its associated boundary element description) is returned to the user once the mesh generation task is completed by the on-site server. Image-to-grid material type classification is performed by the user supplying an AVW image volume file and a list of values that define the material type thresholds. The on-site server generates a tetrahedral FE mesh by utilizing custom-built mesh generation methods [62]. A screenshot of this tab is seen in Figure 37.

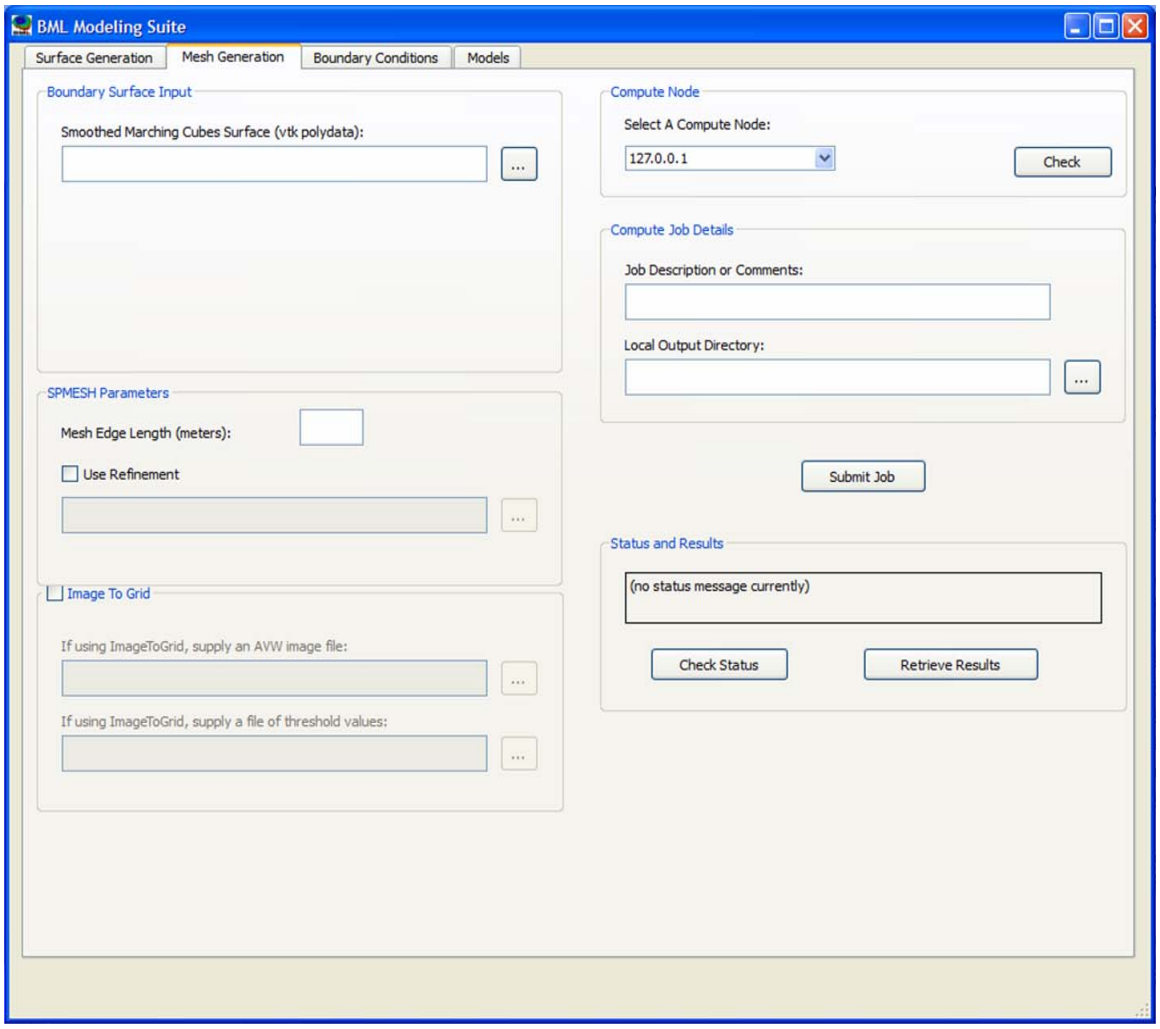


Figure 37. Mesh generation interface.

Boundary condition assignment

Boundary conditions are assigned through the use of a Visualization Toolkit (VTK) integrated window in the boundary condition tab of the client application in which the user loads the FE mesh and interactively selects a subset of boundary nodes on the model by 'painting' nodes on the surface of the mesh with the mouse and assigns the boundary condition type (displacement or stress free), coordinate (normal/tangential or

Cartesian), and value. To add points to the selection, the user selects 'Add' then paints the nodes on the surface to highlight. There is additionally an option to delete selected nodes. When selection is finished, the user assigns the desired boundary condition values as either displacement or stress-free. After selection and assignment, the user applies the boundary condition and is able to select different subsets of boundary nodes for additional boundary condition assignments. When finished with all boundary condition assignments, the boundary condition file is saved locally on the off-site client without the need for submission to the on-site server. A screenshot of this tab is seen in Figure 38. For additional information on the selection and application of boundary conditions in inverse FE modeling of fracture calluses, see [61].

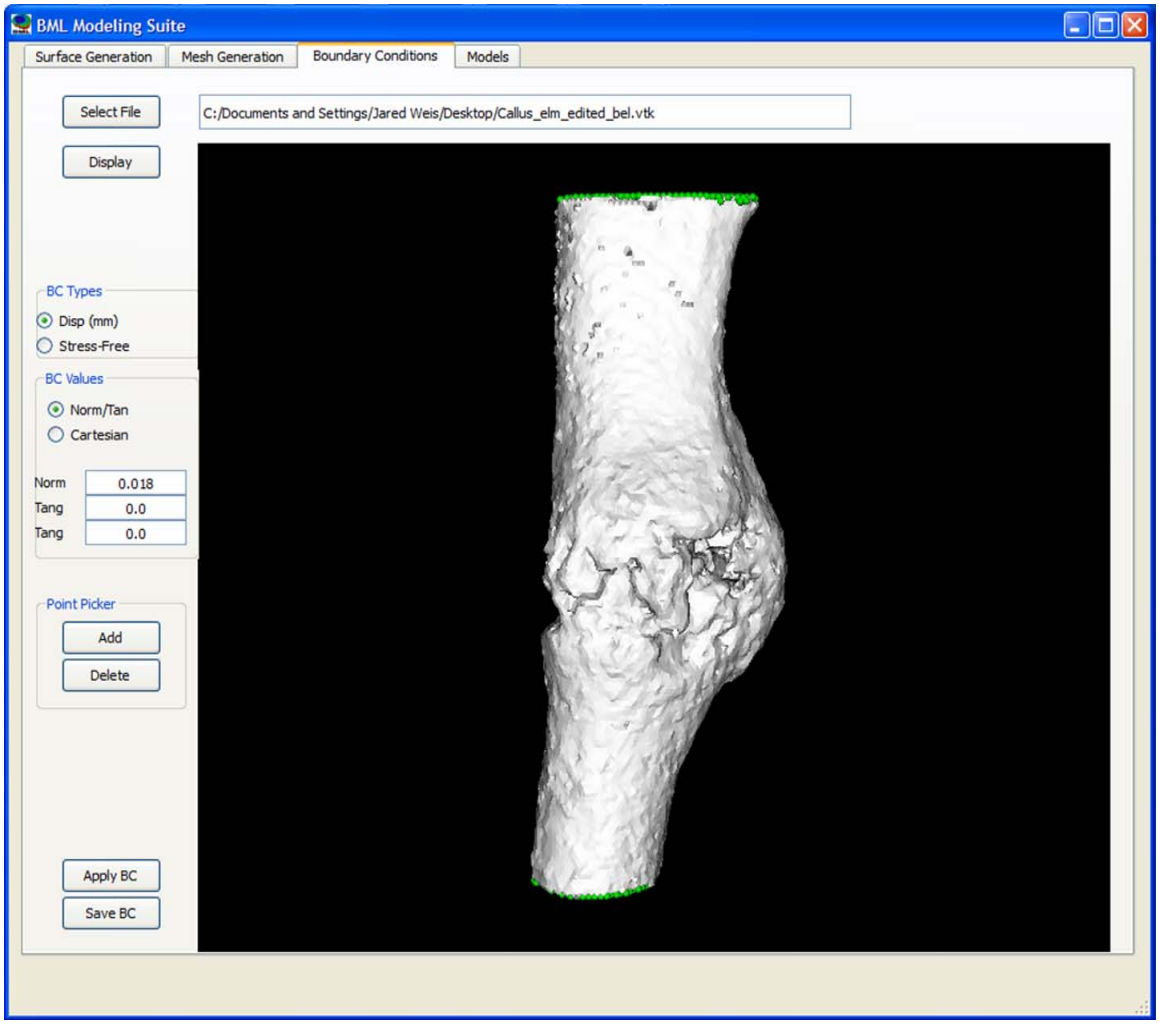


Figure 38. Boundary condition generation interface

Model submission

Following surface, mesh, and boundary condition creation, the inverse FE model is ready for submission and solving in the model tab. The mesh and boundary conditions created during the previous steps are submitted along with additional optional model parameters (such as body force file, gravity vector, and fluid file) and additional inverse model parameters (such as experimental force file, property ID number that is being

optimized, and an initial guess of the property). The optional model parameters of body force file, gravity vector, and fluid file are not used in the current bone fracture callus inverse model, however these parameters are included as optional arguments within the pipeline for general adaptation. The experimental force file is the experimental biomechanical testing data to which the model optimizes towards. Upon submission and completion of the analysis on the on-site server, the optimized property value is returned as a solution to the off-site client. A screenshot of the model submission tab in the client application is seen in Figure 39. For additional details on the inverse FE model, see [61].

Processing of bone fracture callus data

As a trial analysis of the submission system pipeline, example bone fracture calluses (n=3 samples) were processed through the semi-automatic pipeline. Client processing times and the created mesh domain sizes were recorded for all samples. Average processing times +/- standard deviations are reported for all client interactive tabs. The client processing time (which includes AVW image file and marching cubes, decimation, and RBF parameter option selections) for surface generation was recorded on average as 33.93 +/- 2.50 seconds. Client processing time for mesh generation was recorded as 36.10 +/- 1.75 seconds, which resulted in an average domain size of 114747 +/- 26238 nodes and 633868 +/- 147917 elements. Client processing time for boundary condition selection and assignment was recorded as 217.87 +/- 20.98 seconds. Finally, client processing time for initiating the inverse FE model optimization was recorded as 36.82 +/- 1.63 seconds. Server processing times (data not shown) were highly variable

based upon domain size, but were on the order or 30 minutes each for surface and mesh generation and 60 minutes for inverse FE model optimization.

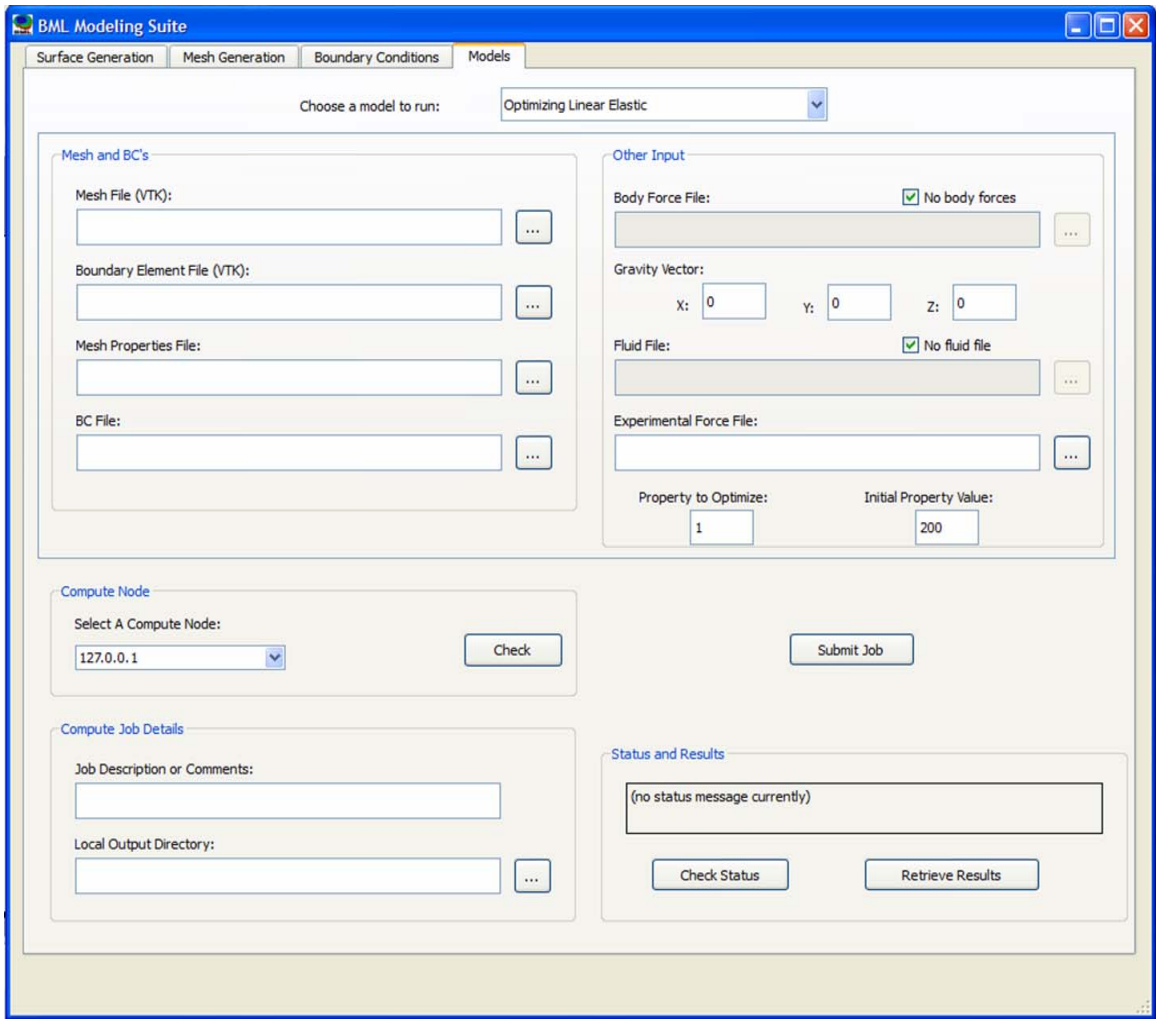


Figure 39. Model submission interface.

## Discussion

In this study we have developed a dual-node approach for generating an online resource for investigators for the functional inverse FE analysis of fracture healing callus. This dual-node client/server framework is generated such that interaction for the client only represents the collection and preparation of data for transmission rather than execution of the analysis locally. The process of generating inverse FE model-assisted analysis is broken down into discreet steps which require minimal interaction from the user. In each step, the data is submitted to the server for analysis and results are retrieved from the server when processing is completed. Processing is performed automatically and transparently to the user. Following completion of all of the steps, the user is presented with the reconstructed fracture callus tissue elastic modulus, which represents a biomarker of bone fracture healing.

As an alternative to a web-based submission system, the inverse analysis methods developed previously could also be packaged and distributed for specific analysis. However, as the needs of collaborators change, it often then requires an expert in numerical analysis to "re-tune" the analysis for the new application. Additionally, as refinement of the analysis methodology occurs in a package distribution system design, those changes are slowly integrated, whereas changes can be deployed quickly with minimal user interaction in the submission system design. As a result, we have taken the approach of generating an online resource for investigators whereby minimal understanding of numerical analysis would be needed by collaborators and changes to the analysis could be rapidly addressed by the experts who created it. In some respect, this represents a refinement of the shared compute facility approach by adding an interface

level such that the nuances of compute platforms, library construction, compilation issues, and ‘tuning’ are avoided by the end-user. Furthermore, a client/server framework is generated such that interaction for the client only represents the collection and preparation of data for transmission rather than executing the analysis locally.

# CHAPTER VII

# FUTURE DIRECTIONS AND CONCLUSIONS

This chapter contains initial contributions and comments towards fundamental advancements that can be applied to the current analysis work. These developments are intended to be preliminary but yet comprehensive in that they cover all core aspects of the analysis methodology. The proposed advancements can be separated into four key components of the current analysis pipeline: analysis developments, computational platform developments, experimental design developments, and experimental system developments. Example developments and preliminary data are presented for each key aspect, as well as a discussion of the impact upon the analysis methodology. Additionally, a summary of all of the studies contained within the work and a reflection upon the impact of this work is included.

## Analysis Developments

The studies presented herein have raised several aspects of the analysis methodology that deserve further consideration as avenues of future work. The inverse FE analysis procedure was developed as a generic and adaptable method, in that the FE model can be adjusted to suit differing investigator needs or advances in computational modeling capability. Therefore, a logical next step in regards to the accuracy and applicability of the analysis model and the resultant mechanical property reconstruction would be to increase the level of sophistication of the FE model. The current inverse

analysis procedure relies upon the assumption of an isotropic linear elastic material constitutive law. Although a geometrically nonlinear framework was explored in Chapter V through a 'moving mesh' technique, the fundamental assumption of isotropic linear elasticity remains. As such, this remains a potential direction for refinement in the current analysis methodology due to the fact that neither bone nor cartilage (the two major components of callus tissue) exhibit true material linear elasticity. An assumption of linear elasticity was used as an initial approximation during the development and validation stages of the inverse FE model; however now that that the methodology has demonstrated sensitivity and effectiveness, challenging this assumption would be prudent. One such material model that would make an appropriate choice is that of hyperelasticity. Hyperelastic materials are ones which exhibit very large elastic deformation in response to loading and are generally incompressible or nearly-incompressible. Hyperelastic material models were originally developed to describe rubber-like materials [98, 99] however many biological tissues, including cartilage, fall into this category. Widely used hyperelastic material models include Neo-Hookean, Mooney-Rivlin, Arruda-Boyce, and Ogden materials, with Neo-Hookean and Mooney-Rivlin models being the most predominant ones within the biological tissue field. The Mooney-Rivlin strain energy density potential is given by:

$$W = C_1(\bar{I}_1 - 3) + C_2(\bar{I}_2 - 3) + D_1(J - 1)^2$$

Where $C_1$ and $C_2$ are empirical material constants and $\bar{I}_1$ and $\bar{I}_2$ represent the first and second deviatoric strain invariants, respectively. For the case of incompressibility, $D_1 = 0$ and $J = 0$.

The Neo-Hookean strain energy potential is given by:

$$W = C_1(\bar{I}_1 - 3) + D_1(J - 1)^2$$

Through comparison to the Mooney-Rivlin model, this model can be seen as a special case of the Mooney-Rivlin model where $C_2 = 0$. Again, $D_1 = 0$ and $J = 0$ for the case of incompressibility.

In these models, the deviatoric strain invariants $\bar{I}_1$ and $\bar{I}_2$ are:

$$\bar{I}_1 = Tr(\bar{\boldsymbol{F}}\bar{\boldsymbol{F}}^T)$$
$$\bar{I}_2 = \frac{1}{2}\bar{I}_1^2 - Tr[(\bar{\boldsymbol{F}}\bar{\boldsymbol{F}}^T)(\bar{\boldsymbol{F}}\bar{\boldsymbol{F}}^T)]$$

where

$$\bar{\boldsymbol{F}} = J^{-1/3}\boldsymbol{F}\ ,\ J = \lambda_1\lambda_2\lambda_3$$

and

$$\boldsymbol{F} = \begin{pmatrix} \lambda_1 & 0 & 0 \\ 0 & \lambda_2 & 0 \\ 0 & 0 & \lambda_3 \end{pmatrix}$$

Substitution yields

$$\bar{I}_1 = J^{-2/3}(\lambda_1^2 + \lambda_2^2 + \lambda_3^2)$$
$$\bar{I}_2 = J^{-4/3}(\lambda_1^2\lambda_2^2 + \lambda_2^2\lambda_3^2 + \lambda_3^2\lambda_1^2)$$

with J as the volume ratio and $\lambda_i$ as the stretch ratio in each of the principal directions.

As an example of the difference between hyperelastic (Neo-Hookean and Mooney-Rivlin) and linear elastic material models, consider the case of uniaxial deformation of a nearly-incompressible material. For uniaxial extension of an incompressible material, $\lambda_1 = \lambda,\ \lambda_2 = \lambda_3 = 1/\sqrt{\lambda}$ and $J = 1$. Therefore $I_1$ and $I_2$ can be rewritten:

$$\bar{I}_1 = \lambda^2 + \frac{2}{\lambda}$$
$$\bar{I}_2 = 2\lambda + \frac{1}{\lambda^2}$$

Stress can be expressed as:

$$\boldsymbol{S} = \frac{\partial W}{\partial \boldsymbol{E}} = 2\frac{\partial W}{\partial \boldsymbol{C}}$$

where **S** is the second Piola-Kirchoff stress tensor, **E** is the Green strain tensor and **C** is

the right Cauchy-Green deformation tensor.

The engineering stress tensor in the Mooney-Rivlin model can therefore be written as:

$$\sigma_{eng} = 2C_1\left(\lambda - \frac{1}{\lambda^2}\right) + 2C_2\left(1 - \frac{1}{\lambda^3}\right)$$

and the Cauchy stress as:

$$\sigma_{Cauchy} = 2C_1\left(\lambda^2 - \frac{1}{\lambda}\right) + 2C_2\left(\lambda - \frac{1}{\lambda^2}\right)$$

In the Neo-Hookean model, the engineering stress is:

$$\sigma_{eng} = 2C_1\left(\lambda - \frac{1}{\lambda^2}\right)$$

and the Cauchy stress is:

$$\sigma_{Cauchy} = 2C_1\left(\lambda^2 - \frac{1}{\lambda}\right)$$

For small strains, as $\lambda \to 1$, the initial Young's modulus (E) can be determined by taking the partial derivative of the Mooney-Rivlin stress with respect to stretch:

$$E = \lim_{\lambda \to 1} \frac{\partial \sigma}{\partial \lambda} = 6(C_1 + C_2)$$

Therefore the initial shear modulus in a nearly-incompressible material is given by:

$$G = \frac{E}{2(1+\nu)} = 2(C_1 + C_2)$$

where ν is Poisson's ratio, equal to 0.5 for the case of incompressibility.

A plot comparing the force versus displacement behavior of the two hyperelastic models discussed with a linear elastic model of an example bone fracture callus is shown in Figure 40A. In this figure, Mooney-Rivlin constants were selected for the callus material by setting $C_2$ equal to 0.25*$C_1$ and the determining the constants through the above linear elastic-to-hyperelastic transformation equation where the Young's modulus is equal to 1888.12 kPa (taken from optimization). The callus material was assumed to be hyperelastic and nearly-incompressible. $C_1$ was set as 251.75 kPa, $C_2$ was set as 62.94 kPa, and the cortical bone material was left as linear elastic. As observed in this figure, there are major fundamental differences between the force versus displacement behavior

of the linear elastic model and the hyperelastic models, whereas the two hyperelastic models behave similarly. As the biomechanical testing data of this same sample (shown in Figure 40B) exhibits significant nonlinearity with a similar trend, we would expect that these hyperelastic models would more closely replicate the true biomechanical testing data upon final optimization which determines the $C_1$ and $C_2$ parameters. This would lead to a more accurate and diagnostic functional fracture healing material property biomarker that is based on a more biologically relevant material model. Therefore this analysis development represents a potentially important avenue of future work in order to reduce the computational-to-experimental model fitting error and generate more accurate and relevant results.

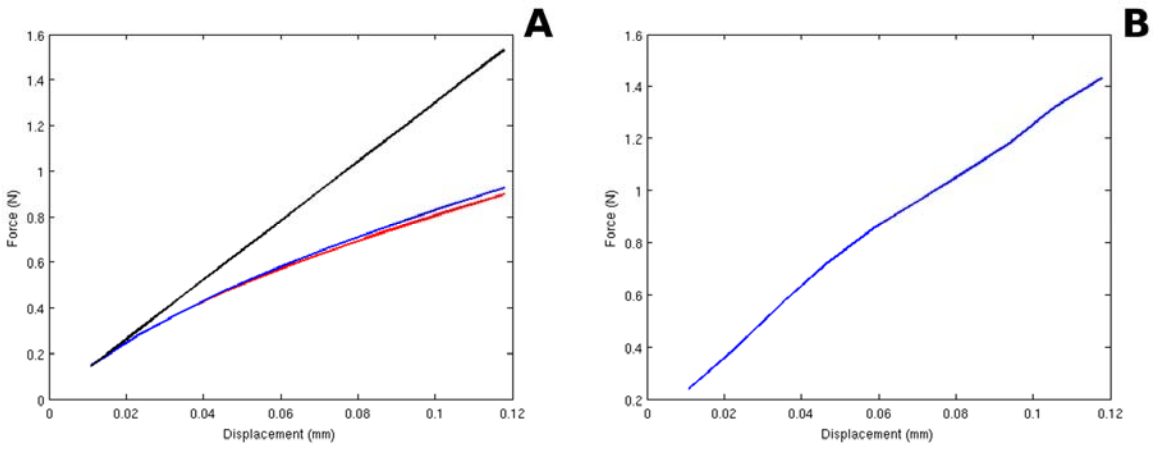


Figure 40. Force versus displacement curves for (A) callus hyperelastic and linear elastic material FEA model comparisons, and (B) experimental biomechanical testing of the same sample. In (A), the black, blue, and red lines are linear elastic, Mooney-Rivlin, and Neo-Hookean models, respectively. The hyperelastic constants were selected from the derived linear elastic-hyperelastic transform equation shown above. C2=.25*C1 for the Mooney-Rivlin model.

## Computational Platform Developments

As hyperelastic material models are inherently more computationally sophisticated than the linear elastic model that is contained within the current inverse FE framework, the addition of a hyperelastic model to the in-house custom-built suite of FE material models will incur significant software development effort that necessitates advancement to the computational platform. The addition of hyperelastic modeling capability to the in-house custom-built FE software package would require a complete re-write of the core FE software package, incurring a large development effort. One strategy to eliminate the dependency of potential new core FE models (hyperelastic or otherwise) upon programmatic time and effort is with the integration of commercially available FE modeling packages within the analysis pipeline. In this way, multiple additional complex models can be implemented without incurring excessive programmatic development cost. These additional commercial models can be 'plugged-in' to the forward model section of the inverse pipeline (see Chapter 2, Figure 8) and as such are treated modularly to obtain a different model calculated force ($F_{calc}$) from that calculated by the current in-house developed linear elastic model. However, the integration of commercial FE software within the context of an in-house custom-built software pipeline does not come without its own caveats, such as difficulties with input/output file format conversions, issues dealing with the execution the commercial solver from within the software pipeline, and inconsistencies between similar computationally derived values. Commercially available FE software is primarily intended to be used as an 'all-in-one' forward modeling package, in which the model is built, boundary conditions are assigned, and the displacement/force solution is calculated

from within an all-encompassing graphical user interface (GUI). While user friendly, this practice is not conducive to an inverse FE methodology. However, commercial FE software does often leave the core model solver exposed for processing models written from outside the typical GUI. Therefore we can leverage this solver to execute the complex forward model by appropriately converting to and from the commercial FE software input and output file formats through the addition of custom-built file format converters to the inverse pipeline. Significant development has already been made towards this goal utilizing MSC.Nastran and MSC.Marc as the commercial FE solvers and preliminary data is given below.

Validation of the incorporation of a commercial FE package within the inverse procedure is shown in Table 12. From this table, we see that the inverse FE calculated Young's modulus values from the original methodology utilizing in-house developed FE software (PETSc-based) yields similar results (< ~5% difference) as the equivalent modulus values calculated from the inverse procedure utilizing the commercial solver for a linear elastic model. Therefore we can conclude that the incorporation of this solver does not materially affect the modulus reconstruction procedure. However it is interesting to note that a difference, while small, does exist between the reconstructed Young's moduli in what are essentially the exact same FE models. This is due to the fact that subtle differences exist between the model calculated forces from the in-house developed FE code as compared to the commercial FE code, due to differences between the methods used to reconstruct the respective surface force values. Thus, the integration of commercial FE packages provides distinct advantages for the solution of complex material models, however it comes with the caveat that different numerical methods can

be used to calculate similar quantities and thus calculation variability can occur. The next step in this development is to utilize the Neo-Hookean and Mooney-Rivlin hyperelastic material models as the forward FE model within the inverse FE procedure to determine hyperelastic material constants of bone fracture callus through optimization.

Table 12. Comparison of the inverse FE reconstructed modulus for both the original (custom-built in-house model) and the MSC.Nastran linear elastic models at 14 and 21 days post-fracture.

| | $E_{mean,\ PETSc}$ | $E_{mean,Nastran}$ | % difference |
|---|---|---|---|
| 14d NC | 2296.45 ± 715.56 | 2174.59 ± 1159.08 | 5.31 |
| 21d NC | 3842.02 ± 1686.89 | 3656.49 ± 560.28 | 4.83 |

## Experimental Design Developments

Separate from the computational analysis (software) developments discussed above are experimental design (hardware) developments. The inverse analysis procedure was developed to be adaptable to changes in the experimental design, including changes in the biomechanical testing regime. Researchers currently use several methods for assessing the biomechanical properties of bone fracture callus, including tension, torsion, and 3-point bending biomechanical testing. The procedure described within this work utilizes a tensile displacement ramp to failure at 0.25 mm/min. This low strain rate loading regimen is selected to negate the effects of any time dependant viscoelasticity terms; and tension is selected for computational ease in the FE model. By selecting tensile loading, the boundary condition assignment for the FE model becomes trivial: the

top surface is prescribed a ramp displacement similar to the BMT, and the bottom surface is fixed. However, in nature the most common mode of bone failure is through bending, and it is unusual for a bone to experience a pure tension loading environment. Therefore an advancement to the current callus inverse FE analysis experimental design is to modify the experimental design by changing the biomechanical testing regimen to include a more physiologically relevant loading pattern, such as bending. But the selection of the most common form of bending BMT (3-point bending) comes with challenges. In 3-point bending testing of fracture callus, the two upright supports are placed in contact with the bone ends on either side of the callus with the downward 'indenter' located in the middle of the callus. In this scenario for the case of early-stage healing where there is a soft callus, the indenter compressively deforms the callus material directly without deflecting the entire beam, further complicating the loading pattern and the computational model. To avoid this complication while retaining the physiologically relevant bending analysis system, we have developed a cantilever bending fixture for the analysis of bone fracture callus. The fixture setup is shown in Figure 41 and sequential images taken during an example mechanical test are shown in Figure 42. In this setup, one of the bone ends of the sample is potted upright in PMMA in a disposable plastic tube. After polymerization, this tube is loaded into the fixture and secured. The fixture is then brought into cantilevered contact with the indenter prior to the mechanical test, with the indenter applying force to the bone end on the opposite side of the callus as the fixture. The mechanical test is performed by displacing the indenter downward, which deflects the bone. As the callus is the weakest part of the bone sample, failure will predictable occur within the callus region.

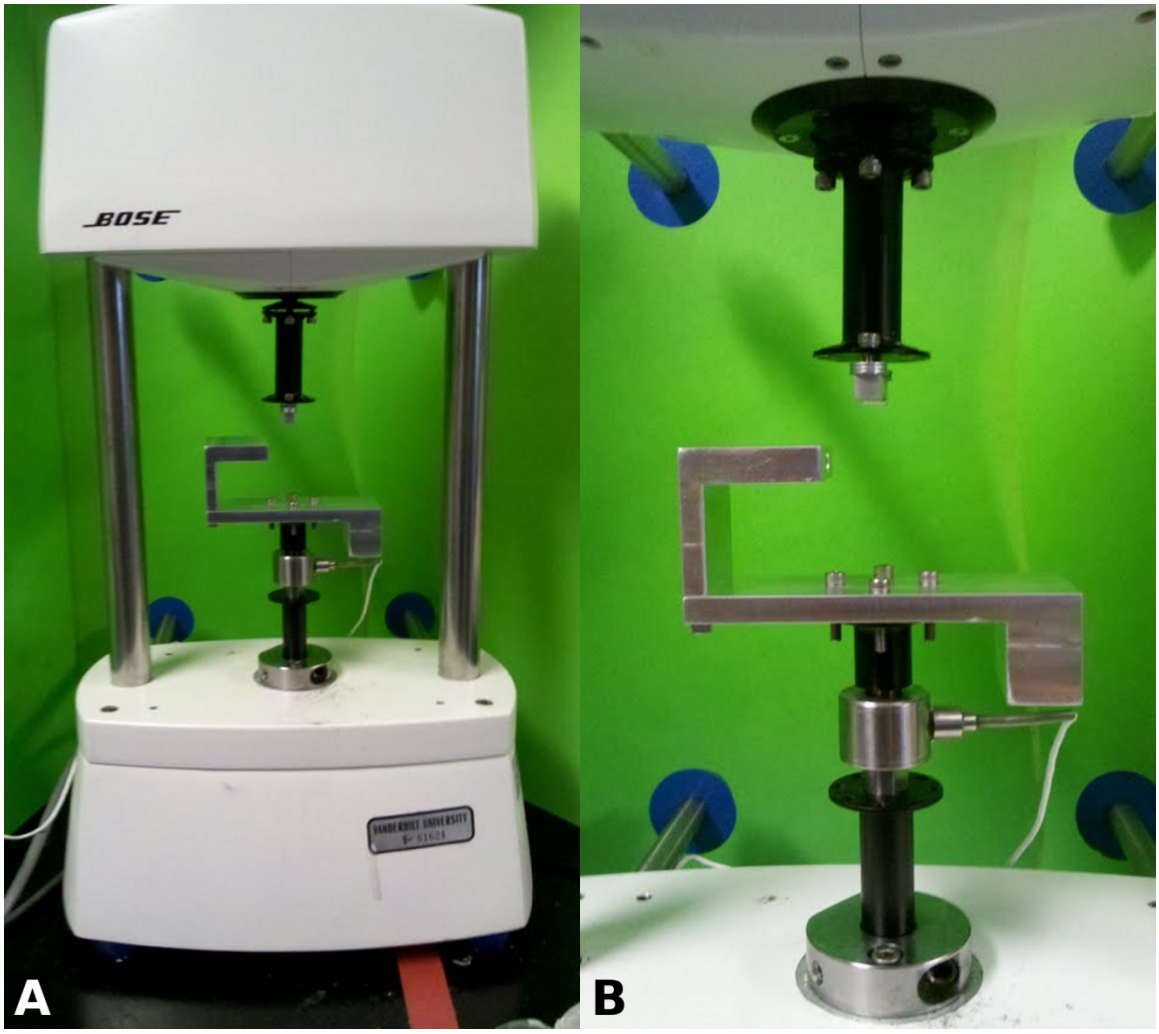


Figure 41. Cantilever bending biomechanical testing fixture.

However, care must be taken regarding identification of orientation when loading the bone sample into the fixture due to the complications associated with modeling the bending deformation. In bending analysis of bone fracture callus the model boundary condition assignment becomes complex and depends upon the orientation of the bone within the material testing fixture. The bone fracture callus is highly irregular and

inhomogeneous and thus the stress/strain behavior is different for each orientation. Proper and accurate inverse FE property reconstruction requires that the simulated and experimental orientations be the same, and therefore the orientation of the bone within the BMT fixture must be notated for post hoc FE modeling. This is an additional difficulty and added step within the analysis pipeline. One hypothesis to confirm correct orientation is through the use of an image registration procedure between the microCT scan and a 2-dimensional image acquired prior to mechanical testing. Prior to FE analysis, this registration can be performed such that the external surface of the microCT scanned image volume is rotated to match that of the 2-D image taken prior to BMT. As the bone fracture callus is highly irregular, the external surface should provide enough unique identifiable information such that an optimum registration is possible. An example of such a 2-D image is shown in Figure 42A, which is taken from video capture of the cantilever BMT. Future research should be directed at validation of this orientation registration hypothesis and the applicability of cantilever BMT analysis in the inverse methodology.

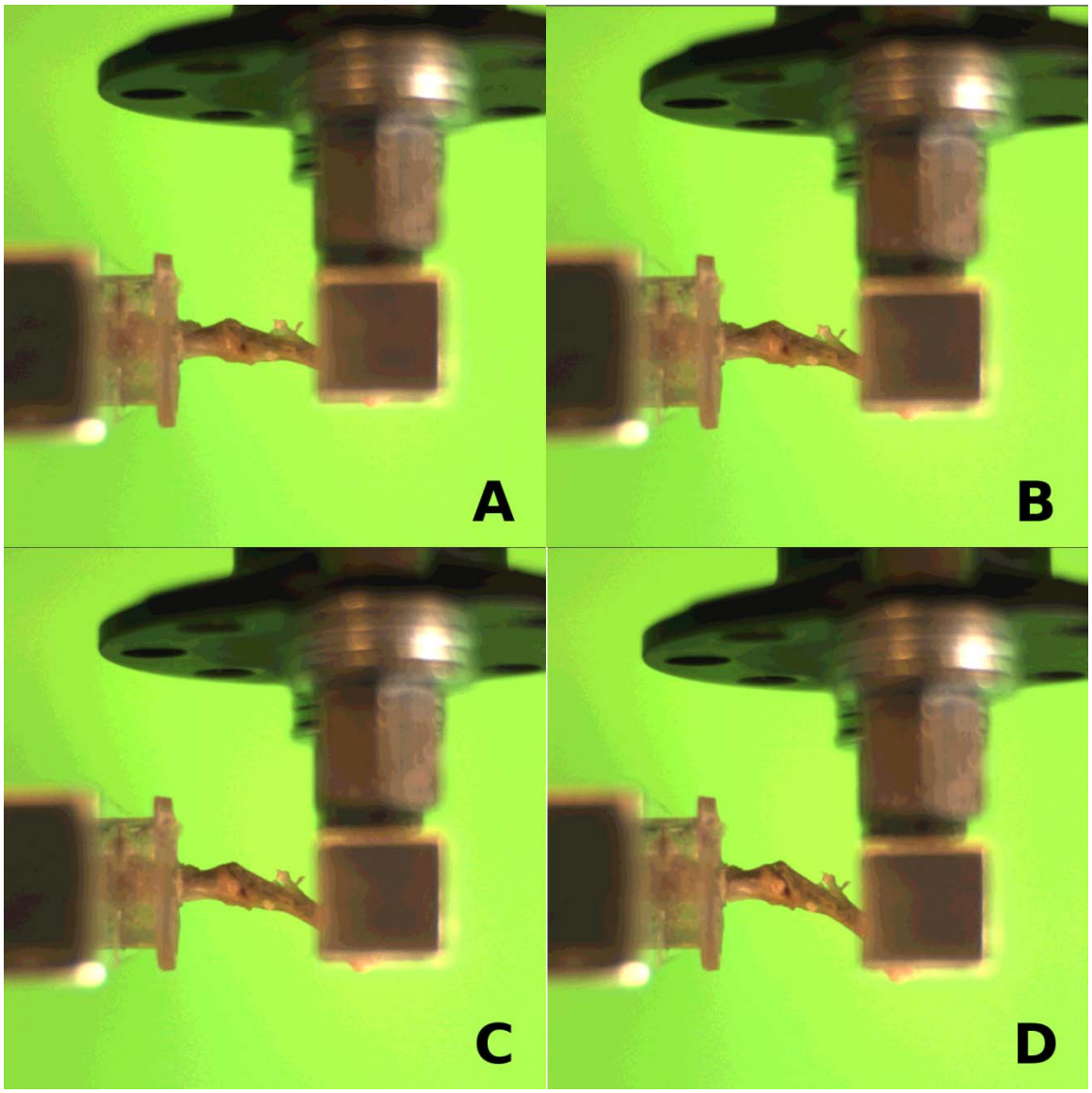


Figure 42. Sequential images taken from video capture of a cantilever bending test of a bone fracture callus.

## Experimental System Developments

The studies on fracture healing in both the literature and within this document have largely been dependent on wild-type rodent fracture healing models. Recently, several rodent models of pathological fracture healing have been developed. Therefore,

an intriguing future direction is to extend the inverse FE material property reconstruction methods towards experimental system developments, such as evaluation of animal models of pathological fracture healing. One such model is the *Bmp2*$^{c/c}$; *Prx1::cre* mouse model (Figure 43) [7, 100]. It is a transgenic mouse that has *Bmp2* inactivated in limb tissue-specific manner (*Prx1::cre* enhancer). Briefly, mice with a floxed *Bmp2* allele (*Bmp*$^{c/c}$ mice) are bred to *Prx1::cre* mice to obtain *Bmp2*$^{c/c}$; *Prx1::cre* mice (homozygous limb-specific conditional knockout mice), *Bmp2*$^{wt/c}$; *Prx1::cre* mice (heterozygous limb-specific conditional knockout mice), and control mice (no Cre recombinase expression). BMP2 is a secreted signaling molecule in the transforming growth factor-beta superfamily that has been implicated in embryonic skeletogenesis, postnatal bone maintenance, and fracture healing [101]. In fractures, BMP2 is thought to regulate the progression from osteoprogenitor to osteocyte, among other functions, and has been previously shown to be especially important in fracture repair as a necessary initiator of the osteogenic fracture healing cascade [7]. In rodents, stimulation with exogenous BMP2 was found to stimulate endochondral ossification through regulation of periosteal chondrogenesis [102], while fracture calluses from rodents deficient in BMP2 exhibit fracture nonunion with severely limited periosteal activation [7]. In addition, in human fractures, BMP2 was found to be significantly reduced in the cartilaginous callus from patients with fractures that progressed towards nonunion, as compared to patients with healing fractures [74]. Previous studies in mice have shown that global BMP2 knockout exhibits embryonic lethality [103], but the *Bmp2*c/c; *Prx1::cre* limb-specific knockout mouse exhibits few skeletal abnormalities at birth [7]. However, this mouse model exhibits impaired skeletal function (through bone fragility) that manifests in spontaneous

forearm fractures by 13 weeks of age. The mouse is able to avoid spontaneous fractures until it gets larger and more mobile, increasing the risk of fracture. The heterozygous *Bmp2*c/wt; *Prx1::cre* mouse, however, avoids the risk of spontaneous fractures while also exhibiting an impaired fracture healing phenotype. Thus this mouse makes an ideal candidate for the study of impaired healing without the complications of spontaneous, uncontrolled fractures.

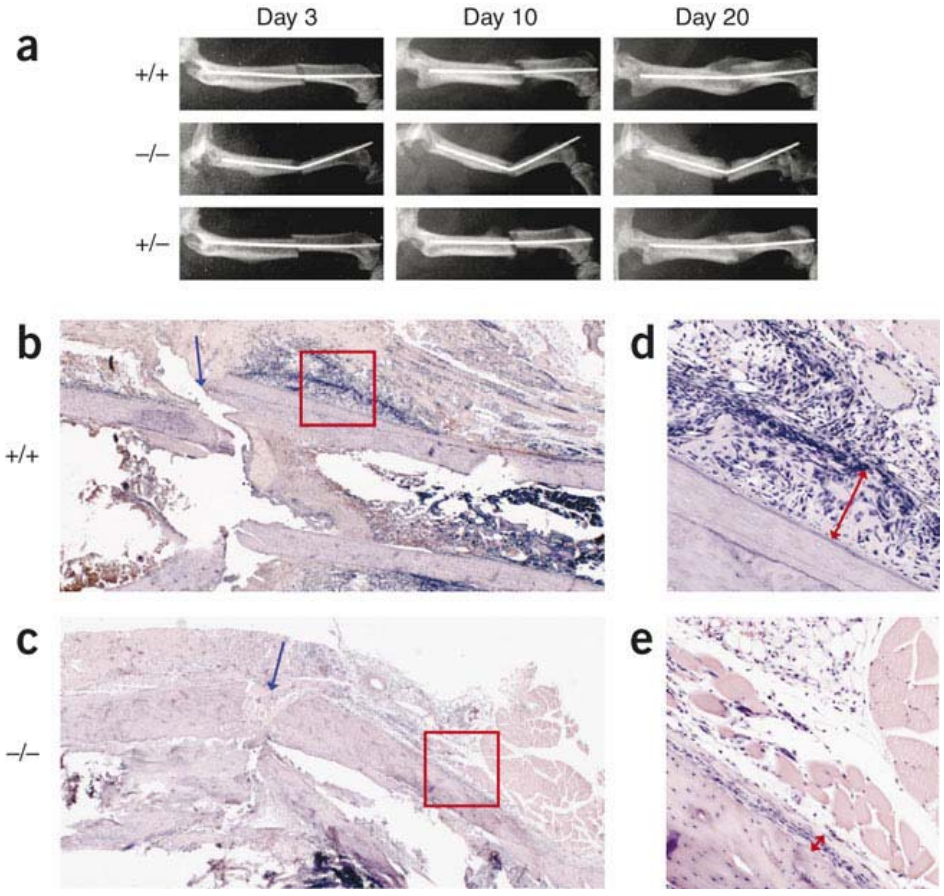


Figure 43. Loss of BMP2 leads to impaired fracture healing. (a) Longitudinal x-ray images from wild-type (+/+), *Bmp2*$^{wt/c}$; *Prx1::cre* (+/-), and *Bmp2*$^{c/c}$; *Prx1::cre* (-/-) mice show impaired healing and lack of healing in +/- and -/-, respectively. Wild-type (b,d) and *Bmp2*$^{c/c}$; *Prx1::cre* (c,e) histological images show lack of periosteal activation in the BMP2 knockout. Adapted from [7].

Preliminary results regarding the application of the inverse FE analysis method as well as several other traditional fracture healing metrics within this pathological fracture healing system are shown in Figure 44 and Table 13. Limb specific heterozygous BMP2 mice (n=6) as well as control mice (littermates that do not express Cre recombinase, n=4) were subjected to experimental tibia fracture and evenly divided into groups that were allowed to heal for either 14 or 21 days. Due to the low sample numbers in this preliminary analysis, no significant differences we observed at either time-point when comparing control mice to heterozygous BMP2 mice. However upon observation of the inverse FE analysis material property and BMT-derived stiffness metrics, a trend of decreasing mechanical competence was observed for BMP2 heterozygous mice at 14 days post-fracture as compared to control mice. This trend disappeared as the time of healing progressed to 21 days. While not statistically significant (due to low sample number and an inherently noisy genetic system), this observation would seem to fit within the logic of the experimental system. Knocking-down BMP2 (an initiator of fracture healing) in the heterozygous mouse would thus have a greater impact upon the mechanical competence of the early-stage callus. As healing progresses to later-stages, the reduction in BMP2 would have less of an impact on the progression of fracture healing. It is also important to note that none of the microCT imaging metrics show a similar trend, giving further support to the insufficiency of imaging alone as a surrogate functional measure, as elaborated upon in Chapters 3 and 4. In summary, these preliminary data reflect important trends and thus additional study is necessary to further elucidate the mechanical competence of fracture calluses from this genetic model as well as the effectiveness of the inverse FE analysis procedure within this experimental

challenge. Additionally, the application and inverse FE assessment of therapeutic MSC transplantation (as discussed in Chapter 4) in the BMP2 knock-down system as an attempt to ameliorate the impaired healing would be an intriguing future direction.

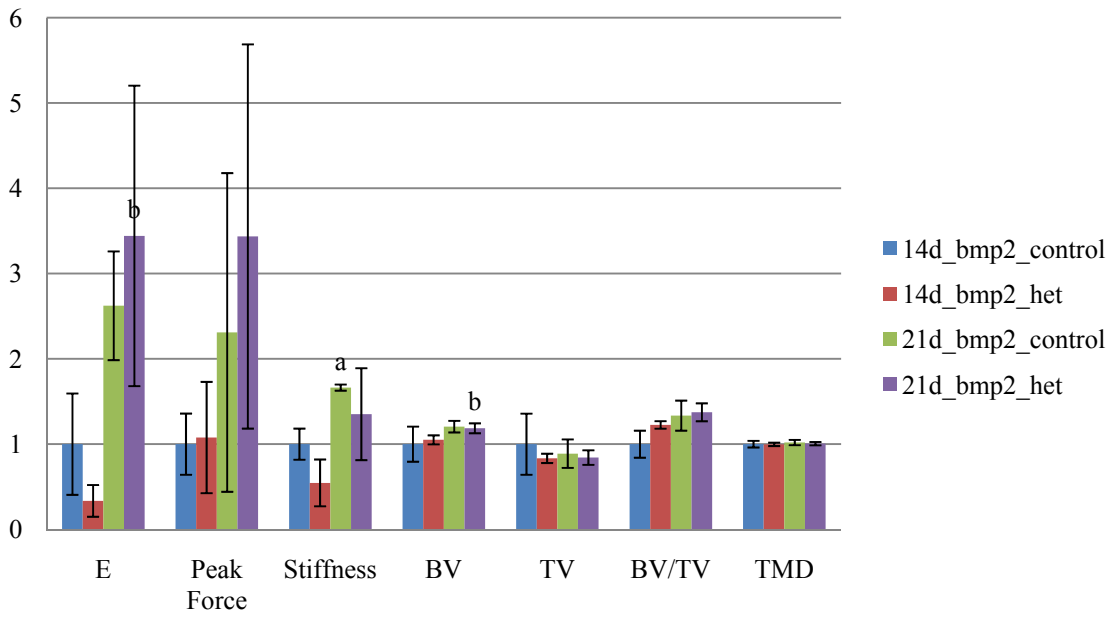


Figure 44. Plot of fracture healing metrics for BMP2 knockout model. [a], $p < 0.05$ vs. 14d BMP2+/+. [b], $p < 0.05$ vs. 14d BMP2 +/-. N=2 for both 14d and 21d BMP2 +/+ and N=3 for both 14d and 21d BMP2 +/-.

Table 13. Fracture healing metrics for BMP2 knockout model. [a], $p < 0.05$ vs. 14d BMP2+/+. [b], $p < 0.05$ vs. 14d BMP2 +/-. n = 2 for both 14d and 21d BMP2 +/+ and n = 3 for both 14d and 21d BMP2 +/-.

| | **14d BMP2 +/+** | **14d BMP2 +/-** | **21d BMP2 +/+** | **21d BMP2 +/-** |
|---|---|---|---|---|
| **E** | 18842.40 ± 11203.34 | 6312.49 ± 3516.03 | 49424.01 ± 12013.19 | 64859.13 ± 33199.74[b] |
| **Peak Force** | 2.60 ± 0.93 | 2.80 ± 1.70 | 6.00 ± 4.86 | 8.93 ± 5.86 |
| **Stiffness** | 83.93 ± 15.31 | 45.82 ± 23.02 | 139.61 ± 3.06[a] | 113.47 ± 45.26 |
| **BV** | 7.31 ± 1.50 | 7.68 ± 0.39 | 8.81 ± 0.50 | 8.67 ± 0.43[b] |
| **TV** | 15.60 ± 5.59 | 13.01 ± 0.85 | 13.87 ± 2.61 | 13.15 ± 1.33 |
| **BV/TV** | 0.48 ± 0.08 | 0.59 ± 0.02 | 0.64 ± 0.08 | 0.66 ± 0.05 |
| **TMD** | 120.69 ± 4.66 | 120.42 ± 2.35 | 123.02 ± 3.77 | 121.46 ± 2.39 |

## Summary

The work described herein is a collection of related studies in which bone fracture callus has been assessed in animal models of bone fracture healing through the use of an inverse FE methodology. The inverse analysis methodology serves as an enhanced functional healing analysis metric in which imaging data and biomechanical testing data are used jointly to determine mechanical properties of healing fracture callus tissue. Within this work, this method had been validated through the use of simulation studies

and has been shown to provide an enhanced level of discriminatory analysis ability over that of traditional microCT imaging and biomechanical testing alone in a study comparing normal fracture healing in mice at 10 versus 14 days post-fracture. Additionally, in a study comparing fracture healing in mice either receiving or not receiving therapeutic MSC transplantation at 14 and 21 days post-fracture, this method was proven to provide a level of discriminatory ability capable of statistically differentiating between all important experimental groupings across time and MSC treatment. Similarly to the previous study, other traditional fracture healing assessment metrics (both imaging and biomechanical testing derived) failed to provide a similar level of discriminatory capability as the inverse FE method, showing the enhanced ability of the inverse method over traditional metrics in functional mechanical analysis. Combined with the additional study detailing the specifics of the MSC therapeutic system, this data shows that in response to a fracture cue, MSC are recruited to the fracture site, engraft, and contribute to beneficially effect the progress of fracture healing and accelerate the regain in mechanical integrity/stiffness of the healing callus tissue allowing the callus to deform less in response to a given load. Additionally, modifications to the inverse analysis procedure were explored in which multiple elastic mechanical properties (Lame' constants) were assessed utilizing a geometrically nonlinear 'moving mesh' approach. This study shows that with a unique dataset derived from a geometrically nonlinear approach, additional mechanical parameters can be derived from the same data. Finally, a web-based submission system was developed in which the inverse analysis can be executed with a minimum dataset and minimal user interaction/computational knowledge. In this way, the submission system can facilitate the general adaptation of

computationally complex analysis tools whereby a naive user can generate the inverse FE analysis without prior knowledge of computational systems.

The utility of the inverse analysis methodology presented within this work is in the enhanced functional assessment of fracture callus tissue. Upon the initiation of this work, the overall hypothesis was that inverse FE techniques could be applied to the assessment of bone fracture healing in order to generate a more sensitive biomarker for the evaluation of healing. Through utilizing multiple modes of bone fracture callus experimental data (microCT imaging and biomechanical testing), the analysis techniques developed within this work have been shown to provide a unique view of the healing callus tissue-level mechanical properties that is unattainable through other current analysis techniques. This assessment provides a more clear analysis metric capable of discriminating differences between groups of fracture calluses and thus confirms the initial hypothesis. Looking towards the future of this analysis methodology (after further research upon larger and more varied groups of data), I envision further validation and verification of the fidelity of this analysis methodology as well as a trend towards general acceptance and adaptation of inverse methods in the analysis of fracture healing. While this specific tool may not gain broad acceptance within the general fracture healing scientific community, the fact remains that inverse FE analysis techniques (both in general and specifically in fracture healing) have been shown to provide an enhanced level of analysis; and this work was the first to apply those techniques to the analysis of bone fracture healing data. The current standard of fracture healing assessment has been shown to be lacking, and therefore I propose a movement towards the general adaptation of more sensitive and multi-modal assessment methodologies (including the inverse FE

analysis presented within this work). I also recognize that this analysis does not come without its own drawbacks. Firstly, the technique is limited to destructive *ex vivo* analysis only, as destructive biomechanical testing is required within the pipeline. A reliable and accurate non-destructive assessment technique would be extremely valuable, however currently the only method to get the necessary biomechanical information for use in inverse analysis is through destructive *ex vivo* biomechanical testing. Additionally, the current gold standard for functional fracture healing assessment utilizes this same destructive biomechanical testing. As another critique, the analysis also currently lacks FE model sophistication. However the goal of this work was to generate a sensitive biomarker for functional fracture healing assessment, not to produce the most accurate multi-physics model of bone fracture callus possible. Additionally, the preliminary data contained within future work discussed above in the 'Analysis Developments' subsection begins to address this critique with a movement towards incorporation of more sophisticated and physiologically relevant hyperelastic material models.

# APPENDIX A

# REGENERATIVE EFFECTS OF TRANSPLANTED MESENCHYMAL STEM CELLS IN FRACTURE HEALING

## Introduction and Contribution of Study

This study demonstrates the specifics of the fracture healing animal model as well as details regarding the MSC transplantation system. This study shows that MSC, when transplanted into a mouse with an experimental fracture, migrate to the fracture site, engraft, contribute to the initiation of the reparative process, and modulate the inflammatory environment. The CXCR4-SDF1 axis was identified as having a primary role in the migration and targeting of MSC to the fracture site. Additionally, this study contained the first evidence that MSC were seen to enhance fracture healing by improving biomechanical and microCT-derived bone and cartilage volumetric parameters.

While I am not the primary author of this manuscript, as the second author my role in this study remained significant: perform the microCT imaging and analysis, perform the biomechanical testing and analysis, assist in performing the bioluminescence imaging and analysis, assist in generating the experimental fractures, assist in isolation and culture of mesenchymal stem cells, assist in histological preparation of bone tissue callus samples, assist in final analysis and study conclusions. Therefore I have included this manuscript as an appendix to aid in the understanding of the MSC transplantation animal model as well as mechanisms behind the effectiveness of MSC as a fracture healing therapeutic. This study was published in Stem Cells in 2009.

Appearing in:

Granero-Molto F, Weis JA, Miga MI, Landis B, Myers TJ, O'Rear L, Longobardi L, Jansen ED, Mortlock DP, Spagnoli A. Regenerative effects of transplanted mesenchymal stem cells in fracture healing. Stem Cells 2009; 27: 1887-98.


## Abstract

Mesenchymal stem cells (MSC) have a therapeutic potential in patients with fractures to reduce the time of healing and treat non-unions. The use of MSC to treat fractures is attractive as it would be implementing a reparative process that should be in place but occurs to be defective or protracted and MSC effects would be needed only for the repairing time that is relatively brief. However, an integrated approach to define the multiple regenerative contributions of MSC to the fracture repair process is necessary before clinical trials are initiated. In this study, using a stabilized tibia fracture mouse model, we determined the dynamic migration of transplanted MSC to the fracture site, their contributions to the repair process initiation and their role in modulating the injury-related inflammatory responses. Using MSC expressing luciferase, we determined by bioluminescence imaging that the MSC migration at the fracture site is time-and dose-dependent and, it is exclusively CXCR4-dependent. MSC improved the fracture healing affecting the callus biomechanical properties and such improvement correlated with an increase in cartilage and bone content, and changes in callus morphology as determined by microcomputed-tomography and histological studies. Transplanting CMV-Cre-R26R-LacZ-MSC, we found that MSC engrafted within the callus endosteal niche. Using MSC from *BMP-2-Lac-Z* mice genetically modified using a bacterial artificial chromosome

system to be β-gal reporters for BMP-2 expression, we found that MSC contributed to the callus initiation by expressing BMP-2. The knowledge of the multiple MSC regenerative abilities in fracture healing will allow to design novel MSC-based therapies to treat fractures.

## Introduction

High energy tibia fractures are threatening injuries with slow healing times averaging 43-49 weeks [104]. Furthermore, the fracture healing process is impaired in 10-20% of the fractures, resulting in non-unions and causing severe disabilities [4, 5, 105]. Non-unions are mostly treated with bone autografts that are associated with morbidities related to the harvesting procedure, have a limited supply and unpredictable repairing potential [77]. There is a compelling need to develop novel therapies to improve the fracture healing course and to treat non-unions. Mesenchymal stem cells (MSC) initiate the fracture repair process leading to the formation of a cartilaginous template (callus) that is then replaced by new bone that repairs the gap [2]. Limitation in MSC number and/or functions are hypothesized to play a critical in the pathogenesis of non-unions. MSC are present in several adult tissues including bone marrow (BM) and are capable of differentiating *in vitro* into mesenchyme cell types including chondrocytes and osteocytes while such differentiation has not been unequivocally shown *in vivo* [106]. Furthermore, both BM-MSC and BM mononuclear cells have been reported to exert beneficial effects in the healing of a limited number of patients with non-unions [107-112]. Although promising, these clinical studies are anecdotal. Before controlled clinical trials can begin, critical animal studies are necessary to determine how MSC are recruited

and survive at the fracture site, their repair effectiveness and the mechanisms through which they exert their actions.

Although MSC seem to migrate into damaged tissues, their dynamic trafficking and tissue homing when systemically infused is a poorly understood process [113-115]. *Post-mortem* microscopy is the standard method to detect transplanted MSC within the tissues; however, it does not allow to study either the cell trafficking or to perform longitudinal observations and it is not quantitative. Small-animal *in vivo* imaging bioluminescence (BLI) permits to determine a semi-quantitative temporal and spatial analysis and bio-distribution of the light signal of luciferase-tagged cells within a living animal. Among chemokines and their receptors, CXCR-4 has been found to be critical in hematopoietic stem cell homing and cancer cell metastasis [116]. The CXCR4 expression and contribution to MSC migration *in vitro* and its need in MSC homing *in vivo* have been scarcely evaluated [117, 118].

Several reports have shown that MSC delivered to an injured tissue can improve the recovery; however, a limited number of MSC have been demonstrated to differentiate into the repaired tissue [81, 119, 120]. This discrepancy might be explained by the fact that: 1) there are technical difficulties in identifying MSC within the repaired tissue; 2) studies have focused on the identification of MSC differentiation into cells involved in advanced stages of healing; 3) MSC mechanisms of action, other than differentiation, may have induced the regeneration. Anti-inflammatory paracrine effects of MSC have been reported in animal models of acute and chronic inflammatory diseases [121-124]. Most recently, MSC transplant in 55 patients with severe graft-versus-host disease has led to a complete response or improvement in 39 patients [125]. It is plausible that due to

their intrinsic multipotentiality, MSC have several and distinct reparative actions. Uncontrolled inflammation plays a critical role in the pathogenesis of non-unions and a selective modulation of the inflammatory response may become the target of new therapies to enhance the bone repair and to prevent the occurrence of a non-union. The role of MSC in the initiation of the callus formation has been scarcely investigated and most of the studies have focused on more advanced repair stages either during the cartilaginous callus maturation or the mineralization process [21, 126] .

Our studies were designed to determine: 1) the *in vivo* trafficking and homing within the fractured tibia of systemically transplanted MSC; 2) the need of CXCR4 for MSC homing; 3) the effects of MSC transplant in the callus biomechanical properties; 4) the MSC engraftment into the repairing tissue and contribution to the callus initiation; 5) the systemic and local anti-inflammatory effects of MSC in fracture repair.

## Materials and Methods

### Reagents

7-Amino-actinomycin D (7-DAA) was from Molecular-Probes; D-luciferin from Biosynth-International.

### Antibodies

Biotin-conjugated anti-mouse CD34, CD45, CD11b and CXCR4 antibodies from BD-Biosciences. Phycoerythrin-conjugated anti-mouse CXCR4, CD29, CD44, CD73, CD105, CD45 and control isotype antibodies from eBioscience.

Stabilized fracture model

All animal procedures were approved by the animal care committee of the University of North Carolina-Chapel Hill and Vanderbilt University. Stabilized tibia fractures were produced in 8-12 weeks old FVB female syngenic mice (FVB-NJ, Jackson-Laboratories) by intramedullar fixation using a 0.25mm stainless steel pin (Fine-Science-Tools) inserted through the patellar tendon inside the medullar canal of the tibia followed by closed fracture using a three-point bending device with a standardized force [30]. For pain control, bupremorphine (0.5 mg/kg) was administered subcutaneously.

Isolation and expansion of MSC

Primary cultures of BM-MSC were obtained by flushing the BM from femurs and tibias of 4-6 weeks old FVB-NJ mice as previously reported [65]. Briefly, BM nucleated plastic-adhering cells were expanded for 7-10 days without passaging [65]. Immediately before transplant, contaminating hematopoietic cells were eliminated by immunodepletion of the CD45, CD11b and CD34 positive cells using a MACS system (Miltenyi-Biotech). As shown in Figure 45, using this protocol we obtain a MSC population in which >90% of cells express the specific MSC markers CD73, CD29, CD44, and 67.5% the CD105 marker. Furthermore, MSC after immunodepletion were negative for CD45 (0.9±0.5%, n=3) and CD11b (1.1±1.3%, n=3). For BLI imaging, MSC were isolated from FVB/N animals constitutively expressing *Firefly luciferase* under the β-actin promoter (FVB/N-Tg(β-*Actin-luc*)-Xen) (CaliperLife-Sciences). After fracture, mice were transplanted with $10^6$ MSC by tail vein injection, unless specified. MSC were also isolated from the BM of the *CMV-R26R* or *BMP-2-Lac-Z* mice and

transplanted into wild-type female littermates. The *BMP-2-Lac-Z and CMV-R26R* mice were generated as described or previously reported [127].

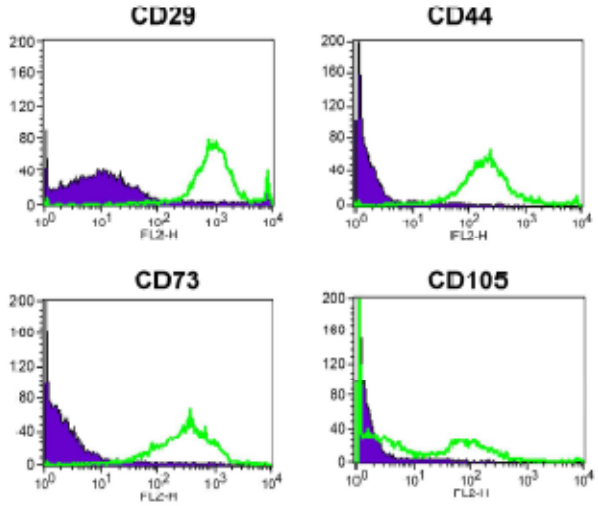


Figure 45. Highly purified population of primary cultured hematopoietic depleted MSC. Primary cultures of BM derived MSC were obtained by flushing the BM from femurs and tibias of 4 to 6 week old FVB syngenic mice, nucleated plastic-adhering cells were expanded for 7-10 days (> than 80% confluence) without passaging; immediately before transplant contaminating hematopoietic cells were eliminated by immunodepletion of the CD45, CD11b, and CD34 positive cells using conjugated antibodies in a MACS magnetic system. Figure depicts the FASC analysis for the specific MSC marker CD73, CD29, CD44, CD 105 in our MSC population. Our MSC population expressed in >90% of cells the CD73, CD29, CD44, markers and 67.5% the CD105 marker. Shaded histogram represents control isotypes, open histogram represents specific antibodies.

BLI analyses

BLI imaging was performed using an IVIS 200 imaging system (Caliper-Life-Sciences). Mice were anesthetized using 2.5% isofluorane in a vaporizer apparatus, leg and abdomen fur was shaved and mice were placed in a supine position for image acquisition. The BLI substrate D-luciferin was injected intraperitoneally (150 mg/kg).

Images were collected at 10, 15 and 20 minutes after D-luciferin injection using an acquisition time of 3 minutes. The maximal luminescence signal occurred 15 minutes after the D-luciferin injection and all images presented are collected at 15 minutes. BLI signaling at the fracture tibia site region of interest (ROI), measured as integrated photons/sec/cm$^2$/sr, was normalized by subtracting the background signal found in an equal ROI in the contralateral intact tibia. Imaging data were analyzed using the LivingImages2.20.1 (Xenogen-Corp.).

Luciferase expressing adenoviruses and MSC infection

An adenoviral vector that encodes the *Firefly luciferase* under the control of a cytomegalovirus promoter was used to generate highly purified (CsCl gradient) viruses as previously described [128]. All the experiments were performed using a multiplicity of infection of 1,000 in MSC cultured for 7 days. The adenoviral vector encodes bicistronically the Firefly luciferase and green fluorescent protein (GFP) under the control of a cytomegalovirus promoter. Efficiency of MSC infection and MSC viability was determined by two-color flow cytometry to detect GFP and 7-ADD fluorescence using a BD Biosciences FACSCalibur flow cytometer and by measuring the luciferase activity by BLI and luciferase assay (Promega) as previously reported (62). MSC cultured for 7 days, were infected overnight at increasing multiplicity of infection (MOI) of adenoviruses respectively 100, 1,000, 2,000, 10,000 MOI. The BLI and luciferase assay measurements correlated very well (R=0.9). Although the maximal luciferase activity was detected using 10,000 MOI, 30-40% of the cells died. With a MOI of 1,000, 34±5% of the cells were infected (GFP+) with more than 95% cell viability.

Biomechanical testing (BMT)

Fractured tibias were dissected 14 days post-fracture, wrapped PBS-embedded gauze and stored at -80°C until analysis. The bone ends were embedded with polymethylmetacrylate and loaded into the electroforce-based system ELF 3100 (Bose). The displacement rate was at 0.25 mm/min and a force-displacement curve recorded to calculate the ultimate distraction (maximum distraction at failure), ultimate force (maximum force at failure), toughness (area under the curve) and stiffness (maximum slope) using the WinTestControl Software (Bose).

Histology and *in situ* hybridization

Tibias were dissected 7 and 14 days post-fracture, histologically prepared and the entire callus sectioned (6µm). The callus center was identified as the largest diameter by H&E staining and analyses performed within 20 sections from the center. *In situ* hybridization analysis was performed as previously reported [129]. Plasmid with insertion of mouse Collagen (II)-alpha1-chain (*Col2a1*) was provided by D. Kingsley (Stanford University), mouse Collagen (I)-alpha-1-chain (*Col1a1*) and mouse *Osteocalcin* by G. Karsenty (Columbia University). Probe for mouse Collagen (X)alpha1chain (*Col10a1*) was generated as previously described [72]. Images were taken using an Olympus BX51 microscope with a DP71 camera, imported into Adobe Photoshop and formatted without using any imaging enhancement.

Micro computed tomography analysis of fracture calluses

Tibia fractures were dissected 14 days post-fracture and following removal of the pin and microCT scanned (Scanco Medical μCT40). microCT imaging were obtained at 55 kVp, 145 μA, 300 ms integration time using 6μm voxel resolution along 5.2 mm length centered at the fracture line with a total scanning time of approximately 1 hour. To determine material type from microCT scans, a parametric thresholding study was performed by serial microCT scanning and histological analysis. Tibia fractures were dissected 14 days post-fracture, and following removal of the fixation pin, were uCT scanned at 6 μm voxel resolution along ~5.2 mm length centered at the fracture line (Scanco Medical μCT 40). After microCT scanning, bones were prepared for histological analyses and sectioned at 6 μm thickness along ~5.2 mm length centered at the fracture line. This resulted in 864 histological sections per bone, which were placed 3 sections per slide and divided into 4 serial groups for staining, resulting in ~72 slides per group (72 slides x 3 sections/slide x 4 groups). In-situ hybridizations for Collagen 1 and Collagen 10 and Trichrome Blue and Safranin O/Fast Green histological staining were obtained. Trichrome Blue and Safranin O/Fast Green staining were performed using standard histological procedures as previously described (65). As shown in Figure 46, Collagen 1 in situ hybridization was used to label new bone, Collagen 10 in situ hybridization to label hypertrophic chondrocytes; Safranin O/Fast Green staining to label areas of cartilaginous tissue as bright red and areas of bone as green; Trichrome Blue staining to label newly mineralized bone as blue and highly mineralized bone as red. Each histological marker was volumetrically quantified by a custom built image analysis code (MATLAB, Mathworks) that was used to select areas of differing tissue type (soft

tissue, new bone, and cortical bone) based on color intensity. The microCT image stack was then thresholded based on CT attenuation into 3 groups that visually and quantitatively matched the histological staining determination of tissue type (soft tissue, new bone, and bone). These thresholds were then used to determine volumes of bone and soft tissue from the scanned specimens. To eliminate the effect of cortical bone on the bone and callus volume analysis, the cortical bone was segmented and removed from the microCT image volumes through the use of an automated segmentation analysis (Analyze, AnalyzeDirect). The microCT image volumes without cortical bone were then analyzed based on tissue volume and mineral content. To determine the callus HA mineralization content, we scanned phantoms with varying HA density (0–800 mg-HA/cm3) to generate a mg-HA/cm3 to CT attenuation standard curve through which we determined the HA density and total HA content of the microCT image volumes without cortical bone.

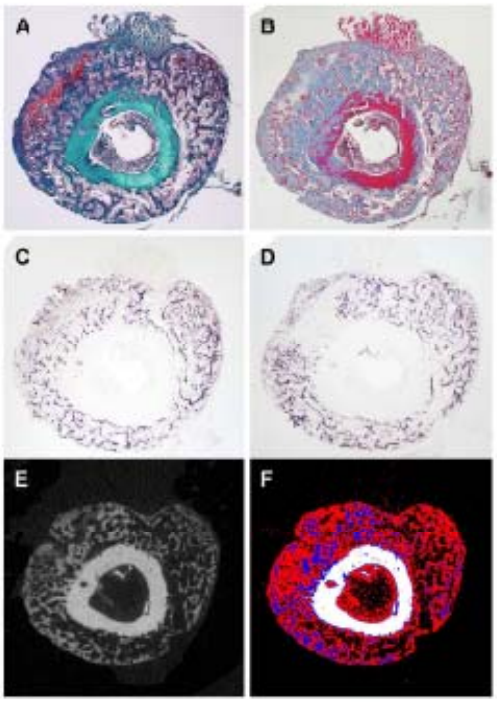


Figure 46. Callus material type studies based on microCT scan and histological analyses. After microCT scanning, calluses were prepared for histological analysis and sectioned at 6 um thickness. Sections were placed in 4 groups and used for: (A) Safranin O/Fast Green staining; (B) Trichrome Blue staining; (C) in situ hybridization analysis for Collagen1; (D) in situ hybridization analysis for Collagen10. Collagen 1 was used to label new bone, Collagen 10 for labeling of hypertrophic chondrocytes. Safranin O/Fast Green staining was used to label areas of cartilage (red) and bone (green). Trichrome Blue staining was used label newly mineralized bone as blue and highly mineralized bone as red. Each histological marker was volumetrically quantified and used to select the areas of differing tissue type based on color intensity. The uCT image stack (E) was threshold based on CT attenuation into 3 color groups matching visually and quantitatively the histological staining (F). The thresholds were used to determine volumes of bone and soft tissue from scanned specimens.

Circulating and callus cytokine measurements

Sera were obtained from mice that received MSC transplant and controls at day 1, 3 and 7 post-fracture. Tumor necrosis factor-α (TNF-α), interleukin-1 β (IL-1β), interleukin-10 (IL-10), interleukin-13 (IL-13), interleukin-6 (IL-6) levels were

determined using LINCOplex immunoassay (LINCO-Research). Total RNA obtained using Trizol and PureLinK columns (Invitrogen) from dissected calluses 3 and 7 days after fracture was reversed transcribed using SuperScript III reverse transcriptase (Invitrogen) and Oligod(T)16 (Applied Biosystems). *TNF*-α mRNA expression was measured by qRT-PCR (MyIQ-Single-Color-RT-PCR-System, Biorad) using Syber Green as previously described [37]. PCR primers for *TNF*-α amplification were: 5'-CCACCACGCTCTTCTGTCTAC -3' and 5'GGCTACAGGCTTGTCACTCG-3'. Samples were run in triplicates, data were normalized to βactin expression and analyzed using the $2^{-\Delta\Delta CT}$ method and expressed as fold of increases compared with the average of an untransplanted control, which was given the value of 1.

X-Gal staining

X-Gal staining was performed as previously described with some modifications [127]. Briefly, the fractured tibia was dissected, briefly fixed with 0.4% PFA and stained at room temperature with X-Gal staining solution. To achieve specific localization of cells which express prokaryotic (*Escherichia coli*) β-galactosidase, pH of the reacting solution was adjusted to selectively favor its activity over that of the mammalian enzyme [130, 131]. After staining, samples were fixed with 4% PFA for 24h paraffin embedded and sections were counter-stained using nuclear fast red as previously described [72, 127]. CMV-R26R-LacZ-MSC ($1X10^5$) were placed in 10µl medium in a 24-well plate and after 1 hour, 500µl of medium was added; cells were cultured for 24 hours and X-Gal stained as previously reported [72].

Generation of the BMP-2-Lac-Z mice

The BMP-2-Lac-Z mice were generated as previously reported using a bacterial artificial chromosome (BAC) system [132]. The mouse BAC clone RP23-85011, obtained from the Children's Hospital Oakland Research Institute, that spanned an approximately 240.8-kb genomic region, including the 11-kb Bmp2 transcription unit, 188.1 kb of 5' flanking sequence and 40 kb of 3' flanking sequence; an internal ribosome entry site-β-gal-geo cassette was inserted into the BMP-2 BAC, in place of Bmp2 exon 3 mature regioncoding sequences [132].

Generation of the CMV-R26R mice

The CMV-R26R mice were generated by crossing R26R mice in which the ROSA26 locus is targeted by gene-trapping so that Cre-recombination results in LacZ expression [133] with TgN(CMV-Cre)1Cgn mice in which the Cre gene is under the control of a human cytomegalovirus minimal promoter that is expressed before implantation during early embryogenesis, leading to the deletion of lox-P-flanked genes in all tissues, including germ cells. TgN(CMV-Cre)1Cgn mice were purchased from The Jackson Laboratory.

Statistics

Data are expressed as mean ± SD. Statistical analyses were performed using unpaired Student's *t*-test, ANOVA followed by *post-hoc* multiple comparison testing. The relationship between number of transplanted MSC and BLI signal was analyzed using a

dose-response sigmoid curve. The Graph-pad Prism Software was used. Statistical significance was set at $p<0.05$.

## Results

Systemically transplanted MSC: In vivo dynamic and time-dependent recruitment at the fracture site

To assess the *in vivo* MSC dynamic trafficking and homing in response to a pathological tibia fracture cue, $1X10^{6}$ MSC-β-Act-Luc, constitutively expressing *luciferase*, were transplanted into a mouse with stabilized tibia fracture and sequential BLI imaging was performed from day 1 to day 14 post-fracture/transplant. As depicted in Figure 47A (left panel), one day after the fracture/transplant MSC-β-Act-Luc were visualized at the lung site. On day 3 after the fracture, we observed that MSC began to localize at the fractured leg site (right tibia) where they persisted up to 14 days after the fracture/transplant (Figure 47A, left panel). Semi-quantitative analysis of the BLI signal of luciferase-tagged MSC over the fractured leg was time-dependent, increasing progressively from day 1 to day 7, without any further increase at day 14.

A

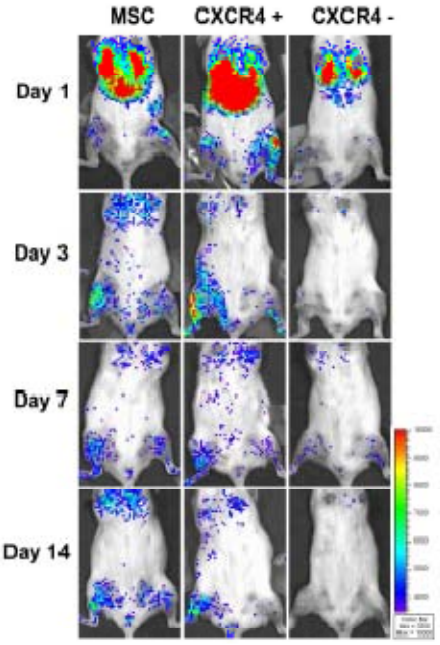


B

| | MSC | CXCR4+ | CXCR4- | P Value (ANOVA) |
|---|---|---|---|---|
| Day 3 post-fracture | 5317 ± 3468[a] n=14 | 6464 ± 4814[a] n=8 | 546 ± 433 n=8 | 0.0037 |
| Day 7 post-fracture | 7093 ± 2041[a] n=6 | 8526 ± 4202[a] n=4 | 133 ± 745 n=3 | 0.0057 |
| Day 14 post-fracture | 6508 ± 5350 n=5 | 18149 ± 6100[a,c] n=3 | 2440 ± 806 n=3 | 0.0109 |

Figure 47. MSC migrate to the fracture site in a time-and CXCR4-dependent manner. (A): BLI was performed at day 1, 3, 7 and 14 after fracture/transplant in mice with tibia fracture transplanted either with $10^6$ MSC-β-Act-Luc (MSC) (left panel), MSC-β-Act-Luc-CXCR4+ (CXCR-4+) (middle panel) or MSC-β-Act-Luc-CXCR4-(CXCR-4-) (right panel). Graded color bar indicates BLI signal intensity expressed as photons/sec/cm$^2$/sr. (B): BLI signal semi-quantitative analysis. Signal at the fracture tibia site ROI measured as photons/sec/cm$^2$/sr, was normalized by subtracting the background signal found in an equal ROI in the contralateral unfractured tibia. [a]$p<0.05$ versus CXCR4-group; [b]$p<0.01$ versus CXCR4-group; [c] $p<0.05$ versus MSC by Tukey post-test. Abbreviations: MSC, mesenchymal stem cells.

The presence of CXCR4 is essential for MSC homing at the fracture site

The finding that MSC have the ability to migrate to an injured tibia implies that they own specific homing signal(s). While CXCR4 has been involved in the hematopoietic stem cell engraftment and cancer cell metastasis, its role in MSC homing still needs to be defined [117, 118, 133-135]. In our study, using primary cultures of unpassaged MSC immunodepleted of hematopoietic cells, we first found that ~30% of MSC express CXCR4 (34.2±4.7%, n=4 MSC cultures obtained from the BM of at least 4 mice for each culture). Second, we separated, using CXCR4 immunoselection, the MSC population as MSC-CXCR4(+) and MSC-CXCR4(-) populations that were injected into a mouse with a tibia fracture. One day post-fracture both MSC-CXCR4(+) and MSC-CXCR4(-) had a localization pattern similar to the unselected MSC (Figure 47A). However, at day 3, MSC-CXCR(-) were not capable of homing to the fracture site, while the MSC-CXCR(+) showed an intense signal (Figure 47A, middle and right panels). A similar scenario was observed at day 7 and day 14 following the fracture/transplant (Figure 47, middle and right panels). As shown in Figure 47B, semi-quantitative analysis of the BLI signal confirmed that the MSC-CXCR4(-) migration to the fracture site at any studied time-point was negligible; whereas, MSC-CXCR4(+) showed a time-dependent increase of MSC-luciferase signal at the fractured tibia**.** Our data demonstrate that systemically transplanted MSC are capable of homing at the fracture site and the migration is dependent on the presence of CXCR4.

Dose-dependent MSC homing at the fracture site

To assess the dose-dependent MSC homing at the fracture site, we systemically infused MSC transduced with an adenoviral vector expressing *luciferase* (MSC-Adn-Luc) into mice with a tibia fracture. We reasoned that since adenoviruses do not integrate in the host genome, and expression is lost in dividing cells, the luciferase signal would exclusively assess the MSC migration to the fracture site. As shown in Figure 48A, in mice with fractured tibia transplanted with increasing doses of MSC-Adn-Luc (from $5X10^3$ to $1000X10^3$ MSC) and BLI imaged 3 days later, we found that MSC homing was dose-dependent. Interestingly, we found the ED50 to be a dose of $300X10^3$ , with a plateau at $700X10^3$ without any significant increase at a dose of $1000X10^3$ (Figure 48C). This finding indicates that MSC migration to the injured site reaches a saturation point and a limiting mechanism that needs further investigations can be hypothesized.

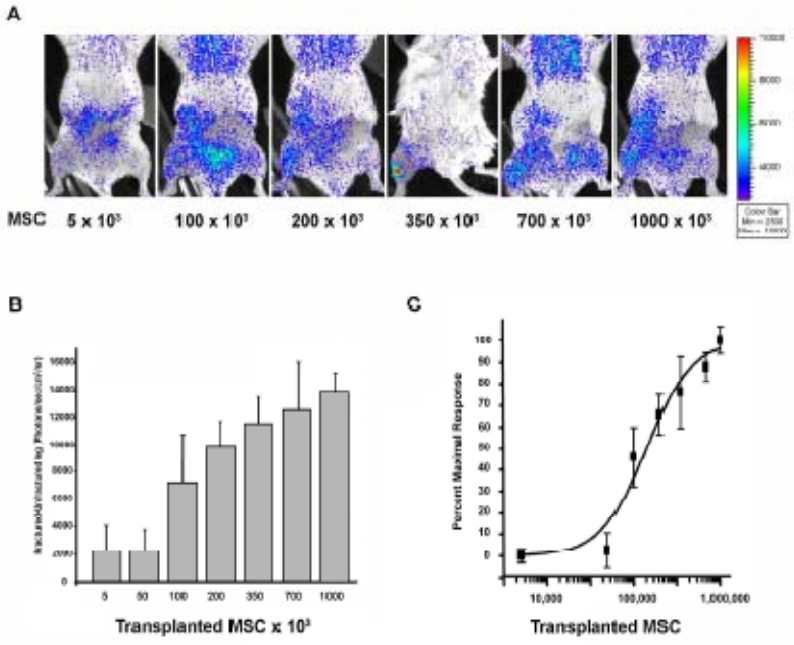


Figure 48. Does-dependent homing of transplanted MSC in response to tibia fracture. (A): representative BLI imaging of mice with a fracture in the right tibia transplanted with increasing numbers of MSC adenovirally transduced to express luciferase. MSC were transplanted after tibia fracture and BLI analysis was obtained 3 days after fracture. An increase of BLI signal over the right tibia is depicted. Graded bar indicates BLI intensity expressed as photons/sec/cm$^2$/sr. (B): BLI signal at the fracture tibia ROI was normalized by subtracting the background signal found in an equal ROI in the contralateral intact tibia. BLI signaling increased in a dose-dependent manner, $p<0.01$ by ANOVA. (C): a sigmoid dose-response curve was generated using BLI results are expressed as a percent of the maximal signal; the relative $ED_{50}$ was found at a dose of $300X10^3$ cells and a plateau was observed after $700X10^3$ cell transplant. Three mice per dose were analyzed.

MSC improve the biomechanical properties of the fracture callus

A critical feature of bone healing is that the regenerated tissue provides sufficient strength to the injured limb in order to regain function. To investigate whether MSC improved the callus material properties we performed distraction-to-failure BMT. Dissected calluses from MSC recipient mice (MSC) as well as control calluses from mice that did not receive MSC (no cells), were subjected to a gradual distraction force until

they broke. As shown in Table 14, calluses of mice that received MSC had increased toughness and ultimate displacement compared to controls. The peak force was not different in the two groups while, there was a trend over a decrease of callus stiffness in the mice that received MSC. Taken together, these data indicate that MSC improved the callus material properties making the tissue less brittle by decreasing the structural rigidity.

Table 14. MSC improve the biomechanical properties of the fracture callus. Fourteen days after tibial fracture, calluses from mice that were transplanted either with MSC or control (no cells) were dissected and subjected to distraction-to-failure BMT. [a]$p<0.05$ versus No cells; [b]$p<0.01$ versus No cells by Student's *t*-test. Abbreviations: MSC, mesenchymal stem cells; BMT, biomechanical testing; N, Newton.

| | No Cells (n=5) | MSC (n=6) |
|---|---|---|
| **Toughness (N·mm)** | 0.138 ± 0.044 | 0.425 ± 0.143 [b] |
| **Ultimate Force (N)** | 1.803 ± 0.488 | 2.492 ± 0.829 |
| **Stiffness (N/mm)** | 17.790 ± 8.861 | 12.000 ± 7.591 |
| **Ultimate Displacement (mm)** | 0.124 ± 0.045 | 0.308 ± 0.148 [a] |

MSC effects on callus size and morphology

To determine material type (bone and soft tissue) from microCT scans, a parametric threshold study of an entire callus was performed by serial microCT scanning

and histological analyses (*in situ* hybridizations for *Collagen 1*, *Collagen 10*, and Trichrome-Blue and Safranin-O/Fast-Green staining). Mice that received MSC transplant displayed a significant increase of the total volume, as well as total bone, soft tissue, new bone, and callus volumes and callus mineralization content compared to controls (Figure 49A). The three-dimensional reconstructions of the entire calluses as well as the sagittal sections showed remarkable differences in the size and morphology of the new mineralized callus in mice that received MSC *versus* controls. As shown in Figure 49B, the most notable differences were that: 1) a large callus surrounded the fractured bone edges as well as the intact cortical bone in the calluses from mice transplanted with MSC, but remained limited to the ends of the bone segments in the controls [compare panels B1 with B5 and B3 with B7]; 2) a continuous net of the creeping callus bridging the fracture gap in MSC recipient mice versus the limited connectivity observed in the controls [compare panels B2 with B6 and B4 with B8]. These findings indicate that MSC transplant by providing a more organized bridge between the bone ends improves the repairing process and therefore its material properties.

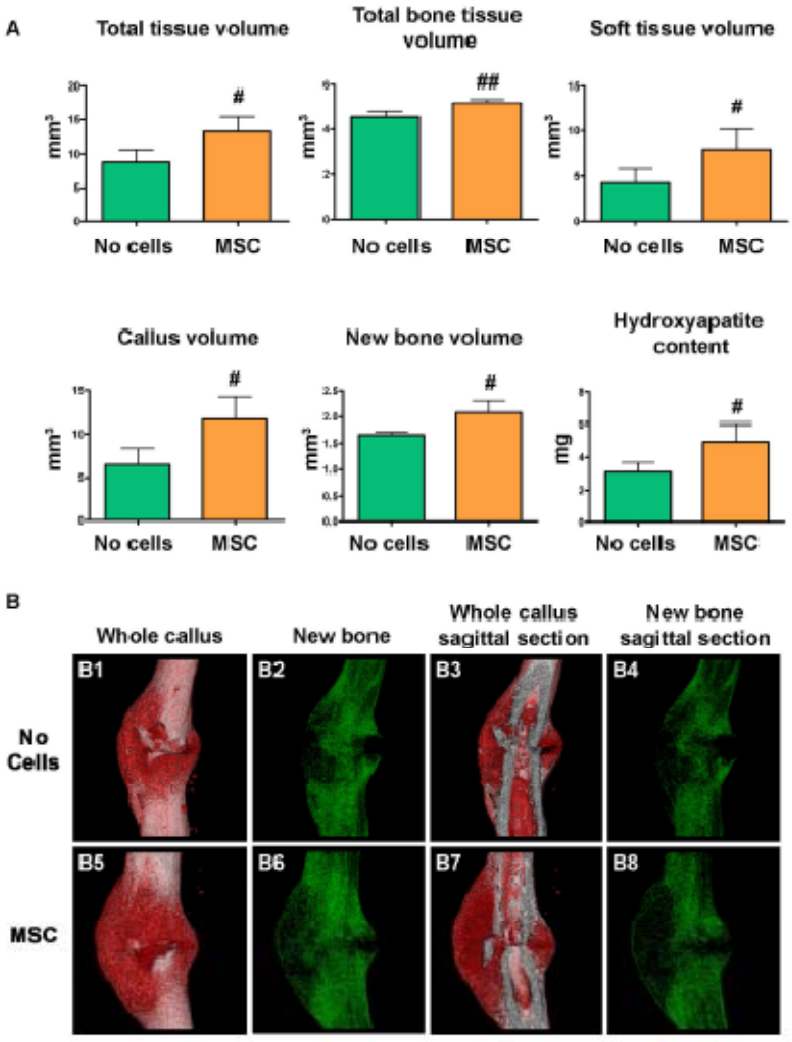


Figure 49. MSC transplant increases callus size and changes callus morphology. (A): microCT analyses were performed 14 days after fracture in calluses dissected from mice that received MSC transplant and controls (no cells). Callus volume and new bone volume were calculated after subtracting the cortical bone volume respectively from the total volume and the total bone tissue volume. #, $p<0.05$ versus No cells; ##, $p<0.01$ versus no cells by Student's *t*-test. No cells, n=3; MSC, n=6. (B): three-dimensional reconstruction of whole calluses (B1, B2, B5, B6) and sagittal sections (B3, B4, B7, B8) were obtained 14 days after tibial fracture in calluses from mice that were transplanted with MSC or control untransplanted (no cells). Material type analysis of new bone, and soft tissue was determined by a histological-based thresholding of the microCT imaging scans. Abbreviations: MSC, mesenchymal stem cells.

MSC effects on callus histology

We next analyzed the callus histology as well as bone and cartilaginous marker expressions at day 7 and 14 after the fracture and MSC transplant. H&E staining analyses, showed that at 7days, the calluses from mice transplanted with MSC were bigger than controls and demonstrated larger areas of cartilage-like tissue (Figure 50A). *In situ* hybridization for *Collagen 2* and *Collagen 10* expression as well as Safranin-O staining revealed a more abundant presence of either chondrocytes or hypertrophic chondrocytes in the calluses from mice transplanted with MSC, indicating that the fracture repair in those mice more predominately proceeded through an endochondral ossification process than controls (Figure 50A). When evaluated at 14 days after the fracture, *Collagen 10* expression was also consistently higher in mice that received MSC than controls and at this time, it was associated with an increase of *Collagen 1* expression indicating that the endochondral callus progressed to bone formation (Figure 50B).

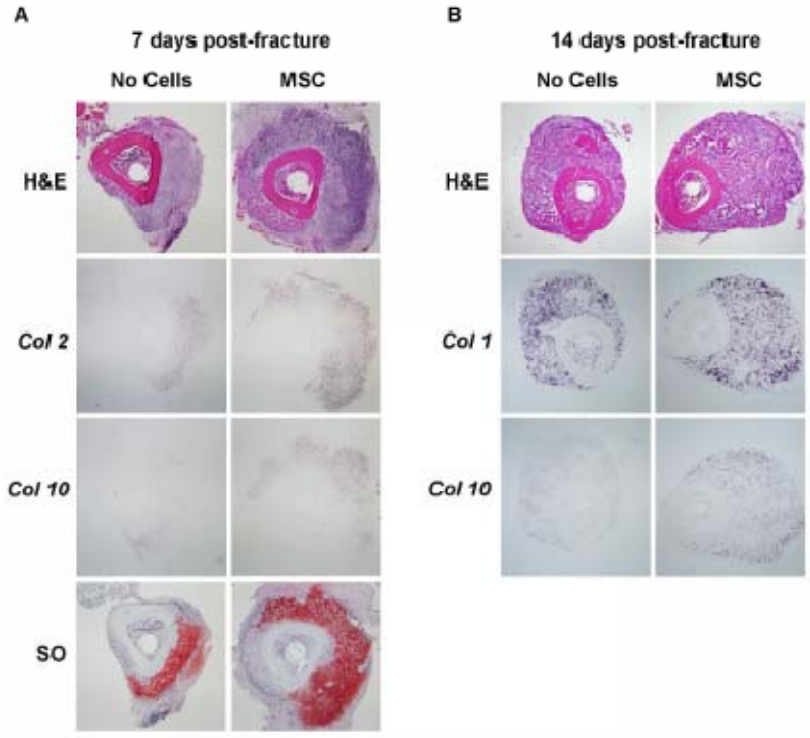


Figure 50. MSC transplant increases the cartilageneous and bone content of the callus. (A): transversal sections of 7 days post-fracture calluses were subjected to H&E and Safranin O staining and *in situ* hybridization for *Collagen-2* and *Collagen-10*.(B): 14 days post-fracture transversal sections were subjected to H&E staining and *in situ* hybridization for *Collagen-1* and *Collagen-10*. The entire callus was sectioned (6 µm thick sections), the center of the callus was identified by the largest diameter of callus size by H&E staining and further analyses were performed within 20 sections from the center. Analyses were done in at least 5 sections for each probe or staining. Sections were obtained from at least 3 mice for each group. Abbreviations: H&E, hematoxylin & eosin; Col2, collagen 2; col1, collagen 10; SO, Safranin O; Col1, collagen 1; MSC, mesenchymal stem cells. 40X magnifications are presented.

MSC distribution within the callus

To analyze the cellular distribution of transplanted MSC within the callus, fractured mice were transplanted with MSC from *CMV-R26R* mice and 7 days after fracture-transplant dissected calluses were Lac-Z stained. As shown in Figure 51, CMV-R26R-LacZ-MSC express stainable β-Gal activity, indicating this as a suitable reporter

system for MSC. As negative control for the Lac-Z staining protocol, 7-day post fracture calluses from wild-type mice were Lac-Z stained. As shown in Figure 52, no staining was detectable indicating that the protocol used did not result in any background.

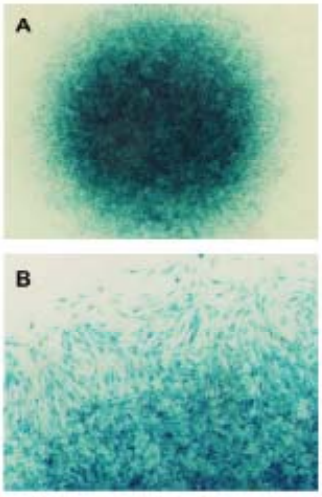


Figure 51. CMV-R26R-MSC ex-vivo X-Gal staining. After isolation, CMV-R26R-MSC were seeded at high density, $1X10^6$ cells in 10 ul medium, after 1 hour, 500 ul of medium was added and 24 hours later cells were X-Gal stained. (A); depicts the CMV-R26R-MSC micromass showing an intense Beta-gal activity. (B): higher magnification of the CMV-R26R-MSC micromass showed that all the cells were stained and therefore targeted for the ROSA26 locus by the Cre recombinase under the CMV minimal promoter.

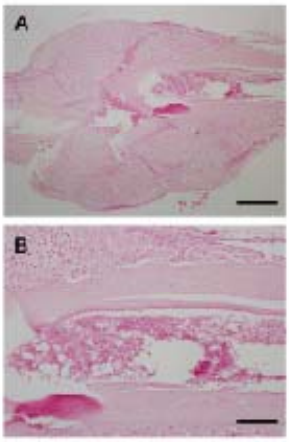


Figure 52. Absence of Beta-gal activity into the fracture callus of wild-type mice. Tibias from wild-type mice were fractured and after 7 days dissected and stained for Beta-gal. (A); paraffin sections, counter-stained with nuclear Fast Red showed no endogenous Beta-gal activity in the callus. (B); higher magnification showed no staining in the regions of interest; bone marrow, endosteum or fracture rim. (A), scale bar 500 micrometers; (B) scale bar 200 micrometers.

As shown in Figure 53A, we found that transplanted CMV-R26R-LacZ-MSC localized within specific areas of the callus, in particular within the fracture ridge, the endosteum close to the fracture rim and the BM. Counterstaining the calluses with Safranin-O/Fast-Green (Figure 53B), we identified that MSC localized within the endosteal callus in the areas of most active bone formation. Higher magnification of these areas showed that the Lac-z positive MSC (stained in Blue) were embedded in the bone matrix (stained in Green) as osteoblasts within the newly forming bone Figure 53C) or as newly formed osteocytes with abundant cytoplasm (Figure 53D). As shown in Figure 54, *in situ* hybridization analysis confirmed that within the margins of the woven bone, some of the Lac-z positive MSC expressed also *osteocalcin* confirming their ability to differentiate into osteoblasts. Our findings indicate that transplanted MSC localize within different and specific niches of the callus and the number of MSC within the

newly forming bone seems to be limited compared to the significant effects of MSC on the callus biomechanical properties. This observation led us to hypothesize that the contributions of MSC to the fracture healing is likely through multiple mechanisms that include but cannot limited to the callus mineralization.

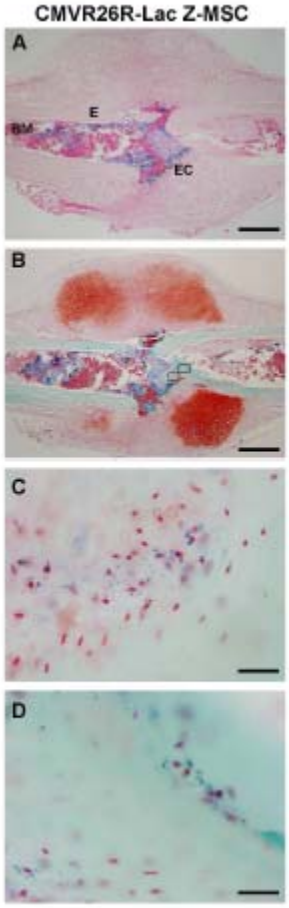


Figure 53. Transplanted MSC localize within specific niches of the fracture callus. $10^6$ CMVR26-Lac-Z-MSC were transplanted into fractured mice, calluses dissected 7 days after fracture and X-gal stained. (A): paraffin sections of the β-gal stained calluses were counter-stained with nuclear Fast Red showing MSC localization into specific areas of the fracture callus. (B): paraffin sections of β-gal stained calluses were counter-stained with Safranin O/Fast Green. (C): higher magnification of the open box depicted in B, showed MSC embedded into the bone matrix as osteoblasts. (D): higher magnification of the close box depicted in B, showed MSC also integrated into the bone matrix as newly formed osteocytes. (A, B) scale bar 500 micrometers; (C, D), scale bar 33 micrometers. Sections were obtained from at least 3 mice. Abbreviations: BM, bone marrow (BM); E, endosteum; EC, endosteal callus.

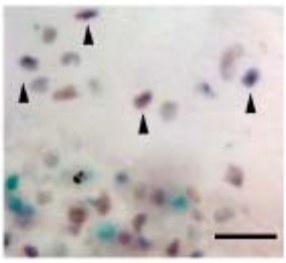

Figure 54. Some of the Lac-z positive MSC express osteocalcin. $10^6$ CMVR26-Lac-Z-MSC were transplanted into fractured mice, calluses dissected 7 days after fracture and X-gal stained. Paraffin sections (6 um thick sections), of the Beta-gal stained calluses were subjected to in situ hybridization for Osteocalcin. Within the woven bone, some of the Lac-z positive MSC (blue staining cells) double stained for osteocalcin (brown staining) as indicated by arrows. Scale bar 50 micrometers. Sections were obtained from at least 3 mice.

MSC contribute to the callus initiation by expressing BMP-2

To determine the contribution of MSC to the initial phase of the callus formation, we analyzed whether transplanted MSC were capable of expressing BMP-2 within the callus. BMP2 is highly expressed during fracture healing and is essential for the callus initiation [7]. In fact, in mice null for BMP-2 expression in limb mesenchyme progenitors, the earliest steps of fracture healing are blocked and mice lack fracture healing [7]. For this purpose, we obtained MSC from *BMP-2-Lac-Z* mice genetically modified using a BAC system to be β-gal reporters for BMP-2 expression [127]. BMP-2-Lac-Z–MSC were transplanted into fractured mice, calluses were dissected 7 days after the fracture and Lac-Z stained. We found that BMP-2-Lac-Z-MSC localized within the fracture rim and more peculiarly along the endosteum adjacent to the fracture edges (Figure 55A-B). This pattern was similar to the pattern observed in the fractured mice transplanted with CMV-R26R-LacZ-MSC, although the mice transplanted with BMP-2-Lac-Z– MSC lacked the Lac-Z staining within the BM cells. Our data indicate that

transplanted MSC localize at the fracture site and are capable of expressing BMP-2, an essential gene for initiating the fracture repair process. To determine the endogenous BMP-2 expression at the same fracture healing stage, calluses were obtained 7 days after fracture from *BMP-2-Lac-Z* fractured mice and Lac-Z stained. As shown in Figure 55C-D, we found that BMP-2 is highly expressed at the fracture rim and interestingly no expression was detectable at the endosteal site. This observation may indicate that the endosteum is a peculiar niche where the transplanted MSC engraft and express BMP-2.

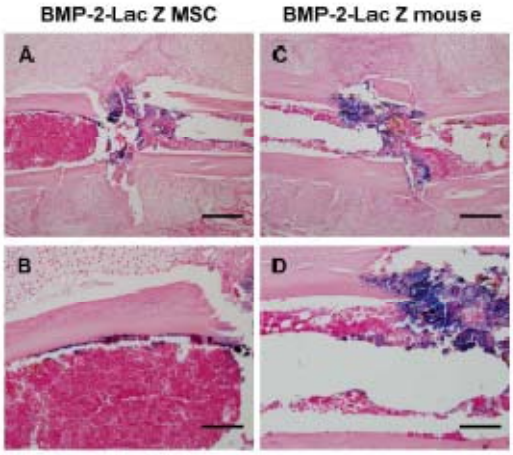


Figure 55. Transplanted MSC express BMP-2 within the fracture and localize at the endosteal site of the callus. (A): $10^6$ BMP-2-LacZ-MSC were transplanted into fractured mice and 7 days after fracture the calluses were dissected and X-gal stained. Paraffin sections were counter-stained with nuclear Fast Red showing that MSC localize and express BMP-2 into the fracture rim and endosteum. (B): higher magnification of A showing the endosteal localization of MSC expressing BMP-2. (C): BMP-2-Lac-Z mice were fractured and 7 days post-fracture calluses were dissected and β-gal stained, paraffin sections were counter-stained with nuclear Fast Red and showed BMP-2 expression at the fracture ridge. (D): higher magnification of the fracture rim showing expression of BMP-2. (A, C) scale bar 500 micrometers; (B, D) scale bar 200 micrometers. Sections were obtained from at least 3 mice. Abbreviations: BMP-2, bone morphogenic protein-2.

MSC transplant modulates the systemic and local inflammatory responses

To determine whether the beneficial contributions of MSC to the fracture healing was associated with an anti-inflammatory action, we sequentially determined the circulating levels of a set of cytokines in the serum of mice either transplanted with MSC or controls. As shown in Figure 56, over the first week after the fracture, MSC transplant selectively down-regulated the serum levels of TNF-α and IL-1β abolishing the injury-induced inflammatory response found in the control fractured mice. The MSC anti-inflammatory action was targeted to specific cytokines, in fact, MSC had no effect on IL-13 and IL-10 at any time and had only a significant effect reducing IL-6 levels at day 3 post-fracture (Figure 56C-E). MSC had similar effects on the local mRNA expression of TNF-α that was decreased in the calluses from MSC transplanted mice compared to controls at day 3 (MSC: 1.278±1.741 fold of change; control: 3.78±3.006; $P<0.05$; n=6) and day 7 (MSC: 0.670±0.315 fold of change; control: 2.729±2.334; $P<0.05$; n=6) post-fracture.

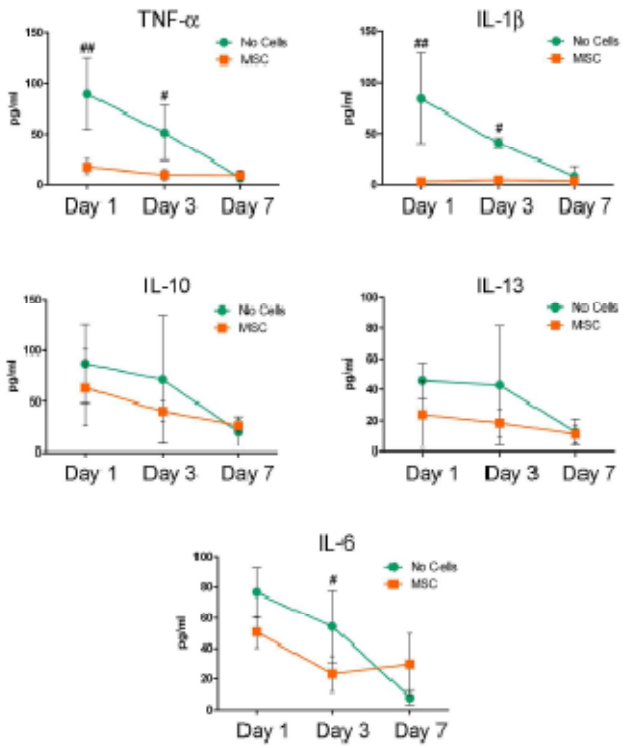


Figure 56. Transplanted MSC have a specific systemic anti-inflammatory effects on the cytokines released after tibia fracture. Cytokines were measured in sera obtained 1, 3 and 7 days after fracture from mice either transplanted with MSC or controls (no cells) by LINCOplex immunoassay. Sera were obtained from at least 4 mice for each group at each corresponding time. #, $p<0.05$ vs control at the corresponding time; ##, $p<0.01$ vs control at the corresponding time by Tukey post-test. Abbreviations: TNF-α, tumor necrosis factor-α; IL-1β, interleukin-1 β, IL-10, interleukin 10; IL-13, interleukin 13; IL-6, interleukin 6.; MSC, mesenchymal stem cells.

## Discussion

In our studies, we have characterized, in living animals, the dynamic migration of MSC in response to a bone fracture and determined that this specific migration at the site of injury is driven by CXCR4. We have also demonstrated that MSC transplant induces a biomechanical improvement of the healing process that is associated with an increase in the callus volumes and cartilaginous and bone contents. We have found that MSC

engraft into specific niches of the callus expressing the fracture repair initiator BMP-2 and that the delivery of MSC has a specific systemic and local anti-inflammatory effect. In summary, our report provides a comprehensive assessment of the contributions of transplanted MSC to the fracture healing process.

There is a significant body of evidence that links MSC to tissue regeneration, including bone and cartilage [81]. However, *in vivo* studies have been primarily performed using *post-mortem* analyses; as a result longitudinal evaluations of MSC dynamic in living animals are scarce [114]. Furthermore, studies have been limited in the attempt to demonstrate one of the regenerative effects of MSC, mostly the differentiation into bone, lacking an ample evaluation of the multiple actions of MSC. The regeneration of damaged tissue implies that different responses converge at the damaged area. The regenerative cells need to be recruited at the injury site, control the injury-induced responses and eventually contribute to the repair. In our studies, we have demonstrated that MSC exert their regenerative properties by contributing to each of the stages of fracture healing. Transplanting MSC tagged with luciferase in combination with BLI analysis, we have demonstrated that MSC migrate to a fracture site and migration is time- and dose-dependent. Recruitment of circulating progenitor cells to the site of injury occurs as a normal biological process during the fracture process [136]. We hypothesize that MSC injected systemically migrate to the fracture site using a similar injury-related recruitment mechanism. Gao et al, using $^{111}$I-indium-MSC investigated the MSC dynamic only for 48 hours after cell infusion into normal non-injured rats [114]. Authors found that after injection, cells distributed into the lungs and the liver and a vasodilator increased the liver localization [114]. We found similar results in our short-term BLI

studies, but our long-term analyses in fractured mice allowed us to determine that three days after the fracture/transplant, MSC were specifically recruited at the fracture site where they remained up to 14 days. Thus, the use of MSC transplant seems to be a valid strategy to allow a non-invasive increase of viable progenitors at a fracture site.

We have found that fracture MSC migration is dependent on the presence of CXCR4. There are discordant data on whether MSC express CXCR4 and its role in MSC migration [117, 118, 133-135]. Differences in culture passages may be the reason for such discordances; in fact, cell passaging causes a down-regulation of CXCR4 expression and loss of MSC homing [117, 132, 137]. We have used primary cultures of unpassaged MSC immunodepleted of hematopoietic cells and found a consistent CXCR4 expression in ~30% of the MSC population. Cheng *et al*., have recently reported that MSC recruitment was enhanced in a rat model of myocardial infarction by retrovirally overexpressing CXCR-4 in MSC that lacked CXCR4 [138]. In our study, we have found that, without any CXCR-4 manipulation, native primary cultured MSC are capable of homing at a fracture site in a CXCR4 dependent manner.

In our study, we found that MSC transplant improves the fracture healing by increasing the material toughness of the callus and causing it to be less brittle. The observed biomechanical material data were consistent with the microCT imaging that showed in MSC recipient mice some remarkable differences in the callus geometry that was larger with more organized bridging structures characterized by soft tissue and new bone. Histological analyses confirmed that the fracture healing in MSC recipient mice progressed through more cartilage and newly mineralized bone than controls. Tibia fractures necessitate long period for healing. Optimization of clinical management can

reduce the healing time, however it has been pointed out that even if osteogenic cells at the fracture site are working at full capacity, they will not heal the defect if too few cells are present, nor will any drug, directed at enhancing bone formation be effective since maximal osteogenesis per cell is already occurring [139]. Our studies provide evidence that even in a normal fracture healing tibia model, MSC transplant enhances the repair process supporting the use of MSC to provide a critical number of regenerative cells to achieve the desired bone-repairing results in patients with high-energy fractures. Although some non-union animal models are available, these models are based either on mice with genetic defects that lead to repair impairments, or by creating large bone gaps or stripping the periosteum in order to decrease the number of regenerative progenitors. None of these models reflects the mechanisms for non-unions found in patients. Furthermore, the healing times in those models are largely inconsistent making problematic the interpretation of results when multiple experimental groups are studied. On the other hand, the stabilized fracture tibia model we have used has a consistent healing time and having found that in this model, MSC have several positive effects opens optimistic prospective for using MSC in non-unions.

In our studies using Lac-Z tagged MSC, we found that transplanted MSC localize along the margins of woven bone where they assume the morphology of active osteoblasts, express osteocalcin and associate with the endosteal surface. Interestingly, MSC did not localize within the periosteal callus although the overall size of the callus of MSC transplanted mice was larger and showed larger areas of newly forming bone. This observation led us to pursue studies aimed at determining whether the MSC regenerative effects were not exclusively related to their differentiative abilities into bone but also to

their contributions on the initiation of the healing process. Our study is the first to report that systemically injected MSC localize at the fracture site where they are capable of expressing BMP-2, an essential initiator of the fracture repair process [7]. One interesting finding from our study is that MSC expressing BMP-2 localize very distinctly at the endosteum site. The endosteum maintains the bone homeostasis, participates in the fracture healing process and a lack of the endosteal callus formation is critical in the pathogenesis of non-unions [140-142]. Several cells form the endosteal niche including osteoblasts, CXCL12-abundant reticular (CAR) cells, MSC and hematopoietic stem cells. There is a large body of evidence that support the notion that the endosteal osteoblasts provide a variety of factors that regulate the hematopoietic stem cell number and function [reviewed in [143, 144]]. It has been hypothesized that in the endosteal niche CAR cells together osteoblasts, and potentially other cell types, generate a hypoxic environment that maintains the hematopoietic stem cells in a quiescent state [144]. The inhibitory effect of MSC on cell proliferation *in vitro* raises the possibility of a MSC role in maintaining the hematopoietic stem cells in this quiescent state [145]. On the other hand, hemapotopoietic stem cells regulate MSC induction into osteoblasts *in vitro* as well as *ex-vivo* [146] . Our knowledge of the MSC niches within native tissues is very poor and even less is known about the MSC niches after transplant. Our study provides evidence for the homing of circulating transplanted MSC in response to a fracture injury cue into the endosteal niche, where they express BMP-2. It is plausible that MSC expressing CXCR4 are recruited to the endosteal niche by CAR cells. We hypothesize that MSC within the endosteal niche can either differentiate into osteoblasts, or through a paracrine action, control the injury-related inflammatory response. It will be of great interest to

evaluate in future longitudinal studies the contributions of MSC through all the reparative process.

Several studies have shown that MSC have the ability to suppress the inflammatory response *in vitro* as well as *in vivo* (reviewed in [81, 119, 120]). These anti-inflammatory effects were induced through paracrine mechanisms that shifted the tissue milieu from a pro-inflammatory to an anti-inflammatory state [121-124]. During the tissue repairing process a precise temporal and spatial resolution of the inflammatory response is critical to limit the tissue injury, to prevent the development of fibrosis, and ultimately to promote the regeneration. Uncontrolled inflammation plays a critical role in the pathogenesis of non-unions. Traditional anti-inflammatory drugs that block the cytokine response *in toto* are unable to direct and selectively control the process and may actually have negative effects on the healing process. In our study, we have found that the beneficial effects of MSC transplant on fracture regeneration are associated with a selective effect on systemic and local cytokine production. MSC as selective modulators of the inflammatory response may become the target of new therapies to enhance the healing process in patients with non-unions.

## Summary

In summary, we have determined that transplanted MSC improve the fracture repair process and we have elucidated several of the mechanisms involved in these beneficial effects. We have characterized the dynamic of MSC migration and the essential role of CXCR4, we have found the niches for MSC recruitment at the injury site and we have determined that MSC contribute to the fracture healing by expressing BMP-

2 and modulating the injury-related inflammatory response. Our findings provide some critical information to implement the development of MSC-based therapies in patients with poorly healing fractures.

# REFERENCES


[1] Granero-Molto F, Weis JA, Miga MI, Landis B, Myers TJ, O'Rear L, Longobardi L, Jansen ED, Mortlock DP, Spagnoli A. Regenerative effects of transplanted mesenchymal stem cells in fracture healing. Stem Cells l2009;27: 1887-98.

[2] Einhorn TA. The cell and molecular biology of fracture healing. Clinical Orthopaedics and Related Research l1998: S7-S21.

[3] Martini FH, Bartholomew EF. Essentials of Anatomy & Physiology. 4th ed. San Francisco, CA: Benjamin Cummings; 2006.

[4] Einhorn TA. Enhancement of fracture-healing. J Bone Joint Surg Am l1995;77: 940-56.

[5] Marsh D. Concepts of fracture union, delayed union, and nonunion. Clinical Orthopaedics and Related Research l1998: S22-S30.

[6] Bhandari M, Guyatt GH, Swiontkowski MF, Tornetta P, 3rd, Sprague S, Schemitsch EH. A lack of consensus in the assessment of fracture healing among orthopaedic surgeons. J Orthop Trauma l2002;16: 562-6.

[7] Tsuji K, Bandyopadhyay A, Harfe BD, Cox K, Kakar S, Gerstenfeld L, Einhorn T, Tabin CJ, Rosen V. BMP2 activity, although dispensable for bone formation, is required for the initiation of fracture healing. Nature Genetics l2006;38: 1424-1429.

[8] Friedenstein AJ, Chailakhyan RK, Gerasimov UV. Bone marrow osteogenic stem cells: in vitro cultivation and transplantation in diffusion chambers. Cell Tissue Kinet l1987;20: 263-72.

[9] Friedenstein AJ, Gorskaja JF, Kulagina NN. Fibroblast precursors in normal and irradiated mouse hematopoietic organs. Exp Hematol l1976;4: 267-74.

[10] Colter DC, Sekiya I, Prockop DJ. Identification of a subpopulation of rapidly self-renewing and multipotential adult stem cells in colonies of human marrow stromal cells. Proc Natl Acad Sci U S A l2001;98: 7841-5.

[11] Digirolamo CM, Stokes D, Colter D, Phinney DG, Class R, Prockop DJ. Propagation and senescence of human marrow stromal cells in culture: a simple colony-forming assay identifies samples with the greatest potential to propagate and differentiate. Br J Haematol l1999;107: 275-81.

[12] Johnstone B, Hering TM, Caplan AI, Goldberg VM, Yoo JU. In vitro chondrogenesis of bone marrow-derived mesenchymal progenitor cells. Exp Cell Res l1998;238: 265-72.

[13] Johnstone B, Yoo J. Mesenchymal cell transfer for articular cartilage repair. Expert Opin Biol Ther l2001;1: 915-21.

[14] Johnstone B, Yoo JU. Autologous mesenchymal progenitor cells in articular cartilage repair. Clin Orthop Relat Res l1999: S156-62.

[15] Mackay AM, Beck SC, Murphy JM, Barry FP, Chichester CO, Pittenger MF. Chondrogenic differentiation of cultured human mesenchymal stem cells from marrow. Tissue Eng l1998;4: 415-28.

[16] Pereira RF, Halford KW, O'Hara MD, Leeper DB, Sokolov BP, Pollard MD, Bagasra O, Prockop DJ. Cultured adherent cells from marrow can serve as long-lasting

precursor cells for bone, cartilage, and lung in irradiated mice. Proc Natl Acad Sci U S A l1995;92: 4857-61.
[17] Sekiya I, Larson BL, Smith JR, Pochampally R, Cui JG, Prockop DJ. Expansion of human adult stem cells from bone marrow stroma: conditions that maximize the yields of early progenitors and evaluate their quality. Stem Cells l2002;20: 530-41.
[18] Sekiya I, Vuoristo JT, Larson BL, Prockop DJ. In vitro cartilage formation by human adult stem cells from bone marrow stroma defines the sequence of cellular and molecular events during chondrogenesis. Proc Natl Acad Sci U S A l2002;99: 4397-402.
[19] Yoo JU, Barthel TS, Nishimura K, Solchaga L, Caplan AI, Goldberg VM, Johnstone B. The chondrogenic potential of human bone-marrow-derived mesenchymal progenitor cells. J Bone Joint Surg Am l1998;80: 1745-57.
[20] Yoo JU, Mandell I, Angele P, Johnstone B. Chondrogenitor cells and gene therapy. Clin Orthop Relat Res l2000: S164-70.
[21] Bruder SP, Jaiswal N, Ricalton NS, Mosca JD, Kraus KH, Kadiyala S. Mesenchymal stem cells in osteobiology and applied bone regeneration. Clin Orthop Relat Res l1998: S247-56.
[22] Bruder SP, Kraus KH, Goldberg VM, Kadiyala S. The effect of implants loaded with autologous mesenchymal stem cells on the healing of canine segmental bone defects. J Bone Joint Surg Am l1998;80: 985-96.
[23] Horwitz EM, Prockop DJ, Fitzpatrick LA, Koo WW, Gordon PL, Neel M, Sussman M, Orchard P, Marx JC, Pyeritz RE, Brenner MK. Transplantability and therapeutic effects of bone marrow-derived mesenchymal cells in children with osteogenesis imperfecta. Nat Med l1999;5: 309-13.
[24] Horwitz EM, Prockop DJ, Gordon PL, Koo WW, Fitzpatrick LA, Neel MD, McCarville ME, Orchard PJ, Pyeritz RE, Brenner MK. Clinical responses to bone marrow transplantation in children with severe osteogenesis imperfecta. Blood l2001;97: 1227-31.
[25] Oyama M, Tatlock A, Fukuta S, Kavalkovich K, Nishimura K, Johnstone B, Robbins PD, Evans CH, Niyibizi C. Retrovirally transduced bone marrow stromal cells isolated from a mouse model of human osteogenesis imperfecta (oim) persist in bone and retain the ability to form cartilage and bone after extended passaging. Gene Ther l1999;6: 321-9.
[26] Gerstenfeld LC, Wronski TJ, Hollinger JO, Einhorn TA. Application of histomorphometric methods to the study of bone repair. Journal of Bone and Mineral Research l2005;20: 1715-1722.
[27] Cattermole HC, Fordham JN, Muckle DS, Cunningham JL. Dual-energy x-ray absorptiometry as a measure of healing in fractures treated by intramedullary nailing. Journal of Orthopaedic Trauma l1996;10: 563-568.
[28] Ciprian S, Iochum S, Kohlmann R, Dautel G, Dap F, Blum A. MR imaging accuracy in the prediction of bone graft healing potential in scaphoid non-union. Journal De Radiologie l2004;85: 1699-1706.
[29] Grigoryan M, Lynch JA, Fierlinger AL, Guermazi A, Fan B, MacLean DB, MacLean A, Genant HK. Quantitative and qualitative assessment of closed fracture healing using computed tomography and conventional radiography. Academic Radiology l2003;10: 1267-1273.

[30] Hsu WK, Feeley BT, Krenek L, Stout DB, Chatziioannou AF, Lieberman JR. The use of F-18-fluoride and F-18-FDG PET scans to assess fracture healing in a rat femur model. European Journal of Nuclear Medicine and Molecular Imaging l2007;34: 1291-1301.
[31] Lynch JA, Grigoryan M, Fierlinger A, Guermazi A, Zaim S, MacLean DB, Genant HK. Measurement of changes in trabecular bone at fracture sites using X-ray CT and automated image registration and processing. Journal of Orthopaedic Research l2004;22: 362-367.
[32] Saran N, Hamdy RC. DEXA as a Predictor of Fixator Removal in Distraction Osteogenesis. Clinical Orthopaedics and Related Research l2008;466: 2955-2961.
[33] Schmidhammer R, Zandieh S, Mittermayr R, Pelinka LE, Leixnering M, Hopf R, Kroepfl A, Redl H. Assessment of bone union/nonunion in an experimental model using microcomputed technology. Journal of Trauma-Injury Infection and Critical Care l2006;61: 199-205.
[34] Severns AE, Lee YP, Nelson SD, Johnson EE, Kabo JM. Metabolic measurement techniques to assess bone fracture healing - A preliminary study. Clinical Orthopaedics and Related Research l2004: 231-238.
[35] Morgan EF, Mason ZD, Chien KB, Pfeiffer AJ, Barnes GL, Einhorn TA, Gerstenfeld LC. Micro-computed tomography assessment of fracture healing: relationships among callus structure, composition, and mechanical function. Bone l2009;44: 335-44.
[36] Nyman JS, Munoz S, Jadhav S, Mansour A, Yoshii T, Mundy GR, Gutierrez GE. Quantitative measures of femoral fracture repair in rats derived by micro-computed tomography. J Biomech l2009;42: 891-7.
[37] Judex S, Boyd S, Qin YX, Miller L, Muller R, Rubin C. Combining high-resolution micro-computed tomography with material composition to define the quality of bone tissue. Curr Osteoporos Rep l2003;1: 11-9.
[38] Kazakia GJ, Burghardt AJ, Link TM, Majumdar S. Variations in morphological and biomechanical indices at the distal radius in subjects with identical BMD. J Biomech l2011;44: 257-66.
[39] Stone KL, Seeley DG, Lui LY, Cauley JA, Ensrud K, Browner WS, Nevitt MC, Cummings SR. BMD at multiple sites and risk of fracture of multiple types: long-term results from the Study of Osteoporotic Fractures. J Bone Miner Res l2003;18: 1947-54.
[40] Sornay-Rendu E, Munoz F, Garnero P, Duboeuf F, Delmas PD. Identification of osteopenic women at high risk of fracture: The OFELY study. Journal of Bone and Mineral Research l2005;20: 1813-1819.
[41] Schuit SCE, van der Klift M, Weel AEAM, de Laet CEDH, Burger H, Seeman E, Hofman A, Uitterlinden AG, van Leeuwen JPTM, Pols HAP. Fracture incidence and association with bone mineral density in elderly men and women: the Rotterdam Study. Bone l2004;34: 195-202.
[42] Siris ES, Miller PD, Barrett-Connor E, Faulkner KG, Wehren LE, Abbott TA, Berger ML, Santora AC, Sherwood LM. Identification and fracture outcomes of undiagnosed low bone mineral density in postmenopausal women - Results from the National Osteoporosis Risk Assessment. Jama-Journal of the American Medical Association l2001;286: 2815-2822.

[43] Kanis JA, Johnell O, Oden A, Johansson H, McCloskey E. FRAX (TM) and the assessment of fracture probability in men and women from the UK. Osteoporosis International l2008;19: 385-397.
[44] van Lenthe GH, Voide R, Boyd SK, Muller R. Tissue modulus calculated from beam theory is biased by bone size and geometry: implications for the use of three-point bending tests to determine bone tissue modulus. Bone l2008;43: 717-23.
[45] Bourne BC, van der Meulen MC. Finite element models predict cancellous apparent modulus when tissue modulus is scaled from specimen CT-attenuation. J Biomech l2004;37: 613-21.
[46] Shefelbine SJ, Simon U, Claes L, Gold A, Gabet Y, Bab I, Muller R, Augat P. Prediction of fracture callus mechanical properties using micro-CT images and voxel-based finite element analysis. Bone l2005;36: 480-8.
[47] Barnes SL, Lyshchik A, Washington MK, Gore JC, Miga MI. Development of a mechanical testing assay for fibrotic murine liver. Medical Physics l2007;34: 4439-4450.
[48] Greenleaf JF, Fatemi M, Insana M. Selected methods for imaging elastic properties of biological tissues. Annual Review of Biomedical Engineering l2003;5: 57-78.
[49] Miga MI, Rothney MP, Ou JJ. Modality independent elastography (MIE): Potential applications in dermoscopy. Medical Physics l2005;32: 1308-1320.
[50] Ophir J, Cespedes I, Ponnekanti H, Yazdi Y, Li X. Elastography - a Quantitative Method for Imaging the Elasticity of Biological Tissues. Ultrasonic Imaging l1991;13: 111-134.
[51] Ou JJ, Ong RE, Yankeelov TE, Miga MI. Evaluation of 3D modality-independent elastography for breast imaging: a simulation study. Physics in Medicine and Biology l2008;53: 147-163.
[52] Samani A, Plewes D. An inverse problem solution for measuring the elastic modulus of intact ex vivo breast tissue tumours. Physics in Medicine and Biology l2007;52: 1247-1260.
[53] Washington CW, Miga MI. Modality independent elastography (MIE): A new approach to elasticity imaging. Ieee Transactions on Medical Imaging l2004;23: 1117-1128.
[54] Barnes SL, Young PP, Miga MI. A novel model-gel-tissue assay analysis for comparing tumor elastic properties to collagen content. Biomech Model Mechanobiol l2009;8: 337-43.
[55] Samani A, Zubovits J, Plewes D. Elastic moduli of normal and pathological human breast tissues: an inversion-technique-based investigation of 169 samples. Phys Med Biol l2007;52: 1565-76.
[56] Egorov V, Ayrapetyan S, Sarvazyan AP. Prostate mechanical imaging: 3-D image composition and feature calculations. IEEE Trans Med Imaging l2006;25: 1329-40.
[57] Egorov V, Kearney T, Pollak SB, Rohatgi C, Sarvazyan N, Airapetian S, Browning S, Sarvazyan A. Differentiation of benign and malignant breast lesions by mechanical imaging. Breast Cancer Res Treat l2009;118: 67-80.
[58] Egorov V, Sarvazyan AP. Mechanical imaging of the breast. IEEE Trans Med Imaging l2008;27: 1275-87.
[59] Sarvazyan A. Mechanical imaging: a new technology for medical diagnostics. Int J Med Inform l1998;49: 195-216.

[60] Sarvazyan AP, Egorov V. Mechanical imaging in medical applications. Conf Proc IEEE Eng Med Biol Soc l2009;2009: 1975-8.
[61] Weis JA, Miga MI, Granero-Molto F, Spagnoli A. A finite element inverse analysis to assess functional improvement during the fracture healing process. J Biomech l2010;43: 557-62.
[62] Sullivan JM, Charron G, Paulsen KD. A three-dimensional mesh generator for arbitrary multiple material domains. Finite Elements in Analysis and Design l1997;25: 219-241.
[63] Schriefer JL, Robling AG, Warden SJ, Fournier AJ, Mason JJ, Turner CH. A comparison of mechanical properties derived from multiple skeletal sites in mice. Journal of Biomechanics l2005;38: 467-475.
[64] Joachimowicz N, Pichot C, Hugonin JP. Inverse Scattering - an Iterative Numerical-Method for Electromagnetic Imaging. Ieee Transactions on Antennas and Propagation l1991;39: 1742-1752.
[65] Spagnoli A, Longobardi L, O'Rear L. Cartilage disorders: potential therapeutic use of mesenchymal stem cells. Endocr Dev l2005;9: 17-30.
[66] Reynolds DG, Hock C, Shaikh S, Jacobson J, Zhang X, Rubery PT, Beck CA, O'Keefe R J, Lerner AL, Schwarz EM, Awad HA. Micro-computed tomography prediction of biomechanical strength in murine structural bone grafts. J Biomech l2007;40: 3178-86.
[67] Colnot C, Thompson Z, Miclau T, Werb Z, Helms JA. Altered fracture repair in the absence of MMP9. Development l2003;130: 4123-4133.
[68] Jamsa T, Jalovaara P, Peng Z, Vaananen HK, Tuukkanen J. Comparison of three-point bending test and peripheral quantitative computed tomography analysis in the evaluation of the strength of mouse femur and tibia. Bone l1998;23: 155-161.
[69] Choi K, Kuhn JL, Ciarelli MJ, Goldstein SA. The elastic moduli of human subchondral, trabecular, and cortical bone tissue and the size-dependency of cortical bone modulus. J Biomech l1990;23: 1103-13.
[70] Hiltunen A, Vuorio E, Aro HT. A Standardized Experimental Fracture in the Mouse Tibia. Journal of Orthopaedic Research l1993;11: 305-312.
[71] Jingushi S, Joyce ME, Bolander ME. Genetic expression of extracellular matrix proteins correlates with histologic changes during fracture repair. J Bone Miner Res l1992;7: 1045-55.
[72] Spagnoli A, O'Rear L, Chandler RL, Granero-Molto F, Mortlock DP, Gorska AE, Weis JA, Longobardi L, Chytil A, Shimer K, Moses HL. TGF-beta signaling is essential for joint morphogenesis. J Cell Biol l2007;177: 1105-17.
[73] Burge R, Dawson-Hughes B, Solomon DH, Wong JB, King A, Tosteson A. Incidence and economic burden of osteoporosis-related fractures in the United States, 2005-2025. J Bone Miner Res l2007;22: 465-75.
[74] Kwong FN, Hoyland JA, Freemont AJ, Evans CH. Altered relative expression of BMPs and BMP inhibitors in cartilaginous areas of human fractures progressing towards nonunion. J Orthop Res l2009;27: 752-7.
[75] Garrison KR, Donell S, Ryder J, Shemilt I, Mugford M, Harvey I, Song F. Clinical effectiveness and cost-effectiveness of bone morphogenetic proteins in the non-healing of fractures and spinal fusion: a systematic review. Health Technol Assess l2007;11: 1-150, iii-iv.

[76] Kawaguchi H, Jingushi S, Izumi T, Fukunaga M, Matsushita T, Nakamura T, Mizuno K, Nakamura K. Local application of recombinant human fibroblast growth factor-2 on bone repair: a dose-escalation prospective trial on patients with osteotomy. J Orthop Res l2007;25: 480-7.
[77] Morshed S, Corrales L, Genant H, Miclau T, 3rd. Outcome assessment in clinical trials of fracture-healing. J Bone Joint Surg Am l2008;90 Suppl 1: 62-7.
[78] Sharif KM, Parker MJ. Austin Moore hemiarthroplasty: technical aspects and their effects on outcome, in patients with fractures of the neck of femur. Injury l2002;33: 419-22.
[79] Toh EM, Sahni V, Acharya A, Denton JS. Management of intracapsular femoral neck fractures in the elderly; is it time to rethink our strategy? Injury l2004;35: 125-9.
[80] Tomak Y, Kocaoglu M, Piskin A, Yildiz C, Gulman B, Tomak L. Treatment of intertrochanteric fractures in geriatric patients with a modified external fixator. Injury l2005;36: 635-43.
[81] Granero-Molto F, Weis JA, Longobardi L, Spagnoli A. Role of mesenchymal stem cells in regenerative medicine: application to bone and cartilage repair. Expert Opin Biol Ther l2008;8: 255-68.
[82] Myers TJ, Granero-Molto F, Longobardi L, Li T, Yan Y, Spagnoli A. Mesenchymal stem cells at the intersection of cell and gene therapy. Expert Opin Biol Ther 10: 1663-79.
[83] Gardner MJ, van der Meulen MCH, Demetrakopoulos D, Wright TM, Myers ER, Bostrom MP. In vivo cyclic axial compression affects bone healing in the mouse tibia. Journal of Orthopaedic Research l2006;24: 1679-1686.
[84] Moukoko D, Pithioux M, Chabrand P. Temporal evolution of mechanical properties of skeletal tissue regeneration in rabbits: an experimental study. Medical & Biological Engineering & Computing l2007;45: 989-995.
[85] Weis JA, Granero-Molto F, O'Rear LD, Miga MI, Spagnoli A. Development of a high-resolution 3D Micro-CT based model to predict fracture callus histological architecture. Journal of Bone and Mineral Research l2007;22: S482-S483.
[86] Weis JA, Miga MI, Granero-Molto F, Spagnoli A. A finite element inverse analysis to assess functional improvement during the fracture healing process. Journal of Biomechanics l2009 (in press).
[87] Bonnarens F, Einhorn TA. PRODUCTION OF A STANDARD CLOSED FRACTURE IN LABORATORY ANIMAL BONE. Journal of Orthopaedic Research l1984;2: 97-101.
[88] Benzley SE, Perry E, Merkley K, Clark B, Sjaardema G. A Comparison of All-Hexahedral and All-Tetrahedral Finite Element Meshes for Elastic and Elasto-Plastic Analysis. In: Proc. 4th International Meshing Roundtable. Sandia National Laboratories; 1995. p. 179-191.
[89] Granero-Molto F, Weis JA, Landis B, Longobardi L, Miga MI, Spagnoli A. Mesenchymal Stem Cells Enhance Fracture Healing: Essential Role for Cytokines in Homing and Anti-Inflammatory Response. Journal of Bone and Mineral Research l2008;23: S166-S167.
[90] Granero-Molto F, Weis JA, O'Rear LD, Miga MI, Spagnoli A. IGF-I engineered bone marrow mesenchymal stem cells improve the fracture healing process. Journal of Bone and Mineral Research l2007;22: S105-S105.

[91] Gutierrez GE, Edwards JR, Jarrett IR, Nyman JS, Mccluskey B, Rossini G, Flores A, Neidre DB, Mundy GR. Transdermal Lovastatin Enhances Fracture Repair in Rats. Journal of Bone and Mineral Research l2008;23: 1722-1730.
[92] Holzer G, Majeska RJ, Lundy MW, Hartke JR, Einhorn TA. Parathyroid hormone enhances fracture healing - A preliminary report. Clinical Orthopaedics and Related Research l1999: 258-263.
[93] Huddleston PM, Steckelberg JM, Hanssen AD, Rouse MS, Bolander ME, Patel R. Ciprofloxacin inhibition of experimental fracture-healing. Journal of Bone and Joint Surgery-American Volume l2000;82A: 161-173.
[94] Zachos T, Diggs A, Weisbrode S, Bartlett J, Bertone A. Mesenchymal stem cell-mediated gene delivery of bone morphogenetic protein-2 in an articular fracture model. Molecular Therapy l2007;15: 1543-1550.
[95] Zhao M, Zhao Z, Koh JT, Jin TC, Franceschi RT. Combinatorial gene therapy for bone regeneration: Cooperative interactions between adenovirus vectors expressing bone morphogenetic proteins 2, 4, and 7. Journal of Cellular Biochemistry l2005;95: 1-16.
[96] Altschul SF, Gish W, Miller W, Myers EW, Lipman DJ. Basic Local Alignment Search Tool. Journal of Molecular Biology l1990;215: 403-410.
[97] Altschul SF, Madden TL, Schaffer AA, Zhang JH, Zhang Z, Miller W, Lipman DJ. Gapped BLAST and PSI-BLAST: a new generation of protein database search programs. Nucleic Acids Research l1997;25: 3389-3402.
[98] Mooney M. A theory of large elastic deformation. Journal of Applied Physics l1940;11: 582-592.
[99] Rivlin RS. Large elastic deformations of isotropic materials. I. Fundamental concepts. Philosophical Transactions of the Royal Society of London. Series A, Mathematical and Physical Sciences l1948;240: 459-490.
[100] Tsuji K, Harfe BD, Cox K, Bouxsein M, Gerstenfeld L, Bandyopadhyay A, Tabin C, Rosen V. Absence of BMP2 results in low bone mineral density, osteoarthritis, spontaneous fracture and impaired fracture healing. Journal of Bone and Mineral Research l2005;20: S8-S8.
[101] Rosen V. BMP2 signaling in bone development and repair. Cytokine Growth Factor Rev l2009;20: 475-80.
[102] Yu YY, Lieu S, Lu C, Colnot C. Bone morphogenetic protein 2 stimulates endochondral ossification by regulating periosteal cell fate during bone repair. Bone l2010;47: 65-73.
[103] Zhang H, Bradley A. Mice deficient for BMP2 are nonviable and have defects in amnion/chorion and cardiac development. Development l1996;122: 2977-86.
[104] Keating JF, Blachut PA, O'Brien PJ, Court-Brown CM. Reamed nailing of Gustilo grade-IIIB tibial fractures. J Bone Joint Surg Br l2000;82: 1113-6.
[105] Praemer A, Furner S, Rice DP, American Academy of Orthopaedic Surgeons. Musculoskeletal conditions in the United States. [2nd ed. Rosemont, Ill.: American Academy of Orthopaedic Surgeons; 1999.
[106] Pittenger MF, Mackay AM, Beck SC, Jaiswal RK, Douglas R, Mosca JD, Moorman MA, Simonetti DW, Craig S, Marshak DR. Multilineage potential of adult human mesenchymal stem cells. Science l1999;284: 143-7.
[107] Marcacci M, Kon E, Moukhachev V, Lavroukov A, Kutepov S, Quarto R, Mastrogiacomo M, Cancedda R. Stem cells associated with macroporous bioceramics for

long bone repair: 6- to 7-year outcome of a pilot clinical study. Tissue Eng l2007;13: 947-55.
[108] Quarto R, Mastrogiacomo M, Cancedda R, Kutepov SM, Mukhachev V, Lavroukov A, Kon E, Marcacci M. Repair of large bone defects with the use of autologous bone marrow stromal cells. N Engl J Med l2001;344: 385-6.
[109] Hernigou P, Mathieu G, Poignard A, Manicom O, Beaujean F, Rouard H. Percutaneous autologous bone-marrow grafting for nonunions. Surgical technique. J Bone Joint Surg Am l2006;88 Suppl 1 Pt 2: 322-7.
[110] Hernigou P, Poignard A, Beaujean F, Rouard H. Percutaneous autologous bone-marrow grafting for nonunions. Influence of the number and concentration of progenitor cells. J Bone Joint Surg Am l2005;87: 1430-7.
[111] Hernigou P, Poignard A, Manicom O, Mathieu G, Rouard H. The use of percutaneous autologous bone marrow transplantation in nonunion and avascular necrosis of bone. J Bone Joint Surg Br l2005;87: 896-902.
[112] Tseng SS, Lee MA, Reddi AH. Nonunions and the potential of stem cells in fracture-healing. J Bone Joint Surg Am l2008;90 Suppl 1: 92-8.
[113] Chapel A, Bertho JM, Bensidhoum M, Fouillard L, Young RG, Frick J, Demarquay C, Cuvelier F, Mathieu E, Trompier F, Dudoignon N, Germain C, Mazurier C, Aigueperse J, Borneman J, Gorin NC, Gourmelon P, Thierry D. Mesenchymal stem cells home to injured tissues when co-infused with hematopoietic cells to treat a radiation-induced multi-organ failure syndrome. J Gene Med l2003;5: 1028-38.
[114] Gao J, Dennis JE, Muzic RF, Lundberg M, Caplan AI. The dynamic in vivo distribution of bone marrow-derived mesenchymal stem cells after infusion. Cells Tissues Organs l2001;169: 12-20.
[115] Barbash IM, Chouraqui P, Baron J, Feinberg MS, Etzion S, Tessone A, Miller L, Guetta E, Zipori D, Kedes LH, Kloner RA, Leor J. Systemic delivery of bone marrow-derived mesenchymal stem cells to the infarcted myocardium: feasibility, cell migration, and body distribution. Circulation l2003;108: 863-8.
[116] Zou YR, Kottmann AH, Kuroda M, Taniuchi I, Littman DR. Function of the chemokine receptor CXCR4 in haematopoiesis and in cerebellar development. Nature l1998;393: 595-9.
[117] Wynn RF, Hart CA, Corradi-Perini C, O'Neill L, Evans CA, Wraith JE, Fairbairn LJ, Bellantuono I. A small proportion of mesenchymal stem cells strongly expresses functionally active CXCR4 receptor capable of promoting migration to bone marrow. Blood l2004;104: 2643-5.
[118] Von Luttichau I, Notohamiprodjo M, Wechselberger A, Peters C, Henger A, Seliger C, Djafarzadeh R, Huss R, Nelson PJ. Human adult CD34- progenitor cells functionally express the chemokine receptors CCR1, CCR4, CCR7, CXCR5, and CCR10 but not CXCR4. Stem Cells Dev l2005;14: 329-36.
[119] Le Blanc K, Gotherstrom C, Ringden O, Hassan M, McMahon R, Horwitz E, Anneren G, Axelsson O, Nunn J, Ewald U, Norden-Lindeberg S, Jansson M, Dalton A, Astrom E, Westgren M. Fetal mesenchymal stem-cell engraftment in bone after in utero transplantation in a patient with severe osteogenesis imperfecta. Transplantation l2005;79: 1607-14.
[120] da Silva Meirelles L, Caplan AI, Nardi NB. In search of the in vivo identity of mesenchymal stem cells. Stem Cells l2008;26: 2287-99.

[121] Ortiz LA, Gambelli F, McBride C, Gaupp D, Baddoo M, Kaminski N, Phinney DG. Mesenchymal stem cell engraftment in lung is enhanced in response to bleomycin exposure and ameliorates its fibrotic effects. Proc Natl Acad Sci U S A l2003;100: 8407-11.
[122] Zappia E, Casazza S, Pedemonte E, Benvenuto F, Bonanni I, Gerdoni E, Giunti D, Ceravolo A, Cazzanti F, Frassoni F, Mancardi G, Uccelli A. Mesenchymal stem cells ameliorate experimental autoimmune encephalomyelitis inducing T-cell anergy. Blood l2005;106: 1755-61.
[123] Parekkadan B, van Poll D, Suganuma K, Carter EA, Berthiaume F, Tilles AW, Yarmush ML. Mesenchymal stem cell-derived molecules reverse fulminant hepatic failure. PLoS One l2007;2: e941.
[124] Bartholomew A, Sturgeon C, Siatskas M, Ferrer K, McIntosh K, Patil S, Hardy W, Devine S, Ucker D, Deans R, Moseley A, Hoffman R. Mesenchymal stem cells suppress lymphocyte proliferation in vitro and prolong skin graft survival in vivo. Exp Hematol l2002;30: 42-8.
[125] Le Blanc K, Frassoni F, Ball L, Locatelli F, Roelofs H, Lewis I, Lanino E, Sundberg B, Bernardo ME, Remberger M, Dini G, Egeler RM, Bacigalupo A, Fibbe W, Ringden O. Mesenchymal stem cells for treatment of steroid-resistant, severe, acute graft-versus-host disease: a phase II study. Lancet l2008;371: 1579-86.
[126] Petite H, Viateau V, Bensaid W, Meunier A, de Pollak C, Bourguignon M, Oudina K, Sedel L, Guillemin G. Tissue-engineered bone regeneration. Nat Biotechnol l2000;18: 959-63.
[127] Chandler RL, Chandler KJ, McFarland KA, Mortlock DP. Bmp2 transcription in osteoblast progenitors is regulated by a distant 3' enhancer located 156.3 kilobases from the promoter. Mol Cell Biol l2007;27: 2934-51.
[128] Fowler M, Virostko J, Chen Z, Poffenberger G, Radhika A, Brissova M, Shiota M, Nicholson WE, Shi Y, Hirshberg B, Harlan DM, Jansen ED, Powers AC. Assessment of pancreatic islet mass after islet transplantation using in vivo bioluminescence imaging. Transplantation l2005;79: 768-76.
[129] Deal KK, Cantrell VA, Chandler RL, Saunders TL, Mortlock DP, Southard-Smith EM. Distant regulatory elements in a Sox10-beta GEO BAC transgene are required for expression of Sox10 in the enteric nervous system and other neural crest-derived tissues. Dev Dyn l2006;235: 1413-32.
[130] Nolan GP, Fiering S, Nicolas JF, Herzenberg LA. Fluorescence-activated cell analysis and sorting of viable mammalian cells based on beta-D-galactosidase activity after transduction of Escherichia coli lacZ. Proc Natl Acad Sci U S A l1988;85: 2603-7.
[131] Devine MJ, Mierisch CM, Jang E, Anderson PC, Balian G. Transplanted bone marrow cells localize to fracture callus in a mouse model. J Orthop Res l2002;20: 1232-9.
[132] Peled A, Petit I, Kollet O, Magid M, Ponomaryov T, Byk T, Nagler A, Ben-Hur H, Many A, Shultz L, Lider O, Alon R, Zipori D, Lapidot T. Dependence of human stem cell engraftment and repopulation of NOD/SCID mice on CXCR4. Science l1999;283: 845-8.
[133] Honczarenko M, Le Y, Swierkowski M, Ghiran I, Glodek AM, Silberstein LE. Human bone marrow stromal cells express a distinct set of biologically functional chemokine receptors. Stem Cells l2006;24: 1030-41.

[134] Chamberlain G, Wright K, Rot A, Ashton B, Middleton J. Murine mesenchymal stem cells exhibit a restricted repertoire of functional chemokine receptors: comparison with human. PLoS One l2008;3: e2934.
[135] Fox JM, Chamberlain G, Ashton BA, Middleton J. Recent advances into the understanding of mesenchymal stem cell trafficking. Br J Haematol l2007;137: 491-502.
[136] Kumagai K, Vasanji A, Drazba JA, Butler RS, Muschler GF. Circulating cells with osteogenic potential are physiologically mobilized into the fracture healing site in the parabiotic mice model. J Orthop Res l2008;26: 165-75.
[137] Rombouts WJ, Ploemacher RE. Primary murine MSC show highly efficient homing to the bone marrow but lose homing ability following culture. Leukemia l2003;17: 160-70.
[138] Cheng Z, Ou L, Zhou X, Li F, Jia X, Zhang Y, Liu X, Li Y, Ward CA, Melo LG, Kong D. Targeted migration of mesenchymal stem cells modified with CXCR4 gene to infarcted myocardium improves cardiac performance. Mol Ther l2008;16: 571-9.
[139] Bruder SP, Fink DJ, Caplan AI. Mesenchymal stem cells in bone development, bone repair, and skeletal regeneration therapy. J Cell Biochem l1994;56: 283-94.
[140] Szulc P, Delmas PD. Bone loss in elderly men: increased endosteal bone loss and stable periosteal apposition. The prospective MINOS study. Osteoporos Int l2007;18: 495-503.
[141] Markel MD, Wikenheiser MA, Chao EY. A study of fracture callus material properties: relationship to the torsional strength of bone. J Orthop Res l1990;8: 843-50.
[142] Rutten S, Nolte PA, Korstjens CM, van Duin MA, Klein-Nulend J. Low-intensity pulsed ultrasound increases bone volume, osteoid thickness and mineral apposition rate in the area of fracture healing in patients with a delayed union of the osteotomized fibula. Bone l2008;43: 348-54.
[143] Mitsiadis TA, Barrandon O, Rochat A, Barrandon Y, De Bari C. Stem cell niches in mammals. Exp Cell Res l2007;313: 3377-85.
[144] Wilson A, Trumpp A. Bone-marrow haematopoietic-stem-cell niches. Nat Rev Immunol l2006;6: 93-106.
[145] Glennie S, Soeiro I, Dyson PJ, Lam EW, Dazzi F. Bone marrow mesenchymal stem cells induce division arrest anergy of activated T cells. Blood l2005;105: 2821-7.
[146] Jung Y, Song J, Shiozawa Y, Wang J, Wang Z, Williams B, Havens A, Schneider A, Ge C, Franceschi RT, McCauley LK, Krebsbach PH, Taichman RS. Hematopoietic stem cells regulate mesenchymal stromal cell induction into osteoblasts thereby participating in the formation of the stem cell niche. Stem Cells l2008;26: 2042-51.